Wallace, L.M., Saffer, D.M., Barnes, P.M., Pecher, I.A., Petronotis, K.E., LeVay, L.J., and the Expedition 372/375 Scientists
Proceedings of the International Ocean Discovery Program Volume 372B/375
publications.iodp.org

https://doi.org/10.14379/iodp.proc.372B375.104.2019

Check for updates

Site U1519[1]

P.M. Barnes, L.M. Wallace, D.M. Saffer, I.A. Pecher, K.E. Petronotis, L.J. LeVay, R.E. Bell, M.P. Crundwell, C.H. Engelmann de Oliveira, A. Fagereng, P.M. Fulton, A. Greve, R.N. Harris, Y. Hashimoto, A. Hüpers, M.J. Ikari, Y. Ito, H. Kitajima, S. Kutterolf, H. Lee, X. Li, M. Luo, P.R. Malie, F. Meneghini, J.K. Morgan, A. Noda, H.S. Rabinowitz, H.M. Savage, C.L. Shepherd, S. Shreedharan, E.A. Solomon, M.B. Underwood, M. Wang, A.D. Woodhouse, S.M. Bourlange, M.M.Y. Brunet, S. Cardona, M.B. Clennell, A.E. Cook, B. Dugan, J. Elger, D. Gamboa, A. Georgiopoulou, S. Han, K.U. Heeschen, G. Hu, G.Y. Kim, H. Koge, K.S. Machado, D.D. McNamara, G.F. Moore, J.J. Mountjoy, M.A. Nole, S. Owari, M. Paganoni, P.S. Rose, E.J. Screaton, U. Shankar, M.E. Torres, X. Wang, and H.-Y. Wu[2]

Keywords: International Ocean Discovery Program, IODP, *JOIDES Resolution*, Expedition 372, Expedition 375, Site U1519, Hikurangi margin, slow slip events, observatory, subduction

Contents

Background and objectives

Site U1519 (proposed Site HSM-01A) is located on the upper continental slope of the Hikurangi margin ~38 km from shore in 1000 m water depth at the landward edge of a 12 km wide midslope sedimentary basin (Figure **F1**; see Figure **F3** in the Expedition 372B/375 summary chapter [Saffer et al., 2019a]). The basin is officially unnamed but is referred to as the Tuaheni Basin. The slope west of the Tuaheni Basin rises to the edge of the continental shelf and hosts the North Tuaheni Landslide. This landslide and other landslides have delivered late Quaternary mass transport deposits (MTDs) and associated sediments directly into the basin (Mountjoy et al., 2014). The seafloor in the basin is underlain by these deposits and is approximately horizontal with localized relief of <20 m in the area of Site U1519 (Figures **F1**, **F2**).

Active thrust faults reach the seafloor on the continental shelf west (landward) of Site U1519 (Mountjoy and Barnes, 2011) and on the mid–lower slope trenchward of the site (Barker et al., 2009, 2018; Bell et al., 2010; Pedley et al., 2010). No active thrust faults are recognized directly beneath the basin; however, an apparently inactive and buried northwest-dipping thrust fault lies ~1.1 km below Site U1519. This fault is associated with an eroded hanging wall sequence that dips northwest (Figure **F2**). The plate interface that hosts large (>10 cm) slip during slow slip events (SSEs) lies ~5 km below the seafloor at Site U1519 (Wallace et al., 2016) (see Figure **F2** in the Expedition 372B/375 summary chapter [Saffer et al., 2019a]).

Based on predrilling interpretation of the seismic data (Figure **F2**), three main unconformity-bounded lithostratigraphic units were identified at Site U1519 to the drilling target depth at 650 meters below seafloor (mbsf). These units include ~260–270 m of horizontally layered basin fill comprising MTDs and sequences of turbidites, a southeast-dipping slope sequence of MTDs and layered strata about 260–270 m thick (to 530 mbsf), and a basal 120 m thick unit of northwest-dipping strata on the back limb of the inactive thrust fault. Although no age control was available prior to drilling, the upper unit was interpreted to be late Quaternary in age and the middle unit was thought to be Plio–Pleistocene. Prior to drilling, the basal unit was interpreted to be Miocene–Pliocene, possibly correlating with the Tolaga Group onshore (e.g., Field et al., 1997). A possible weak bottom-simulating reflector (BSR) projects through Site U1519 at or below 560 mbsf.

The primary objectives at Site U1519 were to install an observatory to monitor deformation, temperature, and hydrological changes throughout the slow slip cycle and to use coring and log-

[1] Barnes, P.M., Wallace, L.M., Saffer, D.M., Pecher, I.A., Petronotis, K.E., LeVay, L.J., Bell, R.E., Crundwell, M.P., Engelmann de Oliveira, C.H., Fagereng, A., Fulton, P.M., Greve, A., Harris, R.N., Hashimoto, Y., Hüpers, A., Ikari, M.J., Ito, Y., Kitajima, H., Kutterolf, S., Lee, H., Li, X., Luo, M., Malie, P.R., Meneghini, F., Morgan, J.K., Noda, A., Rabinowitz, H.S., Savage, H.M., Shepherd, C.L., Shreedharan, S., Solomon, E.A., Underwood, M.B., Wang, M., Woodhouse, A.D., Bourlange, S.M., Brunet, M.M.Y., Cardona, S., Clennell, M.B., Cook, A.E., Dugan, B., Elger, J., Gamboa, D., Georgiopoulou, A., Han, S., Heeschen, K.U., Hu, G., Kim, G.Y., Koge, H., Machado, K.S., McNamara, D.D., Moore, G.F., Mountjoy, J.J., Nole, M.A., Owari, S., Paganoni, M., Rose, P.S., Screaton, E.J., Shankar, U., Torres, M.E., Wang, X., and Wu, H.-Y., 2019. Site U1519. *In* Wallace, L.M., Saffer, D.M., Barnes, P.M., Pecher, I.A., Petronotis, K.E., LeVay, L.J., and the Expedition 372/375 Scientists, *Hikurangi Subduction Margin Coring, Logging, and Observatories*. Proceedings of the International Ocean Discovery Program, 372B/375: College Station, TX (International Ocean Discovery Program). https://doi.org/10.14379/iodp.proc.372B375.104.2019

[2] **Expedition 372B/375 Scientists' affiliations.**

MS 372B375-104: Published 5 May 2019

Figure F1. A. Bathymetry and location of Site U1519. B. Detailed location map, Holes U1519A–U1519E. White dot = LWD Hole U1519A drilled during Expedition 372, orange dots = Holes U1519C–U1519E cored during Expedition 375, yellow dot = observatory Hole U1519B. Background bathymetry grid gray shading is at 25 m cell resolution. Red/black line in A and yellow line in B show location of Seismic Profile 05CM-04 in Figure F2.

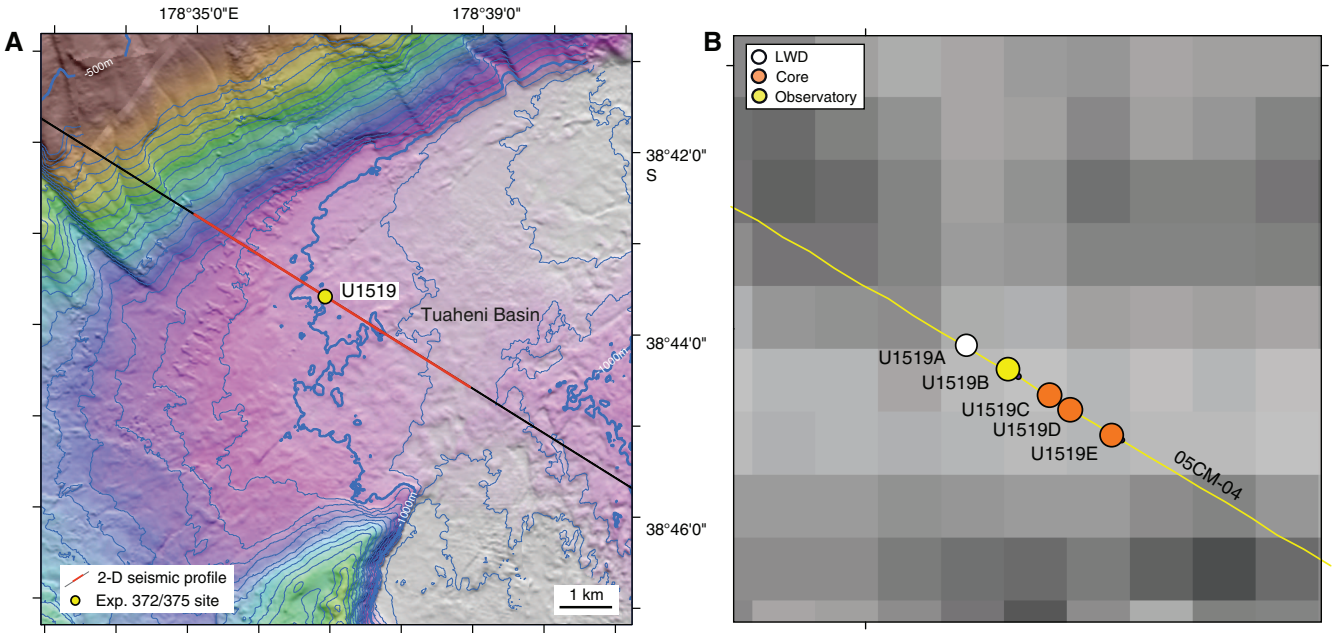

Figure F2. Prestack time migrated seismic reflection image from Profile 05CM-04 (Barker et al., 2018) through Site U1519 (pre-expedition interpretation). Location of seismic line shown in Figure F1. Red lines = interpreted faults. VE = vertical exaggeration.

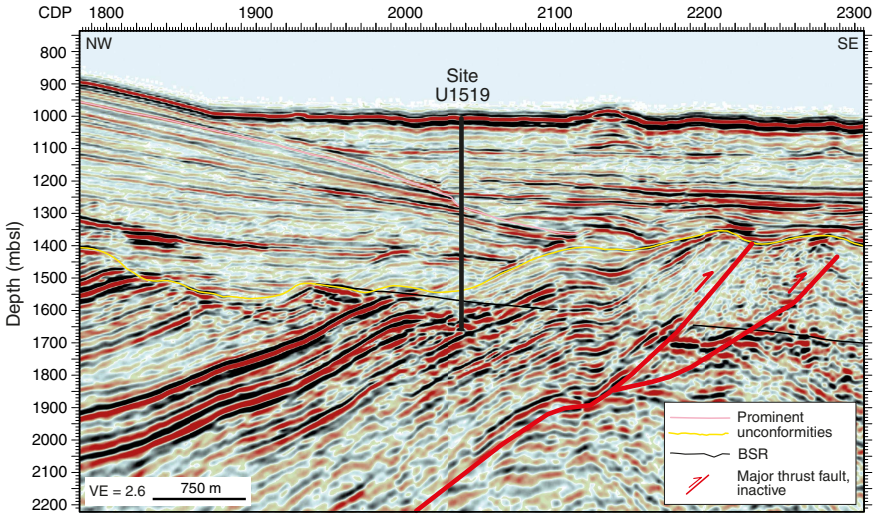

ging-while-drilling (LWD) data to better understand the composition, physical properties, thermal state, and in situ stress state in the hanging wall above the SSE source region. The objective of the borehole observatory is to record pressure and temperature over multiple SSE cycles at a site on the inner margin above portions of the plate interface that host large SSE displacements modeled from geodetic data (e.g., Wallace and Beavan, 2010; Wallace et al., 2016).

The main objective of logging and coring at Site U1519 was to provide information about rock physical properties, composition, thermal state, and structural geology and deformation in the upper plate overlying the SSE source region. LWD logs and core from Site U1519 will also provide constraints on the evolution of the upper slope and basin environment and the timing of apparent thrust cessation across this section of the inner continental slope. Pore fluid geochemistry data will provide insights into diagenetic processes and potential sources and flow pathways of fluid sampled in the upper plate.

One key focus for post-expedition studies on core samples will be geomechanical measurements to define poroelastic and strength properties. These data will be essential for interpretation of observatory data, such as calibrating the use of pore pressure as a proxy for volumetric strain (e.g., Wang, 2004; Davis et al., 2009). Similarly, strength, permeability, and elastic moduli measurements will provide the necessary data to estimate in situ stress magnitude from any observed wellbore breakouts (e.g., Zoback, 2007; Chang et al., 2010; Huffman and Saffer, 2016) and to parameterize hydrological

and geomechanical models. Core-log-seismic integration will allow extrapolation of seismic attributes and in situ conditions (stress, fault zone properties, and pore pressure) away from the borehole over a broad region of existing 2-D and newly acquired 3-D seismic data.

Drilling during International Ocean Discovery Program (IODP) Expedition 372 included LWD to 650 mbsf in Hole U1519A. Drilling during IODP Expedition 375 included coring with the rotary core barrel (RCB) system in Hole U1519C in three discrete intervals (108–163.6, 250–288.4, and 520–640 mbsf) and the advanced piston corer (APC) system from 0 to 23.3 mbsf in Hole U1519D and from 0 to 85.8 mbsf in Hole U1519E. The observatory installed in Hole U1519B includes two formation pore pressure monitoring intervals at 125 and 263.6 mbsf and a string of 15 temperature sensors spanning from 47.8 to 262 mbsf.

Operations

Expedition 372

The R/V *JOIDES Resolution* arrived at Site U1519 at 0530 h (UTC + 13 h) on 24 December 2017 after a 15.4 nmi transit from Site U1518. Site U1519 consisted of one LWD hole during Expedition 372 (Table **T1**).

Hole U1519A

The LWD bottom-hole assembly (BHA) was assembled and included the geoVISION, NeoScope, StethoScope, TeleScope, SonicScope, and proVISION tools behind an 8½ inch drill bit. The LWD BHA and drill string were deployed to 952 meters below sea level (mbsl), and the tools were pump tested before spudding the hole; all turbine-dependent tools were activated during the pump test. Hole U1519A (38°43.6372′S, 178°36.8537′E; 1000.7 mbsl; Table **T1**) was spudded at 1200 h on 24 December 2017 and continued to 26 December. The seafloor depth for Hole U1519A was set at 1000.7 mbsl based on the LWD logs. After logging to 650 mbsf, a 30 bbl mud sweep was used to clean the hole, and the LWD tools and drill string were pulled out of the hole. The bit cleared the seafloor at 0425 h and the rig floor at 0855 h. The vessel began the transit to Site U1520 at 0910 h on 26 December. The time spent at Site U1519 during Expedition 372 was 2.17 days.

Safety monitoring

Continuous safety monitoring (see **Logging while drilling** in the Expedition 372B/375 methods chapter [Wallace et al., 2019]) was completed during LWD operations at Site U1519 to monitor for the presence of abnormal pressure or free gas and to ensure safe drilling conditions. Real-time monitoring in Hole U1519A started

Table T1. Core summary, Site U1519. * = total advanced, † = total cored. DRF = drilling depth below rig floor, DSF = drilling depth below seafloor, CSF = core depth below seafloor. LWD = logging while drilling. NA = not applicable. H = advanced piston corer (APC), F = half-length APC, R = rotary core barrel, numeric core type = drilled interval. NM = nonmagnetic core barrel. APCT-3 = advanced piston corer temperature tool. (Continued on next page.) **Download table in CSV format.**

Hole U1519A (Expedition 372)
Latitude: 38°43.6372′S
Longitude: 178°36.8537′E
Time on hole: 52.08 h (2.17 d)
Seafloor (drill pipe measurement from rig floor, m DRF): 1011.6
Distance between rig floor and sea level (m): 10.9
Water depth (drill pipe measurement from sea level, m): 1000.7
Total penetration (drilling depth below seafloor, m DSF): 650.0 (LWD)
Total length of cored section (m): NA
Total core recovered (m): NA
Core recovery (%): NA
Total number of cores: NA

Hole U1519B (Expedition 375)
Latitude: 38°43.6426′S
Longitude: 178°36.8655′E
Time on hole: 112.56 h (4.69 d)
Seafloor (drill pipe measurement from rig floor, m DRF): 1011.5
Distance between rig floor and sea level (m): 11.1
Water depth (drill pipe measurement from sea level, m): 1000.4
Total penetration (drilling depth below seafloor, m DSF): 283.2 (CORK)
Total length of cored section (m): NA
Total core recovered (m): NA
Core recovery (%): NA
Total number of cores: NA

Hole U1519C (Expedition 375)
Latitude: 38°43.6483′S
Longitude: 178°36.8773′E
Time on hole: 69.36 h (2.89 d)
Seafloor (drill pipe measurement from rig floor, m DRF): 1011.5
Distance between rig floor and sea level (m): 11.2
Water depth (drill pipe measurement from sea level, m): 1000.3
Total penetration (drilling depth below seafloor, m DSF): 640.0
Total length of cored section (m): 215.6
Total core recovered (m): 119.17
Core recovery (%): 55
Total number of cores: 23

Hole U1519D (Expedition 375)
Latitude: 38°43.6516′S
Longitude: 178°36.8831′E
Time on hole: 9.84 h (0.41 d)
Seafloor (drill pipe measurement from rig floor, m DRF): 1011.6
Distance between rig floor and sea level (m): 11.2
Water depth (drill pipe measurement from sea level, m): 1000.4
Total penetration (drilling depth below seafloor, m DSF): 23.3
Total length of cored section (m): 23.3
Total core recovered (m): 23.64
Core recovery (%): 101
Total number of cores: 3

Hole U1519E (Expedition 375)
Latitude: 38°43.6572′S
Longitude: 178°36.8949′E
Time on hole: 19.2 h (0.80 d)
Seafloor (drill pipe measurement from rig floor, m DRF): 1011.5
Distance between rig floor and sea level (m): 11.2
Water depth (drill pipe measurement from sea level, m): 1000.3
Total penetration (drilling depth below seafloor, m DSF): 85.8
Total length of cored section (m): 85.8
Total core recovered (m): 88.98
Core recovery (%): 106
Total number of cores: 13

Table T1 (continued).

Core	Date	Time on deck UTC (h)	Top depth drilled DSF (m)	Bottom depth drilled DSF (m)	Interval advanced (m)	Top depth cored CSF (m)	Bottom depth cored CSF (m)	Recovered length (m)	Core recovery (%)	Comment
372-U1519A-										
11	25 Dec 2017	NA	0.0	650.0		*****Drilled from 0 to 650.0 m DSF*****				Logging while drilling
375-U1519B-										
11	13 Apr 2018	NA	0.0	283.2		*****Drilled from 0 to 283.2 m DSF*****				ACORK/CORK-II observatory
375-U1519C-										
11	18 Apr 2018	NA	0.0	108.0		*****Drilled from 0 to 108.0 m DSF*****				Drilled interval
2R	18 Apr 2018	1330	108.0	115.6	7.6	108.0	111.74	3.74	49	NM
3R	18 Apr 2018	1430	115.6	125.2	9.6	115.6	116.18	0.58	6	NM
4R	18 Apr 2018	1520	125.2	134.8	9.6	125.2	131.20	6.00	63	NM
5R	18 Apr 2018	1610	134.8	144.3	9.5	134.8	136.03	1.23	13	NM
6R	18 Apr 2018	1640	144.3	154.0	9.7	144.3	144.42	0.12	1	NM
7R	18 Apr 2018	1720	154.0	163.6	9.6	154.0	154.00	0.00	0	NM
81	18 Apr 2018	NA	163.6	250.0		*****Drilled from 163.6 to 250.0 m DSF*****				Drilled interval
9R	18 Apr 2018	2240	250.0	259.6	9.6	250.0	256.86	6.86	71	NM
10R	19 Apr 2018	0000	259.6	269.2	9.6	259.6	267.22	7.62	79	NM
11R	19 Apr 2018	0130	269.2	278.8	9.6	269.2	272.56	3.36	35	NM
12R	19 Apr 2018	0300	278.8	288.4	9.6	278.8	284.80	6.00	63	NM
131	19 Apr 2018	NA	288.4	518.4		*****Drilled from 288.4 to 518.4 m DSF*****				Drilled interval
14R	19 Apr 2018	2115	518.4	528.0	9.6	518.4	522.54	4.14	43	NM
15R	19 Apr 2018	2255	528.0	537.6	9.6	528.0	536.41	8.41	88	NM
16R	20 Apr 2018	0030	537.6	547.1	9.5	537.6	546.97	9.37	99	NM
17R	20 Apr 2018	0200	547.1	556.7	9.6	547.1	553.47	6.37	66	NM
18R	20 Apr 2018	0340	556.7	566.2	9.5	556.7	566.03	9.33	98	NM
19R	20 Apr 2018	0450	566.2	575.7	9.5	566.2	575.03	8.83	93	NM
20R	20 Apr 2018	0620	575.7	585.3	9.6	575.7	580.48	4.78	50	NM
21R	20 Apr 2018	0810	585.3	594.9	9.6	585.3	591.68	6.38	66	NM
22R	20 Apr 2018	0950	594.9	604.5	9.6	594.9	603.08	8.18	85	NM
23R	20 Apr 2018	1110	604.5	614.0	9.5	604.5	610.91	6.41	67	NM
24R	20 Apr 2018	1240	614.0	623.6	9.6	614.0	618.85	4.85	51	NM
25R	20 Apr 2018	1430	623.6	633.2	9.6	623.6	627.76	4.16	43	NM
26R	20 Apr 2018	1545	633.2	640.0	6.8	633.2	635.65	2.45	36	NM
		Hole U1519C totals:		640.0*	215.6†			119.17	55	
375-U1519D-										
1H	21 Apr 2018	0315	0.0	4.3	4.3	0.0	4.36	4.36	101	NM
2H	21 Apr 2018	0420	4.3	13.8	9.5	4.3	14.25	9.95	105	NM
3H	21 Apr 2018	0545	13.8	23.3	9.5	13.8	23.13	9.33	98	NM; partial stroke
		Hole U1519D totals:		23.3*	23.3†			23.64	101	
375-U1519E-										
1H	21 Apr 2018	0655	0.0	4.6	4.6	0.0	4.56	4.56	99	NM
2H	21 Apr 2018	0720	4.6	14.1	9.5	4.6	14.46	9.86	104	NM
3H	21 Apr 2018	0825	14.1	21.9	7.8	14.1	21.99	7.89	101	NM
4H	21 Apr 2018	0940	21.9	31.3	9.4	21.9	31.28	9.38	100	NM; APCT-3
5H	21 Apr 2018	1100	31.3	40.1	8.8	31.3	40.08	8.78	100	NM; APCT-3
6H	21 Apr 2018	1230	40.1	49.6	9.5	40.1	50.26	10.16	107	NM; APCT-3
7H	21 Apr 2018	1415	49.6	57.0	7.4	49.6	56.93	7.33	99	NM; APCT-3
8H	21 Apr 2018	1600	57.0	62.3	5.3	57.0	62.23	5.23	99	NM; APCT-3
9F	21 Apr 2018	1730	62.3	67.0	4.7	62.3	67.55	5.25	112	NM; APCT-3
10F	21 Apr 2018	1810	67.0	71.7	4.7	67.0	72.12	5.12	109	NM
11F	21 Apr 2018	1915	71.7	76.4	4.7	71.7	76.60	4.90	104	NM; APCT-3
12F	21 Apr 2018	1950	76.4	81.1	4.7	76.4	81.58	5.18	110	NM
13F	21 Apr 2018	2045	81.1	85.8	4.7	81.1	86.21	5.11	109	NM; APCT-3
		Hole U1519E totals:		85.8*	85.8†			88.75	103	
		Site U1519 totals:		1684.2*	324.7†			231.56	71	

at 37 mbsf and continued to 650 mbsf. Overpressures generally increased downhole, reaching approximately 0.689 MPa (100 psi) at the bottom of the borehole. Eight pressure kicks were observed in the borehole and required special monitoring. Each of these pressure kicks was an isolated point and likely the result of circulation or annular pressure while drilling (APWD) sensor issues. Additionally, these kicks were manageable with 10.5 lb/gal mud. Mud circulation was not required, however, because of the short duration of these events.

Expedition 375

After waiting on weather in the Bay of Plenty for 36.75 h, we arrived at Site U1519 at 1810 h (UTC + 12 h) on 13 April 2018. Upon arriving on location, the thrusters were lowered, the dynamic posi-

tioning system was engaged, and an acoustic positioning beacon was deployed. During Expedition 375, Site U1519 consisted of an observatory hole and three coring holes (Table **T1**). The time spent at Site U1519 during Expedition 375 was 8.79 days. The total time spent at Site U1519 during both expeditions was 10.96 days.

Hole U1519B observatory

First, we moved the base of the reentry cone needed for the observatory installation to the moonpool. Next, we assembled a BHA with a 14¾ inch drill bit. Hole U1519B (38°43.6426′S, 178°36.8655′E; 1000.4 mbsl; Table **T1**) was spudded at 0105 h on 14 April 2018 and reached a total depth of 283.2 mbsf at 1630 h. A 30 bbl mud sweep was circulated to clean the hole of cuttings, and the bit was raised to 71 mbsf. At 1845 h, the reentry cone and its base were released from the moonpool and allowed to fall to the seafloor. The subsea camera was deployed to check that the reentry cone had landed properly and to observe the reentry cone while pulling the BHA out of the hole. The subsea camera was recovered at 2015 h on 14 April, and the drill string was recovered at 2225 h. Next, the hydraulic release tool (HRT) needed to deploy the first stage of the observatory was assembled and stored in the derrick.

The next step in the observatory installation was to assemble the 279 m long ACORK casing string consisting of 22 joints of 10¾ inch casing, two casing joints with 2 m long screens for pressure monitoring, and an umbilical secured on the outside of the casing to connect the two casing screens to pressure loggers on the wellhead (Figure **F3A**). As the casing string was assembled from the bottom up, the umbilical was connected to the bottom and top screens, which were intended to be deployed at 264 and 124 mbsf, respectively. The casing string was completed at 1245 h on 15 April and landed in the moonpool.

Next, we assembled the drilling stinger needed to guide the casing into the predrilled hole. The drilling assembly was composed of a 9⅞ inch drill bit, an underreamer with its arms set to 14¾ inches to clear any obstacles in the hole, and a mud motor to rotate the bit and underreamer in isolation from the ACORK casing (Figure **F3B**). The underreamer arms were tested, and the drilling assembly was completed and landed inside the casing by 1645 h on 15 April.

The pressure umbilical terminations were made on the ACORK wellhead at 1930 h, and the wellhead was submerged for 10 min with the valves in the open position to purge the lines of air. The wellhead was then brought back to the surface to set the valves to their deployment (closed) position, and the wellhead was submerged for the last time. The entire assembly with the HRT running tool; the ACORK wellhead, casing, and umbilical; and the drilling assembly was lowered to the seafloor between 2000 and 2130 h on 15 April.

The subsea camera was then deployed to assist with reentry. Hole U1519B was reentered at 2310 h, and the ACORK wellhead landed in the reentry cone on the seafloor at 0635 h on 16 April. Once the ACORK was released (0715 h), we recovered the subsea camera and deployed an ACORK free-fall funnel (FFF) at 0845 h (Figure **F3C**). To save time and avoid the complications encountered at Site U1518, we decided to not deploy a remotely operated vehicle (ROV) platform. The subsea camera was redeployed to verify that the FFF had landed correctly on top of the ACORK wellhead. The drill string with the mud motor, underreamer, and drill bit was recovered at 1605 h, and the BHA was cleaned with water.

In preparation for deploying a bridge plug at the bottom of the ACORK casing, the drill string was deployed with a 9⅞ inch drill bit BHA. Hole U1519B was reentered at 2100 h on 16 April with the aid

Figure F3. Site U1519 observatory installation. A. ACORK wellhead with pressure loggers and casing string with screens. B. ACORK drilling stinger assembly. mbrf = meters below rig floor. C. ACORK with FFF and bridge plug. D. CORK-II wellhead and casing string.

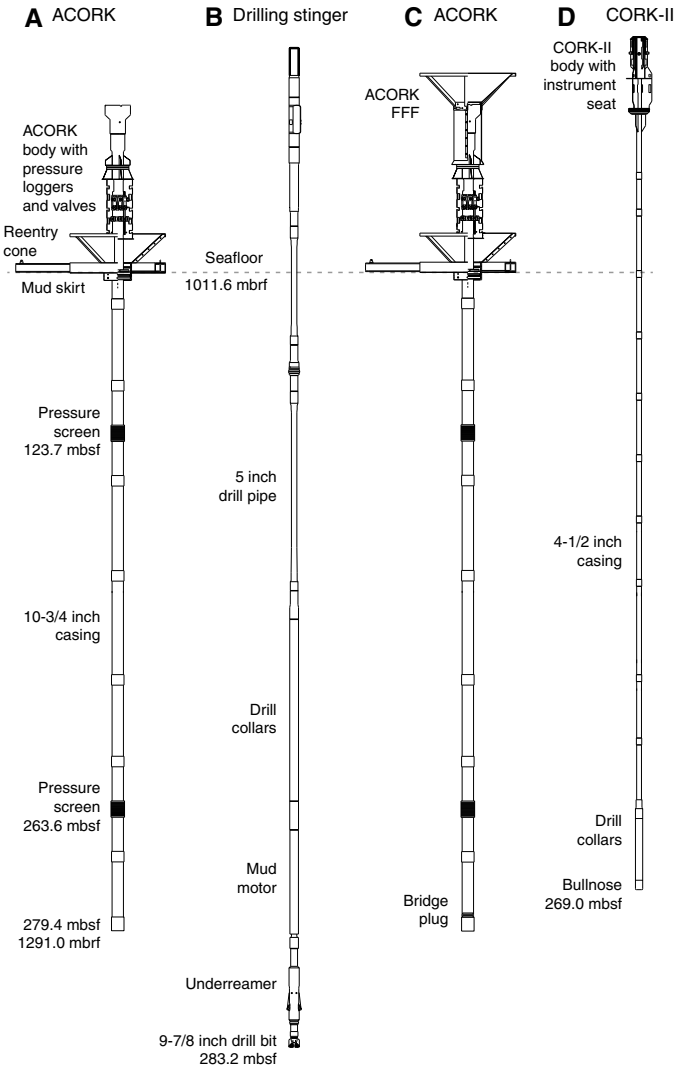

of the subsea camera, the hole was cleared of cuttings, and the drill string was recovered at 0315 h. Next, we assembled a BHA with a bridge plug to seal the bottom of the ACORK casing. The drill string was lowered to the seafloor, and the subsea camera was deployed to aid with the reentry. Hole U1519B was reentered at 0755 h on 17 April. The end of the drill string was positioned at 277 mbsf inside the ACORK casing, the bridge plug was activated until the packer was set at 1135 h (Figure **F3C**), and the bridge plug BHA was recovered at 1455 h.

Next, we started assembling the 269 m long CORK-II casing string consisting of 20 full joints and four pup joints of 4½ inch casing (~234 m), four 6¾ inch drill collars (~36 m), and a bullnose (Figure **F3D**). The CORK-II body and casing string were deployed with a J running tool, and the entire assembly was lowered to the seafloor. The subsea camera was deployed, and the CORK-II entered the ACORK funnel at 0120 h on 18 April. The CORK-II wellhead was lowered to ~20 m above the ACORK and kept there while we deployed the instrument string.

At 0230 h on 18 April, we started assembling the 268 m long instrument string consisting of a single segment of Spectra rope with 15 temperature sensors, one weak link, a sinker bar at the bottom, and a top plug. The top plug was connected to the Schlumberger wireline with the Electronic Release System (ERS), and the instrument string was lowered to the seafloor inside the drill pipe connected to the running tool. Once the top plug latched inside the CORK-II wellhead at 0530 h, the ERS mechanism was activated, releasing the instrument string. The CORK-II then landed inside the ACORK funnel at 0700 h and was released from the running tool at 0735 h on 18 April, completing the observatory installation. Following a brief visual survey of the wellhead, the camera and running tool BHA were recovered at 1100 h. In the inspection video, we noted minor damage on the CORK-II wellhead caused during the running tool release and a thick cover of cuttings over the hydraulic connections in the ACORK funnel, which should not pose a problem for future data recovery.

Hole U1519C

The primary coring objective at Site U1519 was to sample sediment in the intervals surrounding the ACORK pressure screens (around 124 and 264 mbsf) and in the lowermost sedimentary section logged in Hole U1519A (~520–640 mbsf). In preparation for coring, we assembled an RCB BHA. The drill string was lowered to the seafloor, and the vessel was offset 20 m from Hole U1519B at a heading of 122°. Hole U1519C (38°43.6483′S, 178°36.8773′E; 1000.3 mbsl; Table **T1**) was spudded at 1640 h on 18 April 2018, and drilling without core recovery continued to 108 mbsf until 0600 h on 19 April (drilled interval 375-U1519C-11). Cores 2R–26R advanced from 108.0 to 640.0 mbsf and recovered 119.17 m (55% recovery). This cored interval included two drilled intervals (375-U1519C-81 and 131) without coring at 163.6–250.0 and 288.4–518.4 mbsf, respectively. The drill string was recovered at 0815 h on 21 April, and the BHA was put away.

Hole U1519D

The final objective at Site U1519 was to core the shallow sedimentary section to sample interstitial water chemistry and collect in situ temperature measurements with the advanced piston corer temperature tool (APCT-3). An APC/extended core barrel (XCB) BHA was assembled, and the drill string was lowered to the seafloor. The vessel was offset 10 m at a heading of 122°, and Hole U1519D (38°43.6516′S, 178°36.8831′E; 1000.4 mbsl; Table **T1**) was spudded at 1505 h on 21 April 2018. Cores 375-U1519D-1H through 3H advanced from 0 to 23.3 mbsf and recovered 23.64 m (101% recovery). Nonmagnetic core barrels were used for all APC cores. Because coarse, unconsolidated material made it difficult to collect in situ temperature measurements and resulted in a partial stroke with Core 3H, we decided to start a new hole.

Hole U1519E

The vessel was offset 20 m at a heading of 122°, and Hole U1519E (38°43.6572′S, 178°36.8949′E; 1000.3 mbsl; Table **T1**) was spudded at 1845 h on 21 April 2018. Cores 375-U1519E-1H through 13F advanced from 0 to 85.8 mbsf and recovered 88.75 m (103% recovery). Nonmagnetic core barrels were used for all APC/half-length APC (HLAPC) cores. Formation temperature measurements were taken with the APCT-3 for Cores 4H–8H, 9F, 11F, and 13F.

Lithostratigraphy

We identified two lithostratigraphic units at Site U1519 (Table **T2**), which were informed to some extent by the petrophysical attributes of depth-correlative logging units in Hole U1519A drilled during Expedition 372 (Figure **F4**). Detailed characterization of lithofacies was hampered by large coring gaps, poor recovery, and pervasive coring disturbance. We used descriptive visual criteria to compare facies, and we did not define any subunits. The sedimentary strata at Site U1519 range in age from Holocene to early Pleistocene (see **Biostratigraphy**). Common lithologies include mud(stone), silt(stone), and sand(stone). Zones of soft-sediment deformation are also present.

Unit I

Interval: 375-U1519D-1H-1, 0 cm, and 375-U1519E-1H-1, 0 cm, to 375-U1519C-12R-3, 99 cm
Thickness: Holes U1519C–U1519E = 282.66 m
Depth: Holes U1519C–U1519E = 0–282.66 mbsf
Age: Holocene to late Middle Pleistocene
Lithology: mud(stone) and sparse silt(stone)

Coring of Lithostratigraphic Unit I started in Hole U1519C at 108 mbsf (Section 2R-1, 0 cm) and at the seafloor in Holes U1519D (Section 1H-1, 0 cm) and U1519E (Section 1H-1, 0 cm). The unit extends to 282.66 mbsf (Section 375-U1519C-12R-3, 99 cm). Cores from this depth range contain a background of dark greenish gray mud (silty clay to clayey silt) and mudstone with variable levels of consolidation. As explained in **Lithostratigraphy** in the Expedition 372B/375 methods chapter (Wallace et al., 2019), sediments in RCB cores are, by convention, called mudstone (Hole U1519C), whereas identical lithologies in APC cores (Hole U1519D) are called mud. We interpret these sediments to be typical hemipelagic suspension-fallout deposits alternating with very thin beds and laminae of silt. The uppermost part of Unit I (Cores 375-U1519D-1H and 375-U1519E-1H) contains a 1 m thick deposit of light gray, unconsolidated, silicic volcanic ash (Figure **F5**).

Seismic reflection records and high-resolution bathymetry are indicative of shallow mass transport remobilization at Site U1519 (see **Core-log-seismic integration**), similar to the Tuaheni Land-

Table T2. Lithostratigraphic units, Site U1519. **Download table in CSV format.**

Lith. unit	Hole, core, section, interval (cm) Top	Hole, core, section, interval (cm) Bottom	Depth (mbsf) Top	Depth (mbsf) Bottom	Thickness (m)	Stratigraphic age	Lithologic summary	Dominant processes of sedimentation
I	375-U1519D-1H-1, 0 U1519E-1H-1, 0	375-U1519C-12R-3, 99	0.00	282.66	282.66	Holocene to late Middle Pleistocene	Mud(stone), minor silt, and volcanic ash	Hemipelagic settling; interpretation hampered by poor recovery and coring disturbance
II	U1519C-12R-3, 99	U1519C-26R-CC, 5	282.66	635.65	352.99	Middle to early Pleistocene	Mudstone, silt(stone), sand(stone), and mass transport deposits	Hemipelagic settling, turbidity currents, submarine slides, debris flow

Figure F4. Lithostratigraphic summary, Site U1519. Core recovery: black = recovery, white = no recovery. Ages are defined by biostratigraphy (see Biostratigraphy). LWD data and logging units are also shown (see Logging while drilling). Correlations among lithostratigraphic units and logging units are hampered by gaps in coring, poor recovery, and drilling disturbance. TD = total depth.

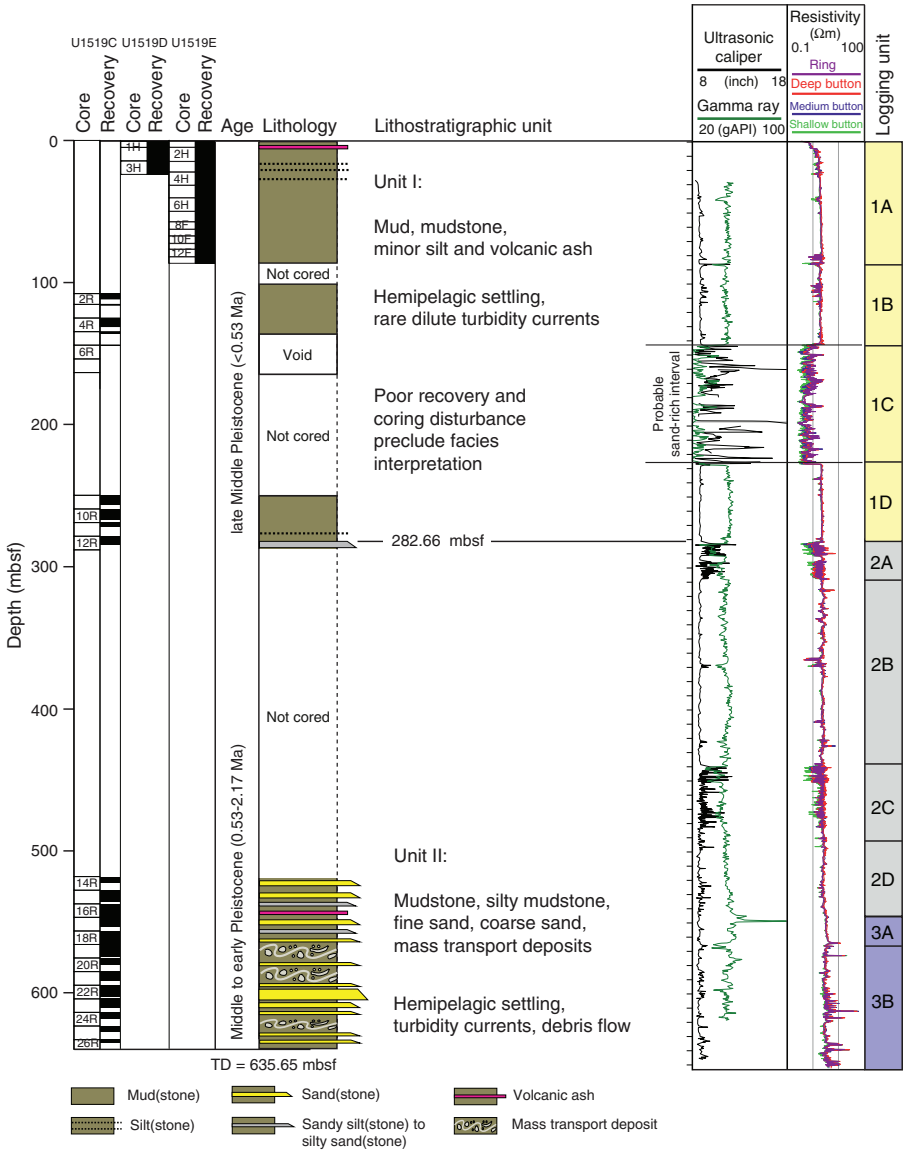

slide Complex that was cored at IODP Site U1517. The APC cores from Holes U1519D and U1519E, however, reveal no definitive diagnostic indicators of gravity-driven soft-sediment deformation in the hemipelagic mud. Recognition of such features might have been compromised by coring disturbance that consists mostly of upward arching of the sedimentary layers and vertical streaking from flow-in.

The shallow RCB cores from Hole U1519C are also overprinted by severe drilling artifacts. Internal sedimentary structures include dark silty laminae, but ubiquitous coring disruption broke most of the material into thin biscuits with truncated and rotated laminae. Normal size grading is preserved only locally, manifested as subtle changes in color. Irregular pods and distorted lenses of fine sand occur in one core (interval 375-U1519C-10R-1, 51–72 cm) (Figure **F6**).

Smear slides reveal that the detrital grain assemblage in the background mud(stone) lithology is dominated by clay minerals, with significant amounts of calcareous nannofossils, quartz, feldspar, and sedimentary lithic and volcaniclastic grains (Figure **F7**). Carbonate contents in mud(stone) specimens range from 0.4 to 12.1 wt% with an average value of 7.9 wt% (see **Geochemistry**). Normalized mineral abundances from bulk powder X-ray diffraction (XRD) analyses are shown in Figure **F8** and Table **T3**. Proportions of total clay minerals (smectite + illite + chlorite + kaolinite) range from 36.0 to 53.3 wt% (mean = 45.3 wt%). Quartz ranges from 23.7 to 37.5 wt% (mean = 29.5 wt%). Feldspar (plagioclase + K-feldspar) abundance ranges from 12.5 to 21.8 wt% (mean = 16.7 wt%), and calcite abundance ranges from 6.9 to 9.9 wt% (mean = 8.4 wt%). We recognize no significant trends in composition with depth.

Figure F5. Event bed thickness, Site U1519. Poor recovery, discontinuous coring, and widespread coring disturbance compromise the reliability of these data as indicators of sedimentary facies.

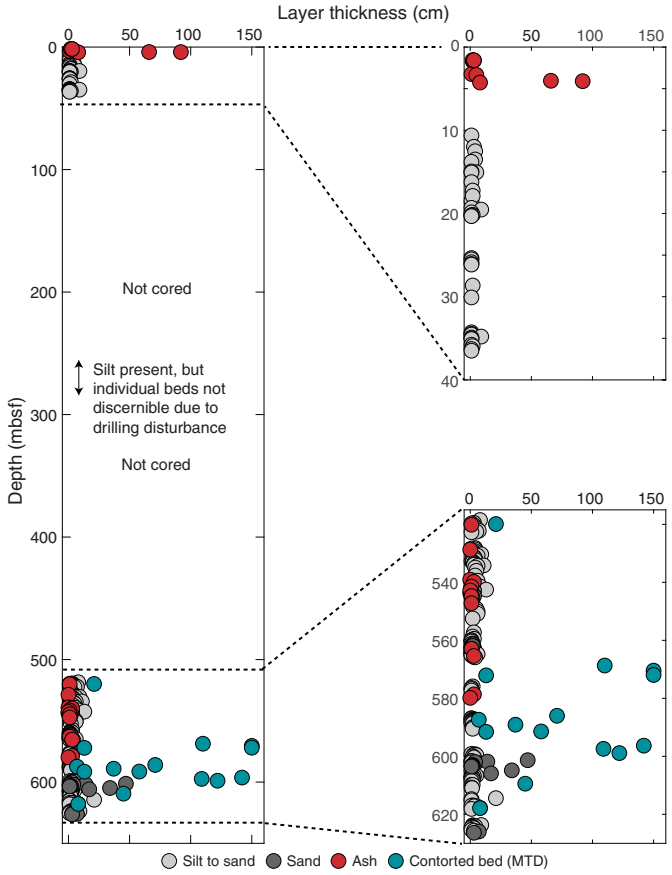

Figure F6. Representative Unit I and II lithologies, Hole U1519C. A. Mudstone with biscuiting and strong drilling disturbance that obscure any primary structure. B. Disrupted layers of fine sand (dashed lines) dispersed in mudstone, possibly representing coarser grained turbidite deposits.

Figure F7. Silt layers in Unit I, Hole U1519E. A, B. Quartz-feldspathic siltstone with calcareous bioclasts (foraminifers and nannofossils), volcanic glass, glauconite, and heavy minerals (3H-4, 110 cm; A: plane-polarized light [PPL]; B: cross-polarized light). C. Pyrite-rich siltstone (5H-4, 40 cm; PPL). D. Terrigenous organic fragments (3H-4, 110 cm; PPL).

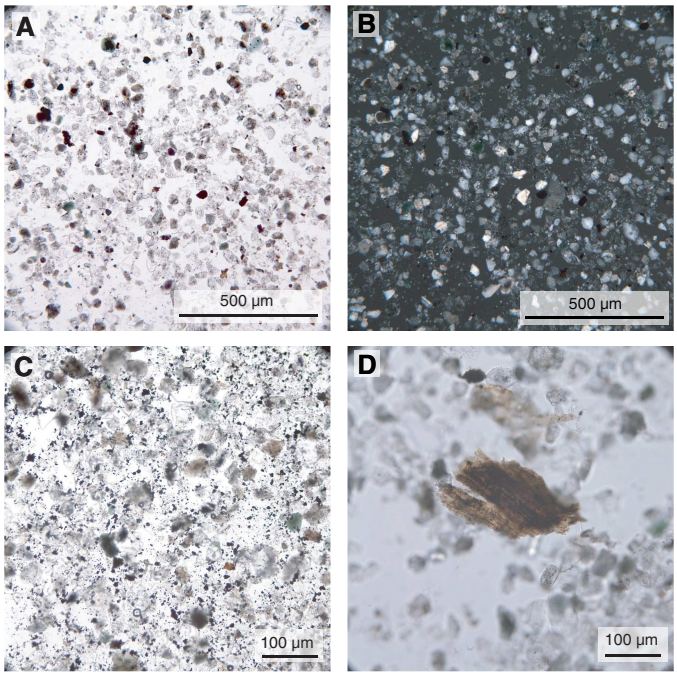

Unit II

Interval: 375-U1519C-12R-3, 99 cm, through 26R-CC
Thickness: 352.99 m
Depth: 282.66–635.65 mbsf
Age: Middle to early Pleistocene
Lithology: mudstone with scattered interbeds of silt(stone) and very fine sand(stone), medium to coarse sand(stone), contorted mudstone, and matrix-supported MTDs

We placed the upper boundary of Unit II in Section 375-U1519C-12R-3, 99 cm (282.66 mbsf), which is close to the top of Logging Unit 2 (281.5 mbsf). This unit boundary coincides with a noticeable change in color from dark greenish gray above to light greenish gray below, and the grain size coarsens somewhat to silt-rich mudstone. Plane-parallel laminae are more common and better preserved below the boundary. The upper part of Unit II also generates a positive excursion in magnetic susceptibility, and drilling disturbance is less severe. Below a 230 m gap in coring, Core 14R (518.4 mbsf) contains similar mudstone with scattered thin interbeds of dark gray sandy siltstone to very fine sandstone. Some of the coarser interbeds reach thicknesses of 5–10 cm (Figure **F5**) and include shell fragments and terrigenous organic matter. Most of the coarser interbeds display sharp bases and subtle normal grading.

Seismic reflection data exhibit geometry indicative of an unconformity at approximately 547 mbsf (see **Core-log-seismic integration**). However, no consequential changes in lithology or in the inferred processes of sedimentation occur over this depth range. Furthermore, the ages do not change across the seismically inter-

Figure F8. Lithostratigraphic summary and normalized mineral abundance from bulk powder XRD analyses, Site U1519. See Table T3 for data.

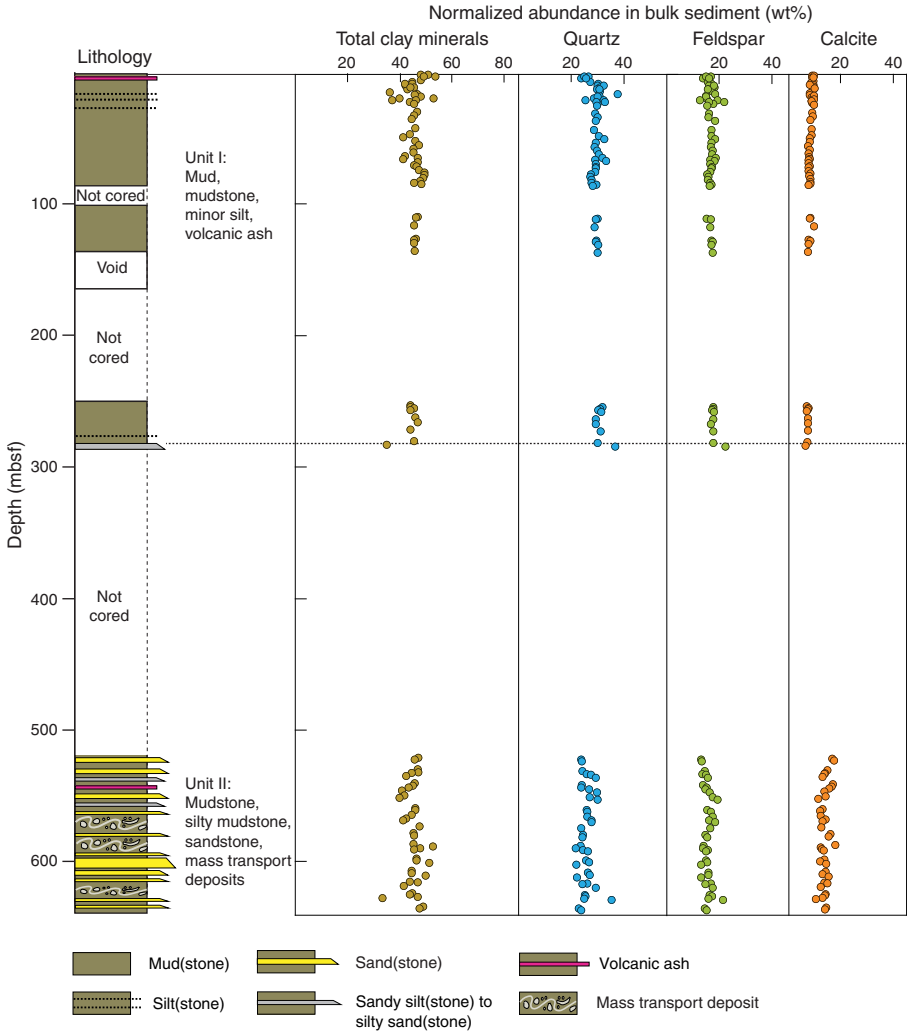

preted unconformity (see **Biostratigraphy**). At the top of Section 375-U1519C-19R-2, the mudstone displays clear evidence of soft-sediment deformation, including convolute laminae, mesoscale folds, dismembered bedding, and clasts of mudstone supported by a mudstone matrix. Zones of soft-sediment deformation also occur in Cores 21R and 22R (Figure **F9**). We interpret the deformed zones to be intraformational MTDs. The lithologies recovered from the remainder of Unit II consist of consolidated greenish gray mudstone interbedded with poorly indurated, uncemented sandy silt and sand. Some of the sandy sediment is medium to coarse grained and poorly sorted, with abundant shell fragments and sedimentary lithic grains. The most noteworthy examples are in Core 22R. Sandy beds in Core 23R are not as coarse; they display well-preserved bases and normal size grading. Core 23R also contains a distinctive matrix-supported conglomerate with widely dispersed clasts of mudstone (granule to pebble size and rounded to subrounded shapes) and small, intact shells of what appear to be shallow-water fauna.

Smear slide observations demonstrate that the detrital grain assemblage in the mudstones of Unit II is dominated by clay minerals, with significant amounts of silt- and sand-sized quartz, feldspar, sedimentary lithic and volcaniclastic grains, and calcareous nannofossils. Terrestrial organic matter is slightly more abundant than in Unit I. The sand deposits are composed largely of quartz and sedimentary rock fragments, although some are mixed with considerable amounts of volcanic glass shards and pumice. Carbonate contents in mudstone specimens range from 7.0 to 21.9 wt% with an average value of 11.2 wt% (see **Geochemistry**). Normalized mineral abundances from bulk powder XRD are shown in Figure **F8** and Table **T3**. Proportions of total clay minerals (smectite + illite + chlorite + kaolinite) range from 33.1 to 52.3 wt% (mean = 44.6 wt%). Quartz ranges from 21.7 to 36.6 wt% (mean = 25.9 wt%). Feldspar (plagioclase + K-feldspar) abundance ranges from 12.9 to 22.2 wt% (mean = 15.7 wt%), and calcite abundance ranges from 6.5 to 17.9 wt% (mean = 13.8 wt%).

Comparison of Holes U1519C–U1519E core data and Hole U1519A log data

In general, logging data provide an uninterrupted record of stratigraphic variability at Site U1519 (see **Logging while drilling**). Correlation between lithostratigraphic units and logging units, however, was compromised by spot coring, poor recovery, and coring disturbance (Figure **F4**). Logging Unit 1 in Hole U1519A (0–281.5 mbsf) shows petrophysical characteristics typical of fine- and coarse-grained lithologies. It is divided into four subunits based on changes in logging response. Subunit 1A (0–86 mbsf) consists of uniformly fine grained sediment. APC cores from Lithostrati-

Table T3. Bulk-powder X-ray diffraction results, Site U1519. Integrated peak areas from MacDiff software. Relative abundance computed using regression equations (see Figure F12 in the Expedition 372B/375 methods chapter [Wallace et al., 2019]). Volc. = volcanic. TCM = total clay minerals, Qtz = quartz, Feld = feldspar, Cal = calcite. (Continued on next page.) **Download table in CSV format.**

Core, section, interval (cm)	Depth (mbsf)	Lithology	Peak intensity (counts/step)				Integrated peak area (total counts)				Relative abundance (wt%)					Normalized abundance (wt%)			
			TCM	Qtz	Feld	Cal	TCM	Qtz	Feld	Cal	TCM	Qtz	Feld	Cal	Total	TCM	Qtz	Feld	Cal
Unit I																			
375-U1519D-																			
1H-1, 127	1.23	Mud	625	10,754	2,493	1,897	24,103	153,288	71,650	31,588	37.3	20.7	13.0	7.2	78.1	47.7	26.5	16.6	9.2
1H-2, 127	2.74	Mud	821	10,319	2,343	1,969	31,400	150,306	64,651	34,712	45.8	20.3	11.8	7.9	85.8	53.3	23.7	13.8	9.2
1H-3, 90	3.88	Volc. ash	Mostly amorphous volcanic glass																
2H-1, 127	5.50	Mud	798	12,054	2,708	2,230	26,920	174,337	74,207	36,161	40.7	23.2	13.4	8.3	85.5	47.6	27.1	15.6	9.6
2H-2, 129	6.97	Mud	715	14,091	2,997	1,919	24,778	197,827	80,994	32,563	38.1	26.0	14.5	7.4	85.9	44.4	30.2	16.9	8.6
2H-3, 127	8.42	Mud	771	14,540	3,168	2,193	26,524	206,669	80,369	37,433	40.2	27.0	14.4	8.6	90.2	44.6	29.9	15.9	9.5
2H-4, 127	9.87	Mud	701	14,156	3,518	2,059	22,557	197,774	85,072	34,619	35.3	25.9	15.1	7.9	84.2	41.9	30.8	18.0	9.4
2H-5, 127	11.33	Mud	736	14,165	2,980	2,091	26,503	201,591	77,769	37,395	40.2	26.4	14.0	8.6	89.1	45.1	29.6	15.7	9.6
2H-6, 122	12.73	Mud	694	14,888	3,394	2,014	24,735	211,430	86,193	36,196	38.1	27.5	15.3	8.3	89.2	42.7	30.9	17.2	9.3
3H-1, 122	14.99	Mud	529	18,026	3,429	1,643	19,374	253,173	89,546	31,047	31.0	32.3	15.9	7.0	86.1	36.0	37.5	18.4	8.2
3H-2, 112	16.45	Mud	758	15,330	2,951	1,851	27,916	213,392	74,656	32,837	41.9	27.8	13.5	7.5	90.5	46.3	30.7	14.9	8.2
3H-3, 118	18.00	Mud	770	13,382	2,844	1,778	28,816	194,463	74,529	34,388	42.9	25.6	13.4	7.8	89.7	47.8	28.5	15.0	8.7
3H-4, 118	19.54	Mud	627	14,315	3,696	1,741	21,001	207,411	91,241	33,118	33.2	27.1	16.1	7.5	83.9	39.6	32.2	19.2	9.0
3H-5, 117	21.08	Mud	649	15,724	4,786	1,977	20,671	224,770	112,004	34,439	32.8	29.1	19.4	7.8	89.1	36.8	32.6	21.8	8.8
3H-6, 100	22.42	Mud	753	14,646	3,708	2,025	25,629	204,835	89,852	35,675	39.2	26.8	15.9	8.1	90.0	43.5	29.8	17.7	9.0
375-U1519E-																			
1H-1, 124	1.23	Mud	802	10,334	2,497	2,014	28,090	153,184	68,026	35,227	42.1	20.7	12.4	8.0	83.2	50.6	24.9	14.9	9.7
1H-2, 124	2.72	Mud	759	10,312	2,733	1,973	26,312	155,695	73,230	34,108	40.0	21.0	13.2	7.8	81.9	48.8	25.6	16.1	9.5
2H-3, 108	8.38	Mud	675	15,688	3,446	1,842	24,163	222,429	90,657	32,559	37.3	28.8	16.0	7.4	89.5	41.7	32.2	17.9	8.2
2H-5, 109	11.13	Mud	775	15,628	3,174	2,096	26,491	216,686	79,487	39,581	40.2	28.1	14.2	9.1	91.7	43.9	30.7	15.5	9.9
3H-2, 110	16.56	Mud	765	14,225	2,832	2,026	27,138	206,399	74,814	38,588	41.0	26.9	13.5	8.8	90.2	45.4	29.9	14.9	9.8
3H-4, 113	19.42	Mud	896	11,303	2,138	1,994	30,945	161,685	58,145	37,052	45.3	21.7	10.8	8.5	86.2	52.5	25.2	12.5	9.8
3H-5, 97	20.72	Mud	759	14,141	3,018	1,977	27,423	203,361	80,590	34,928	41.3	26.6	14.4	8.0	90.3	45.8	29.5	16.0	8.8
4H-2, 93	23.70	Mud	730	13,435	2,820	2,021	25,093	190,786	71,634	36,446	38.5	25.1	13.0	8.3	84.9	45.3	29.6	15.3	9.8
4H-6, 108	29.59	Mud	780	13,252	3,042	1,880	26,625	191,304	77,060	34,537	40.4	25.2	13.8	7.9	87.3	46.3	28.9	15.9	9.0
5H-1, 100	32.29	Mud	724	13,527	2,850	1,885	25,321	196,065	74,925	34,965	38.8	25.7	13.5	8.0	86.0	45.1	29.9	15.7	9.3
5H-3, 110	35.14	Mud	773	14,662	4,177	1,961	27,331	207,859	97,269	34,466	41.2	27.1	17.1	7.8	93.2	44.2	29.1	18.3	8.4
6H-2, 84	42.21	Mud	778	13,816	3,231	1,962	27,385	196,430	85,766	35,457	41.3	25.8	15.2	8.1	90.4	45.7	28.5	16.9	8.9
6H-6, 2	46.81	Mud	718	14,656	3,283	1,926	25,508	208,565	85,539	35,012	39.0	27.2	15.2	8.0	89.4	43.6	30.4	17.0	8.9
6H-7, 92	48.99	Mud	709	16,923	3,677	1,916	24,963	235,421	98,207	33,398	38.3	30.3	17.2	7.6	93.4	41.0	32.4	18.4	8.1
7H-2, 100	51.88	Mud	748	13,459	3,142	1,751	25,790	192,229	81,367	31,117	39.4	25.3	14.5	7.0	86.2	45.6	29.3	16.9	8.2
7H-4, 108	54.92	Mud	764	13,104	3,013	1,676	26,932	189,099	80,765	28,823	40.7	24.9	14.4	6.5	86.6	47.0	28.8	16.7	7.5
8H-1, 86	57.85	Mud	737	13,776	3,343	1,716	25,479	196,264	83,998	30,714	39.0	25.8	15.0	6.9	86.7	45.0	29.7	17.3	8.0
8H-3, 62	60.35	Mud	712	13,914	3,149	1,681	24,732	196,815	81,386	28,683	38.1	25.8	14.5	6.5	84.9	44.8	30.4	17.1	7.6
9F-1, 100	63.17	Mud	734	15,586	3,804	1,740	24,134	219,552	94,659	31,169	37.3	28.5	16.7	7.1	89.5	41.7	31.8	18.6	7.9
9F-2, 125	64.67	Mud	724	13,220	3,071	1,720	26,181	188,464	78,842	30,440	39.8	24.9	14.1	6.9	85.7	46.5	29.0	16.5	8.0
9F-3, 80	65.53	Mud	667	15,334	3,487	1,581	22,321	217,160	87,455	28,674	35.0	28.2	15.5	6.5	85.1	41.1	33.1	18.2	7.6
10F-1, 128	68.17	Mud	768	13,191	3,012	1,720	26,218	190,726	78,560	29,828	39.9	25.1	14.1	6.7	85.8	46.5	29.3	16.4	7.8
10F-3, 79	70.50	Mud	744	13,043	3,254	1,710	24,347	183,515	79,818	30,214	37.6	24.3	14.3	6.8	83.0	45.3	29.3	17.2	8.2
10F-4, 42	71.28	Mud	745	13,659	3,322	1,699	26,646	194,491	82,735	30,395	40.4	25.6	14.8	6.9	87.6	46.1	29.2	16.9	7.8
11F-2, 96	73.93	Mud	744	13,147	3,103	1,773	26,592	188,192	79,130	29,731	40.3	24.8	14.2	6.7	86.0	46.9	28.9	16.5	7.8
11F-4, 41	75.69	Mud	799	12,660	2,839	1,783	29,066	181,120	74,641	32,002	43.2	24.0	13.5	7.3	87.9	49.2	27.3	15.3	8.3
12F-1, 129	77.55	Mud	810	12,446	3,002	1,785	28,995	180,718	77,625	30,892	43.1	23.9	13.9	7.0	88.0	49.0	27.2	15.8	7.9
12F-3, 74	79.86	Mud	856	13,025	2,949	1,856	29,393	186,929	77,872	33,014	43.6	24.7	14.0	7.5	89.7	48.6	27.5	15.6	8.4
13F-1, 129	82.28	Mud	796	12,518	3,131	2,009	26,660	177,283	78,345	32,149	40.4	23.5	14.1	7.3	85.3	47.4	27.6	16.5	8.5
13F-2, 123	83.62	Mud	735	13,103	3,137	1,888	24,494	185,576	78,338	31,142	37.8	24.5	14.0	7.0	83.4	45.3	29.4	16.9	8.5
13F-3, 69	84.47	Mud	763	12,536	3,105	1,559	27,445	182,939	78,354	28,989	41.3	24.2	14.1	6.5	86.1	48.0	28.1	16.3	7.6
375-U1519C-																			
2R-1, 149	109.48	Mud	782	14,301	2,940	1,891	27,413	201,699	74,089	33,346	41.3	26.4	13.4	7.6	88.6	46.6	29.8	15.1	8.5
2R-2, 54	110.03	Mud	779	13,625	3,164	1,824	26,419	193,217	81,198	31,576	40.1	25.4	14.5	7.2	87.2	46.0	29.1	16.6	8.2
3R-1, 25	115.85	Mud	752	12,605	2,968	2,254	23,911	178,285	74,765	34,894	37.0	23.7	13.5	7.9	82.1	45.1	28.8	16.4	9.7
4R-1, 109	126.29	Mud	747	13,544	3,183	1,612	26,069	192,592	81,675	29,347	39.7	25.3	14.6	6.6	86.2	46.0	29.4	16.9	7.7
4R-2, 24	126.94	Mud	713	12,962	3,085	1,717	24,942	186,408	81,896	31,001	38.3	24.6	14.6	7.0	84.6	45.3	29.1	17.3	8.3
4R-3, 111	129.27	Mud	717	13,985	3,143	1,654	25,633	199,197	82,392	29,545	39.2	26.1	14.7	6.7	86.6	45.2	30.1	17.0	7.7
5R-1, 58	135.40	Mud	708	13,791	3,207	1,565	25,571	196,507	83,608	28,294	39.1	25.8	14.9	6.4	86.2	45.4	29.9	17.3	7.4
9R-2, 135	252.81	Mud	739	14,872	3,331	1,509	24,487	209,668	85,685	26,608	37.7	27.3	15.2	6.0	86.3	43.7	31.7	17.7	6.9
9R-3, 134	254.34	Mud	775	15,805	3,517	1,760	26,552	219,059	91,400	31,736	40.3	28.4	16.2	7.2	92.0	43.8	30.9	17.6	7.8
9R-4, 50	254.98	Mud	739	14,070	3,234	1,608	25,629	197,962	82,699	28,790	39.2	26.0	14.8	6.5	86.4	45.3	30.1	17.1	7.5
9R-5, 128	256.43	Mud	690	13,858	3,227	1,502	23,264	198,083	83,112	26,238	36.2	26.0	14.8	5.9	82.9	43.7	31.3	17.9	7.1
10R-2, 115	262.25	Mud	750	13,061	3,332	1,692	24,969	187,343	83,694	28,091	38.3	24.7	14.9	6.3	84.3	45.5	29.3	17.7	7.5
10R-5, 1	265.52	Mud	730	13,151	3,091	1,539	25,739	187,870	79,447	27,870	39.3	24.8	14.2	6.3	84.6	46.5	29.3	16.8	7.4
11R-2, 75	271.43	Mud	757	14,900	3,491	1,619	25,320	210,008	88,365	29,102	38.8	27.4	15.7	6.6	88.4	43.9	31.0	17.7	7.4
12R-1, 117	279.99	Mud	725	13,712	3,287	1,613	25,049	194,290	84,962	27,471	38.4	25.5	15.1	6.2	85.3	45.1	29.9	17.7	7.2
															Unit I mean:	45.3	29.5	16.7	8.4

Table T3 (continued).

Core, section, interval (cm)	Depth (mbsf)	Lithology	Peak intensity (counts/step)				Integrated peak area (total counts)				Relative abundance (wt%)					Normalized abundance (wt%)			
			TCM	Qtz	Feld	Cal	TCM	Qtz	Feld	Cal	TCM	Qtz	Feld	Cal	Total	TCM	Qtz	Feld	Cal
Unit II																			
12R-3, 133	282.98	Mud	548	17,739	4,493	1,305	18,522	245,359	109,926	24,822	29.8	31.4	19.1	5.6	85.8	34.7	36.6	22.2	6.5
14R-3, 1	520.54	Mud	737	10,694	2,342	3,417	27,354	154,361	62,790	61,271	41.2	20.8	11.5	14.6	88.2	46.8	23.6	13.1	16.6
14R-4, 71	522.19	Mud	690	10,572	2,354	3,553	25,608	152,049	62,608	62,646	39.1	20.5	11.5	15.0	86.1	45.4	23.8	13.3	17.4
15R-2, 25	529.73	Mud	741	10,896	2,593	3,118	27,101	158,037	68,995	55,029	40.9	21.3	12.5	13.0	87.7	46.7	24.2	14.3	14.8
15R-3, 77	531.78	Mud	732	12,185	2,504	3,118	27,623	171,764	65,853	52,726	41.5	22.9	12.0	12.4	88.8	46.8	25.8	13.5	13.9
15R-4, 43	532.45	Mud	636	12,516	2,569	2,721	25,011	178,556	70,757	50,377	38.4	23.7	12.8	11.8	86.7	44.3	27.3	14.8	13.6
15R-6, 1	534.54	Mud	646	13,389	2,810	2,722	23,418	191,227	73,875	48,306	36.4	25.2	13.3	11.3	86.2	42.2	29.2	15.5	13.1
16R-2, 121	540.29	Mud	676	10,874	2,301	3,519	25,953	154,447	65,207	61,866	39.6	20.8	11.9	14.8	87.1	45.4	23.9	13.7	17.0
16R-3, 127	541.82	Mud	555	9,092	2,253	2,880	21,926	133,199	63,255	53,854	34.4	18.3	11.6	12.7	77.0	44.7	23.7	15.1	16.5
16R-4, 129	543.35	Mud	620	11,526	2,448	2,993	22,821	163,841	66,543	54,756	35.6	22.0	12.1	12.9	82.6	43.1	26.6	14.7	15.6
16R-6, 67	545.50	Mud	587	12,797	2,917	2,752	20,853	182,222	73,794	47,569	33.0	24.1	13.3	11.1	81.5	40.5	29.6	16.3	13.6
17R-2, 87	549.42	Mud	633	12,162	3,204	3,211	22,717	172,415	83,842	51,477	35.5	23.0	14.9	12.1	85.5	41.5	26.9	17.5	14.1
17R-3, 109	551.04	Mud	637	14,068	3,726	2,393	21,614	195,827	94,515	42,335	34.0	25.7	16.6	9.8	86.2	39.5	29.8	19.3	11.3
18R-2, 80	558.99	Mud	738	11,270	2,812	2,938	25,328	163,366	72,270	47,735	38.8	21.9	13.1	11.1	84.9	45.7	25.8	15.4	13.1
18R-3, 123	560.50	Mud	722	11,608	3,194	2,821	25,628	166,286	79,768	44,576	39.2	22.2	14.3	10.3	86.0	45.5	25.9	16.6	12.0
18R-6, 59	564.24	Mud	642	10,984	3,387	2,648	23,478	159,225	80,302	43,700	36.5	21.4	14.4	10.1	82.3	44.3	26.0	17.4	12.3
19R-1, 101	567.20	Mud	656	12,281	2,925	3,188	22,295	170,688	73,977	50,332	34.9	22.8	13.3	11.8	82.8	42.2	27.5	16.1	14.2
19R-2, 109	568.66	Mud	629	12,468	3,564	3,113	22,171	176,516	88,111	47,589	34.8	23.5	15.6	11.1	84.9	40.9	27.6	18.4	13.0
19R-5, 117	573.10	Mud	579	9,018	2,317	2,664	23,026	130,995	68,258	41,575	35.9	18.0	12.4	9.6	75.9	47.3	23.7	16.4	12.6
20R-2, 101	577.95	Mud	693	10,903	2,675	3,407	25,447	157,546	70,022	58,957	38.9	21.2	12.7	14.0	86.8	44.8	24.4	14.6	16.1
20R-4, 1	579.81	Mud	633	10,086	2,598	3,021	23,986	145,432	68,788	53,289	37.1	19.7	12.5	12.5	81.9	45.3	24.1	15.3	15.3
21R-1, 89	586.17	Mud	634	9,774	2,301	3,080	23,660	138,962	61,430	61,241	36.7	19.0	11.3	14.6	81.6	45.0	23.3	13.9	17.9
21R-3, 67	588.25	Mud	650	8,164	2,051	2,289	26,499	120,136	57,444	40,745	40.2	16.7	10.6	9.4	76.9	52.3	21.7	13.8	12.2
21R-5, 2	589.65	Mud	714	10,368	2,768	2,655	26,031	150,405	71,286	45,618	39.6	20.3	12.9	10.6	83.5	47.5	24.4	15.5	12.7
21R-5, 96	590.52	Mud	694	11,291	2,620	2,851	24,214	161,406	67,633	48,001	37.4	21.7	12.3	11.2	82.6	45.3	26.2	14.9	13.5
22R-2, 108	597.37	Mud	661	10,819	2,622	2,659	25,010	157,269	67,802	48,516	38.4	21.2	12.3	11.3	83.2	46.1	25.4	14.8	13.6
22R-3, 118	598.86	Mud	653	10,888	2,537	2,296	23,654	157,521	66,402	41,704	36.7	21.2	12.1	9.6	79.6	46.1	26.6	15.2	12.1
22R-6, 3	600.71	Mud	825	9,577	2,261	3,039	30,004	138,950	61,174	53,373	44.3	19.0	11.3	12.6	87.0	50.9	21.8	12.9	14.4
23R-3, 1	606.59	Mud	642	11,162	2,690	2,797	22,930	157,997	70,298	48,904	35.8	21.3	12.7	11.4	81.2	44.1	26.2	15.7	14.1
23R-4, 69	608.67	Mud	744	12,680	3,060	2,969	25,691	179,760	77,323	49,718	39.2	23.8	13.9	11.6	88.6	44.3	26.9	15.7	13.1
23R-6, 23	610.27	Mud	738	8,931	2,243	3,166	26,861	130,866	58,211	53,613	40.6	18.0	10.8	12.6	82.0	49.6	21.9	13.1	15.4
24R-1, 102	614.96	Mud	682	11,219	3,261	2,806	23,643	162,733	78,772	49,487	36.7	21.8	14.1	11.6	84.2	43.6	25.9	16.8	13.7
24R-2, 31	615.55	Mud	691	9,985	2,577	2,945	25,134	146,384	65,369	51,929	38.5	19.9	11.9	12.2	82.5	46.7	24.1	14.5	14.8
24R-4, 64	618.53	Mud	629	13,010	3,137	2,556	21,723	181,690	80,386	44,127	34.2	24.1	14.4	10.2	82.8	41.3	29.1	17.4	12.3
25R-1, 45	624.04	Mud	716	11,285	3,318	3,025	25,746	164,793	80,327	53,219	39.3	22.1	14.4	12.5	88.2	44.5	25.0	16.3	14.2
25R-2, 53	624.72	Mud	672	11,305	3,558	2,978	24,697	163,910	84,219	52,006	38.0	22.0	15.0	12.2	87.2	43.6	25.2	17.2	14.0
25R-3, 124	626.47	Mud	743	10,722	3,105	2,644	26,087	155,977	74,229	47,294	39.7	21.0	13.4	11.0	85.1	46.7	24.7	15.7	12.9
25R-4, 63	627.32	Mud	411	14,809	3,835	2,191	15,312	203,901	91,408	34,610	25.1	26.7	16.2	7.9	75.8	33.1	35.2	21.3	10.4
26R-1, 69	633.89	Mud	741	9,353	2,622	2,982	26,758	138,422	65,290	51,320	40.5	18.9	11.9	12.0	83.4	48.6	22.7	14.3	14.4
26R-2, 112	635.37	Mud	762	10,719	3,000	2,949	27,695	154,441	73,474	52,389	41.6	20.8	13.3	12.3	88.0	47.3	23.7	15.1	14.0
															Unit II mean:	44.6	25.9	15.7	13.8

graphic Unit I confirm this interpretation. Subunit 1B (86–143 mbsf) is defined based on a change to slightly lower resistivity, thin beds, and small washouts in the coarse-grained thin beds. Coring disturbance in Hole U1519C is too extensive to corroborate the occurrences of thin interbeds (probable turbidites). Subunit 1C (143–227.5 mbsf) is interpreted to comprise coarse-grained sediment with extensive washouts. We failed to recover sediment from this interval (Cores 375-U1519C-6R and 7R). Subunit 1D (227.5–281.5 mbsf) marks a return to the lithologic character of Subunit 1B. Cores from the upper part of Lithostratigraphic Unit II, although highly disturbed, are consistent with this interpretation; we find remnants of fine sand layers scattered as pods in the mudstone.

Logging Unit 2 (281.5–546 mbsf) is thought to comprise a sequence of mostly fine grained sediments punctuated by coarser interbeds. Four subunits were defined over this depth interval (Figure **F4**). Subunit 2A (281.5–308.5 mbsf) is interpreted to consist of coarser sediment content and larger pore sizes separated by a thin interval of uniform fine sediment. Bed thickness and contrasts among interbeds are variable. These deposits are interpreted to be thin-bedded turbidites. One bed of silty sand to sandy silt was recovered just below the top of Unit II. Subunit 2B (308.5–438.5 mbsf) is interpreted to consist of uniformly fine grained sediment. No coring was attempted in that interval. Subunit 2C (438.5–483.0 mbsf) marks another interval of inferred thin-bedded turbidites with layers as thick as 10 cm. That interval was not cored. LWD results from Subunit 2D (483.0–546 mbsf) are indicative of more uniformly fine grained sediment with sparse thin layers of coarser sediment. The lithologies in Cores 375-U1519C-14R through 17R are consistent with that interpretation, but they are not fundamentally different than the lithologies in Core 19R and below.

Lithologic interpretation of Logging Unit 3 (546–650 mbsf) is dubious. Unit 3 is interpreted to consist of uniformly fine grained sediment. Distinctions between two logging subunits (3A and 3B) are based on small differences in compressional wave velocity, density, and resistivity values. Subunit 3A (546–567 mbsf) is characterized by higher resistivity, lower porosity, and higher density. Subunit 3B (567–650 mbsf) yields evidence for a gradational change to slightly higher porosity values and slower velocity values. These subtle differences in petrophysical attributes are not detectable at either the mesoscale or microscale in the cored lithologies. Cores

Figure F9. Examples of soft-sediment deformation in Unit II, Hole U1519C. Dashed lines highlight contorted layer contacts. A. Greenish gray contorted mudstone with darker gray mudstone (Ms) clasts and sandstone (Ss) clasts. B. Contorted mudstone.

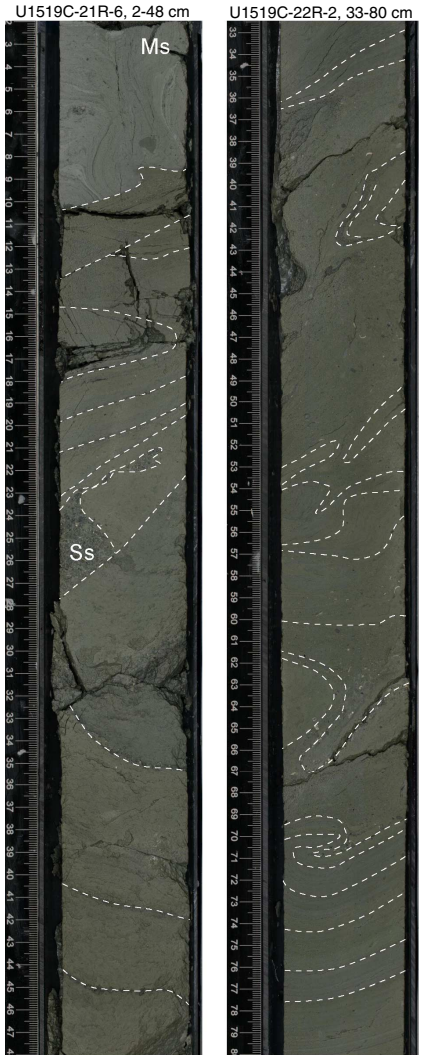

confirm that mudstone is the most common lithology from many meters above the top of Logging Unit 3 through Section 375-U1519C-26R-CC, but we also recovered a substantial number of coarser interbeds throughout the depth range of Unit 3. Some of these layers are similar in texture, thickness, and composition to those in the overlying depth range of Unit 2, but the more distinctive sand beds are considerably thicker and include medium and very coarse grain sizes. The recovery of thicker and coarser sand beds, particularly in Core 22R, coincides with a broader zone of increased resistivity and positive resistivity spikes in the LWD logs. The occurrences of MTDs and pebbly mudstone are not detected in any of the log attributes, even as anomalous zones of bedding dips.

Biostratigraphy

Planktonic foraminifers and calcareous nannofossils from core catcher samples and additional split-core samples from Holes U1519C–U1519E were examined to develop a shipboard biostratigraphic framework for Site U1519. Additionally, benthic foraminifers provided data on paleowater depths and downslope reworking.

A Holocene to Pleistocene sedimentary sequence was recovered at Site U1519. The base of the Holocene was identified between Samples 375-U1519E-1H-CC, 8–18 cm (4.40 mbsf), and 2H-CC, 14–24 cm (14.00 mbsf). The underlying section (to Sample 375-U1519C-15R-CC, 10–19 cm [536.32 mbsf]) is dated Late to Middle Pleistocene (Haweran to Castlecliffian; 0.011–0.62 Ma), indicating a sedimentation rate of 0.84 m/ky. The age through the lower part of the section to the base of Hole U1519C is poorly constrained but is shown by calcareous nannofossils and planktonic foraminifers to be early Pleistocene or younger (younger than 1.73 Ma and younger than 2.17 Ma, respectively).

Highly variable planktonic foraminifer abundances in the upper part of the cored section (Samples 375-U1519E-1H-1, 0 cm, through 15R-CC, 10–19 cm [0–536.32 mbsf]) fluctuate between outer neritic and oceanic values. This variability is attributed to downslope reworking that is evident from the occurrence of common inner shelf benthic taxa and shell fragments with bathyal benthic taxa in the same sample (e.g., 375-U1519C-15R-CC, 10–19 cm [536.32 mbsf]). In the lower part of the cored sequence (Samples 16R-CC, 0–11 cm, through 26R-CC, 0–5 cm [546.86–635.6 mbsf]), benthic markers indicate deposition in mid- to lower bathyal or deeper water depths.

Calcareous nannofossils

Calcareous nannofossil biostratigraphy at Site U1519 was established through the analysis of core catcher samples from Holes U1519C and U1519E. Nannofossils are common throughout the cored sequence, with poor to moderate preservation. Reworking of older, poorly preserved material is common in most samples. Biostratigraphic datums are given in Table **T4**, and the distribution of calcareous nannofossil taxa is shown in Table **T5**.

Split-core samples from Hole U1519E were analyzed under a scanning electron microscope to determine the presence/absence of *Emiliania huxleyi*. The presence of *E. huxleyi* in Samples 375-U1519E-1H-1, 4 cm, through 2H-1, 52 cm (0.04–5.12 mbsf), indicates a Late Pleistocene to Holocene age (0.29 Ma or younger) in Zone NN21 of Martini (1971). Below 5.12 mbsf, the recognition of key datums is problematic because of substantial reworking of Pliocene–Eocene taxa throughout the sequence.

Medium *Gephyrocapsa* spp. (4–5.55 µm) are recorded sporadically throughout Holes U1519C and U1519E. Based on the first appearance datum of medium *Gephyrocapsa* spp. (1.73 Ma or younger; in Zone NN19), the base of Hole U1519C (Sample 375-U1519C-26R-CC, 0–5 cm [635.60 mbsf]) is assigned an early Pleistocene or younger age.

Other taxa in the Pleistocene sequence include rare to common specimens of *Coccolithus pelagicus, Gephyrocapsa* spp. (<3.5 µm), *Helicosphaera carteri, Pseudoemiliania lacunosa, Pseudoemiliania ovata, Reticulofenestra haqii, Reticulofenestra minuta, Reticulofenestra minutula, Reticulofenestra producta*, and *Syracosphaera pulchra* and rare to few specimens of *Braarudosphaera bigelowii, Calcidiscus leptoporus, Calcidiscus tropicus, Calciosolenia brasiliensis, Ceratolithus cristatus, Gephyrocapsa* spp. (>5.5 µm), *Helicosphaera hyalina, Helicosphaera sellii, Pontosphaera discopora, Pontosphaera japonica, Pontosphaera multipora, Reticulofenestra perplexa, Rhabdosphaera clavigera, Umbilicosphaera rotula*, and *Umbilicosphaera sibogae*.

Table T4. Calcareous nannofossil and planktonic foraminifer datums and ages, Site U1519. B = base, Bc = base common. MIS = marine isotope stage. PF = planktonic foraminifer, CN = calcareous nannofossil. NN zones are from Martini (1971). New Zealand (NZ) stage: Wq = Haweran, Wc = Castlecliffian, Wn = Nukumaruan. **Download table in CSV format.**

Calcareous nannofossil and planktonic foraminifer datum	Fossil group	Age (Ma)	NN zone or NZ stage	Top core, section, interval (cm)	Top depth CSF-B (m)	Bottom core, section, interval (cm)	Bottom depth CSF-B (m)	Midpoint depth CSF-B (m)	± (m)
				375-U1519E-		375-U1519E-			
Base *Hirsutella hirsuta* MIS 1 subzone	PF	0.011	Wq	1H-CC, 8–18	4.40	2H-CC, 14–24	14.00	9.20	4.8
B *Emiliania huxleyi*	CN	≤0.29	NN21	2H-1, 52	5.12	2H-1, 106	5.66	5.39	0.27
				375-U1519C-		375-U1519C-			
Base sinistral zone *Truncorotalia truncatulinoides*	PF	≤0.53	Wq-Wc	12R-CC, 6–16	284.70	14R-CC, 0–15	522.39	403.54	118.84
Top dextral zone *Truncorotalia truncatulinoides*	PF	≥0.53	Wc-Wn	12R-CC, 6–16	284.70	14R-CC, 0–15	522.39	403.54	118.84
Bc *Truncorotalia truncatulinoides*	PF	0.62	Wc	15R-CC, 10–19	536.32	16R-CC, 0–11	546.86	541.59	5.27
B medium *Gephyrocapsa* spp.	CN	≤1.73	NN19	26R-CC, 0–5	635.60	Below hole			
B *Truncorotalia truncatulinoides*	PF	≤2.17	Wc-Wn	26R-CC, 0–5	635.60	Below hole			

Table T5. Distribution of calcareous nannofossils, Holes U1519C and U1519E. **Download table in CSV format.**

Table T6. Distribution of foraminifers and other fossil material, Holes U1519C–U1519E. **Download table in CSV format.**

Table T7. Summary of biostratigraphic and foraminifer data, Holes U1519C and U1519E. **Download table in CSV format.**

Planktonic foraminifers

Planktonic foraminifer biostratigraphy at Site U1519 was based on the examination of core catcher samples from Holes U1519C–U1519E. Absolute ages assigned to biostratigraphic datums follow those listed in Table **T4** in the Expedition 372B/375 methods chapter (Wallace et al., 2019). Biostratigraphic datums are given in Table **T4**, and the distribution of planktonic foraminifer taxa is given in Table **T6**. Planktonic foraminifer abundances, indications of oceanicity (qualitative measure of the extent to which the paleoenvironment recorded by the faunal assemblage represents open ocean conditions relative to a nearshore-influenced environment), paleowater depths, and downslope reworking are given in Table **T7** and Figure **F10**.

Because of the high sedimentation rate and the relatively fine grained nature of the cored sedimentary sequence, microfossil residues (>125 µm) from washed samples are often small, even from 10 cm whole-round (352 cm^3) samples. Foraminifers (mostly planktonic) dominate the small residues, however, and age markers are present in sufficient numbers to date most samples reliably. Plant-derived matter and other fossil material including shell (bivalve, gastropod, scaphopod, and barnacle) fragments, echinoid spines and plate fragments, radiolarians, ostracods, and otoliths are also present in variable amounts in most samples. In addition, rare fish teeth, sponge spicules, charophytes, and reworked Pliocene–Miocene taxa are present in some samples.

Holocene

Assemblages from the Holocene section in Hole U1519E are generally well preserved and include rare reworked Pliocene taxa that are moderately to poorly preserved. The presence of *Hirsutella hirsuta* in mudline Sample 375-U1519E-1H-1, 0 cm (0.0 mbsf), and Sample 1H-CC, 8–18 cm (4.40 mbsf), indicates that the uppermost part of the cored succession is Holocene (younger than 0.011 Ma). The absence of *Hr. hirsuta* in underlying samples indicates the base of the Holocene lies between Samples 1H-CC, 8–18 cm, and 2H-CC, 14–24 cm (4.40–14.00 mbsf).

Pleistocene

Pleistocene planktonic foraminifer abundances in Hole U1519E and the upper two cored sections of Hole U1519C (Samples 375-U1519E-2H-CC, 14–24 cm, through 375-U1519C-12R-CC, 6–16 cm [14.00–284.70 mbsf]) are highly variable and fluctuate between outer neritic and oceanic values (Figure **F10**). Assemblages are generally well preserved, but rare reworking in the form of moderately to poorly preserved Pliocene and Miocene taxa occurs in some samples. *Truncorotalia truncatulinoides* is common throughout this interval, and populations are predominantly sinistral coiled, indicating a Late to Middle Pleistocene age (Haweran to Castlecliffian; 0.011–0.53 Ma). Cores were not taken from the drilled interval (375-U1519C-131 [288.4–518.4 mbsf]).

The lower part of the cored Pleistocene section (Samples 375-U1519C-14R-CC, 0–15 cm, through 26R-CC, 0–5 cm [522.39–635.60 mbsf]) includes planktonic foraminifer assemblages with dextrally coiled populations of *Tr. truncatulinoides*, indicating a Middle to early Pleistocene (Castlecliffian to Nukumaruan) age of 0.53–2.17 Ma. The first common occurrence of *Tr. truncatulinoides* (0.62 Ma) occurs in Sample 15R-CC, 10–19 cm (536.32 mbsf), and indicates that the uppermost part of the lower cored section is Middle Pleistocene (Castlecliffian; 0.53–0.62 Ma). The age to the bottom of Hole U1519C where *Tr. truncatulinoides* is much less common is Middle to early Pleistocene (Castlecliffian to Nukumaruan; 0.62–2.17 Ma).

Benthic foraminifers

Benthic foraminifer abundances in Holes U1519C and U1519E are generally much lower than planktonic abundances and range from 8% to 79%. Midbathyal markers, including *Eggerella bradyi* and *Sigmoilopsis schlumbergeri*, occur sporadically through the cored sedimentary sequence, indicating paleowater depths of at least 600 m. Lower bathyal markers including *Planulina wuellerstorfi* and *Cibicides robertsonianus* are also present in the mudline sample and in the lower part of the cored section (Samples 375-U1519C-16R-CC, 0–11 cm, through 26R-CC, 0–5 cm [546.86–635.60 mbsf]), indicating paleowater depths of 1000 m or deeper. Inner shelf taxa including *Zeaflorilus parri, Nonionella flemingi, Elphidium charlottensis, Haynesina depressula, Notorotalia* spp., and miliolids are relatively common, especially in samples with higher benthic abundances. The presence of these taxa in association with bathyal and midbathyal benthic markers suggests they have been transported downslope.

Figure F10. Summary of lithostratigraphy, planktonic foraminifer abundance, interpreted oceanicity, paleowater depths, and biostratigraphic datums, Site U1519. NZ = New Zealand.

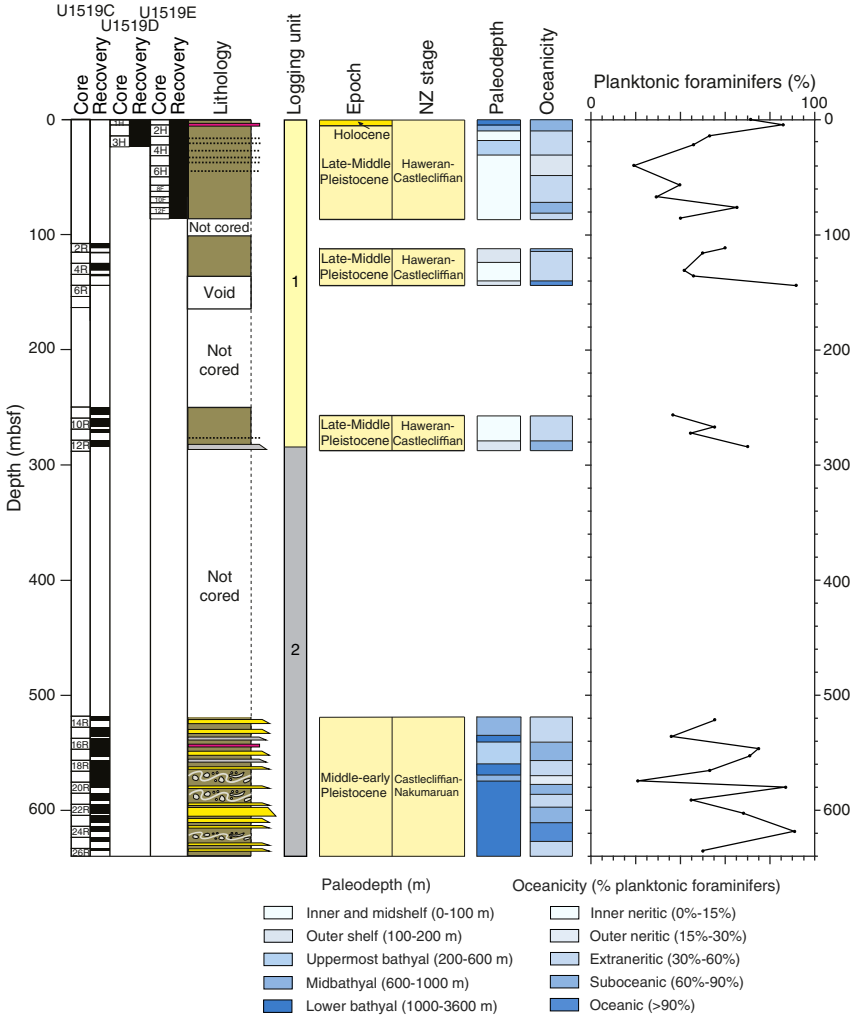

Paleomagnetism

Paleomagnetic analyses at Site U1519 included natural remanent magnetization (NRM) measurement of archive-half core sections prior to and following stepwise alternating field (AF) demagnetization. Five discrete samples from Hole U1519C and eleven samples from Holes U1519D and U1519E were subjected to exploratory anisotropy of magnetic susceptibility measurements, more detailed AF demagnetization, and isothermal remanent magnetization acquisition experiments.

Drilling disturbance, including ductile deformation, mixing, severe biscuiting, and bed drag along the core liners, often resulted in depositional remanence destruction that compromised the paleomagnetic analyses and limited the reliability of the data sets. As a result, we did not conduct any paleomagnetic analyses on spot cores recovered from 108 to 136 mbsf (Cores 375-U1519C-2R through 5R) and from 250 to 285 mbsf (Cores 9R–12R). We analyzed the largely intact core material recovered from the more consolidated interval from 525 to 635 mbsf (Cores 14R–26R). As usual for RCB cores, sections in this interval were often dissected into numerous 5–50 cm long subhorizontal biscuits (see **Lithostratigraphy** and **Structural geology**).

The material recovered from Holes U1519D and U1519E was also affected by drilling disturbance, and most sections have vertical flow-in features and/or bed drag along the rims of the core liners. We avoided the measurement of section halves in which any sedimentary features were severely damaged or absent, but for rock magnetic purposes we measured sections that were affected by bed drag and small-scale flow-in.

Hole U1519C

Archive halves from Cores 375-U1519C-14R through 26R were subjected to AF demagnetization in 5 or 10 mT increments up to 40 mT and measured following each treatment step. NRM intensity values prior to demagnetization range from ~5×10^{-3} to 0.01 A/m (Figure **F11**) with little variation downhole, which is consistent with the magnetic susceptibility records. Visual inspection of individual measurements in vector component diagrams shows that magnetic remanences are usually pervasively overprinted, with measurements on only a few sections showing straight-line decay to the origin at demagnetization levels ≥20 mT (Figure **F12**). Many measurements yield a minor component with a characteristic remanent magnetization direction that extends through the origin in the coercivity range of 20–30 mT. Upon demagnetization to higher lev-

Figure F11. Magnetic inclination, declination, and intensity and magnetic susceptibility (MS), Hole U1519C (>520 mbsf). See text for details. GAD = geocentric axial dipole.

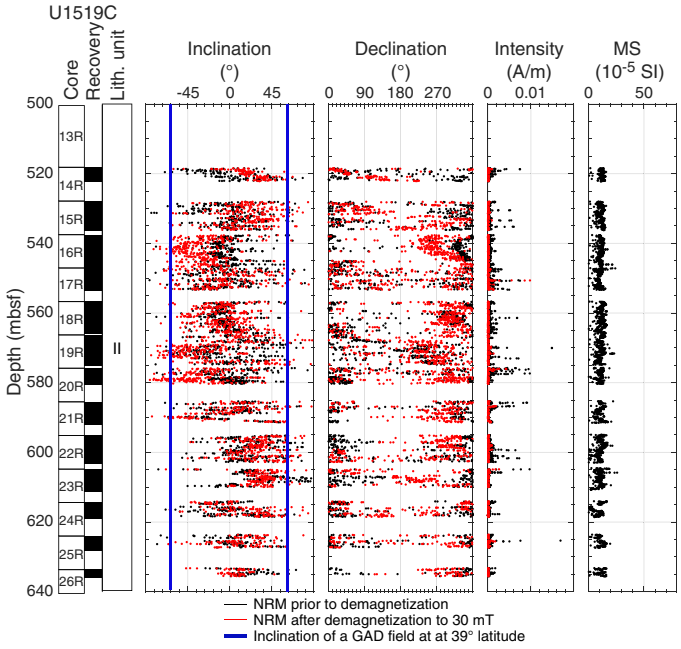

els, however, the demagnetization trajectory often trends away from the origin. Declination records from differing cores or across biscuit boundaries are usually offset with respect to each other, indicating that drilling-induced overprints do not have a major effect on the data set. From 528.0 to 590.8 mbsf (Core 15R through Section 21R-5), NRM inclinations measured following demagnetization to 30 mT are mostly negative. In contrast, from 590.8 to 635.65 mbsf (Section 21R-6 through Core 26R) we primarily measured shallow downward dipping (positive inclination) remanence directions. The sedimentary package in this interval was likely affected by significant tectonic deformation and bedding tilt. It comprises sequences of MTDs interbedded with coarse sand and silt layers (see **Lithostratigraphy**), and detrital remanences may have been further overprinted or damaged during the diagenetic alteration of the magnetic remanence carriers following deposition and burial, which makes the data set unsuitable for a shipboard magnetostratigraphic interpretation.

Holes U1519D and U1519E

Figure **F13** displays the paleomagnetic inclination, declination, and intensity records of the NRM measured on Hole U1519E archive halves prior to and following AF demagnetization to a peak field of 20 mT, as well as the section-half magnetic susceptibility measured using the Section Half Multisensor Logger (SHMSL) (see **Physical properties**). Figure **F14** compares the paleomagnetic records following partial demagnetization and susceptibility values recorded on sediments from Hole U1519D and the upper 22.5 m of Hole U1519E. NRM remanence intensity values range from ~4 × 10^{-4} to 0.02 A/m, whereas peak values coincide with tephra bearing units. Visual inspection of measurements in vector component diagrams shows that viscous overprints are largely removed at the 15 or 20 mT demagnetization step, where remanences decay univectorially toward the origin. The majority of cores were therefore demagnetized to a peak field of 20 mT only, whereas a smaller subset

Figure F12. Representative vector components (Zijderveld) and NRM intensity vs. demagnetization level from superconducting rock magnetometer measurements on archive halves, Hole U1519C.

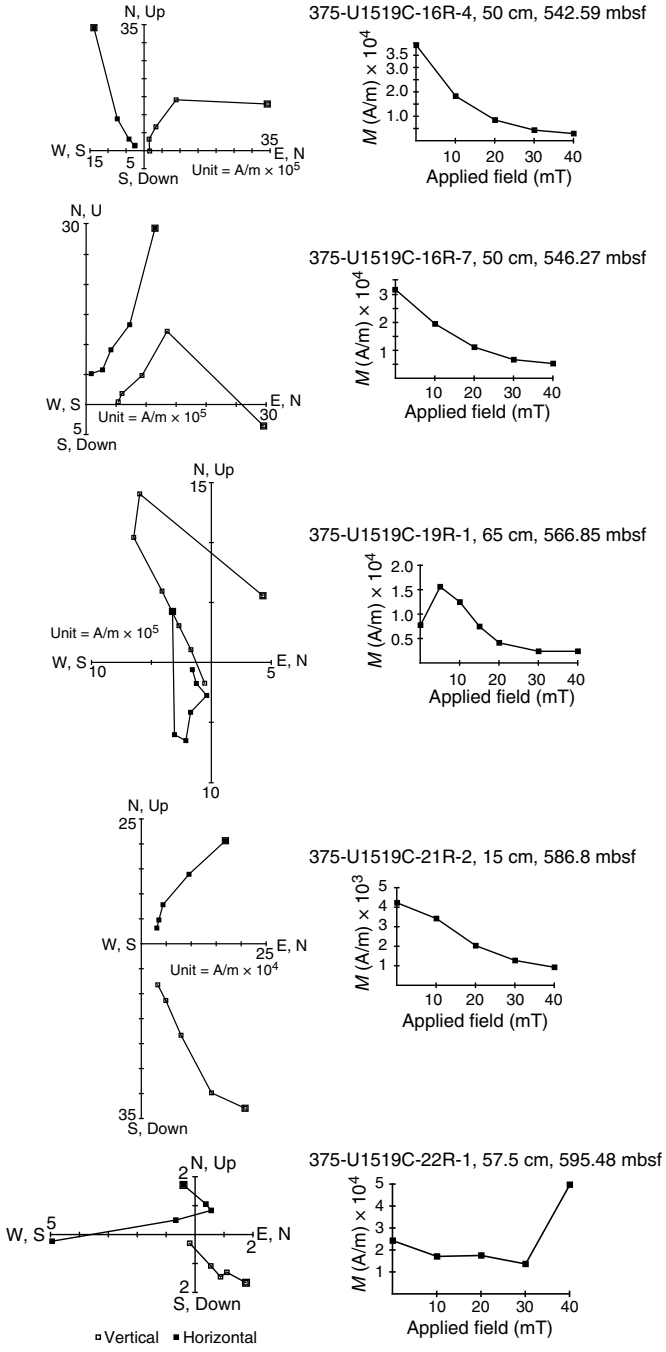

of archive halves were further demagnetized up to 30 or 40 mT to validate these results. Measurement sequences extended to the 40 mT demagnetization level showed that the material recovered throughout Holes U1519D and U1519E yields median destructive fields of 30 mT or more, and in many cases sediments in the archive halves retained as much as 70% of their initial remanence upon demagnetization to 40 mT. The NRM directions prior to and following partial demagnetization yield declinations that are offset from core to core, which suggests that drilling-induced overprints are absent. The NRM directions usually have negative inclinations, and many

Figure F13. Magnetic inclination, declination, and intensity and magnetic susceptibility, Hole U1519E. See text for details.

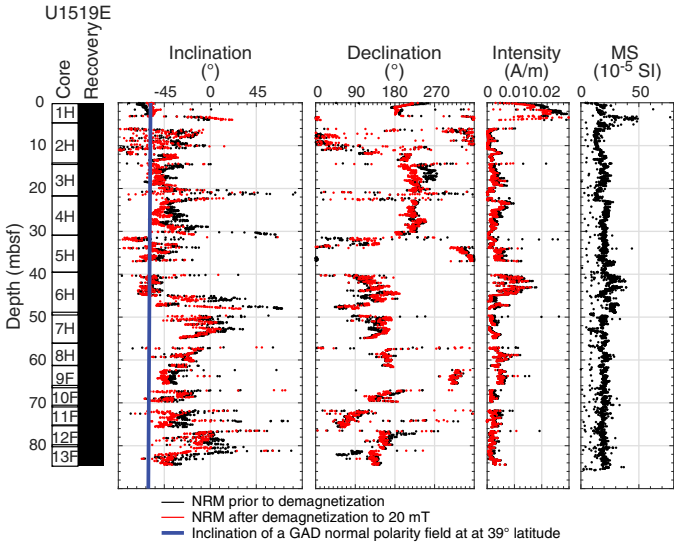

Figure F14. Magnetic inclination, declination, and intensity and magnetic susceptibility, Holes U1519D and U1519E.

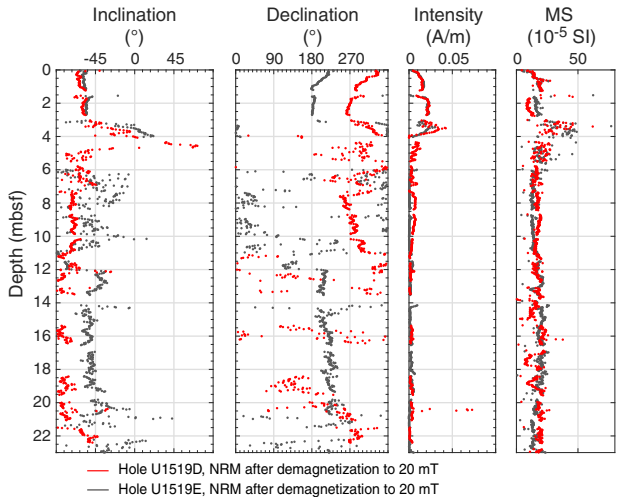

sections carry remanences that fall well into the directions expected in a normal polarity field. Swings in inclination observed downhole, however, may be a feature of core disturbance and do not necessarily reflect variations in the inclination of the ambient field at the time of deposition.

Structural geology

At Site U1519, cores were recovered from four zones separated by depth intervals that were drilled without coring. The top zone (Cores 375-U1519D-1H through 3H and 375-U1519E-1H through 13F) was cored with the APC system, whereas the three lower intervals (Hole U1519C) were cored with the RCB system. Because of partial core recovery, we rely on dip data from geoVISION (GVR) resistivity image logs obtained from LWD during Expedition 372 for the intervals with no core recovery or extensive drilling disturbance.

The strata at Site U1519 are inclined and have bed dips that rarely exceed 60° (Figure **F15**). Exceptions where steeper bedding dips are recorded are in folded strata interpreted to be MTDs. Small displacement fractures and minor faults are present locally. The dip and depth distributions of structures recorded in the core and GVR image logs are plotted in Figures **F15** and **F16**. Many of the structures and dipping beds observed in the core were oriented to a geographical reference frame using paleomagnetic data (see **Paleomagnetism**), and these preliminary orientations are plotted in Figures **F15** and **F17**. Typical uncertainty for the reoriented azimuths is ~030° (see **Structural geology** in the Expedition 372B/375 methods chapter [Wallace et al., 2019]).

We define two structural domains based on changes in structures observed in the core and GVR image logs. Domain 1 is characterized by intervals of moderate bedding dips alternating with intervals where dips are steeper and more variable (Figures **F15**, **F16**). Domain 2 is defined by a marked decrease in the number of filled fractures and gentle to moderate bedding dips to the northwest. Scattered, steeply dipping, dominantly conductive fractures are identified in GVR image logs throughout both domains (Figure **F16**).

Types of structures observed in the core

The main structure types observed at Site U1519 are fractures and rare small faults. Features designated as "fractures" include all opening-mode discontinuities that show little to no evidence of apparent shear displacement. At this site, these fractures are predominantly open fractures, although sets of variably oriented, filled fractures are present below 534.5 mbsf (Section 375-U1519C-15R-6) (Figure **F15**). Soft-sediment deformation is evident in MTDs in some intervals (see **Lithostratigraphy**), including folded and locally overturned beds and some zones of sheared sediments (Figure **F18**).

Domain 1

Domain 1 is defined from the tops of Cores 375-U1519D-1H and 375-U1519E-1H through Section 375-U1519C-19R-1 (0–567.58 mbsf) and is characterized by scattered steep fractures and dominantly, moderately northeast-dipping beds interrupted by intervals of variable but markedly steeper dipping beds with a range of dip azimuths. Four separate intervals were cored in this domain: the uppermost interval used the APC system, and the three lower intervals used the RCB system. Severe drilling disturbance occurred in the shallower three intervals, making structural observations difficult. Structural Domain 1 spans Lithostratigraphic Units I and II and Logging Units 1 and 2 (Figures **F15**, **F16**) (see **Lithostratigraphy** and **Logging while drilling**). Below, we describe observations from the cored intervals in the context of the structural features revealed by the GVR image logs (Figure **F16**).

APC and HLAPC cores from the top of Domain 1 (Cores 375-U1519D-1H through 3H [0.0–23.13 mbsf] and 375-U1519E-1H through 13F [0.0–86.21 mbsf]) were disturbed by upward-warping of beds to variable degrees, but some geological features were preserved (Figure **F15**). Bedding in the core is gently to moderately dipping (15°–60°) (Figure **F18A**). Bedding dips from the GVR image log range from 10° to vertical, which is slightly steeper than bedding dips measured in the core (Figure **F15**). The steeper beds in the GVR data are common to 80 mbsf, and dips as steep as 60° persist to 143 mbsf at the base of Logging Subunit 1B (Figure **F16**). These steep dips likely result from MTDs dominating this interval, which are also visible in seismic reflection data (see **Core-log-seismic integration**). The Logging Subunit 1B/1C boundary lies in Domain 1 and is marked by a transition to more gently dipping beds (<50°). Although this transition was sampled in the first RCB cored interval

Figure F15. Structure dips and azimuths measured in Hole U1519C–U1519E cores and from Hole U1519A GVR image log data. Pale yellow = Structural Domain 1, light blue = Domain 2. Lithostratigraphic and logging units shown for comparison.

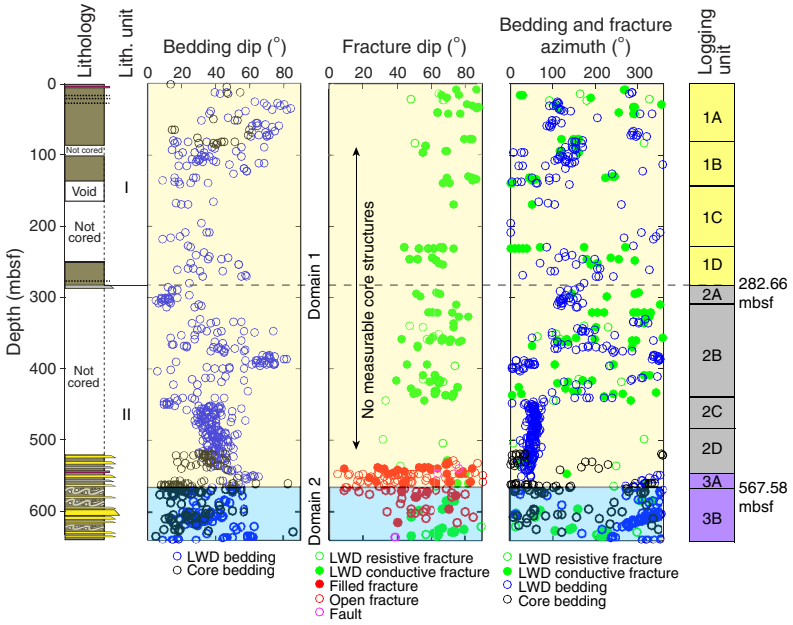

(Cores 375-U1519C-2R through 7R [108.0–163.6 mbsf]), cores were severely biscuited (<5 cm thick biscuits), and we were unable to resolve bedding or other structures. Furthermore, Core 7R, which would have sampled the top of Logging Subunit 1C, had no recovery.

Core 375-U1519C-6R through drilled interval 131 (144.3–518.4 mbsf) represent intervals with no recovery (including two intervals drilled without coring [375-U1519C-81 and 131]) or severe drilling disturbance, including the second RCB cored interval (Cores 9R–12R [250.0–288.4 mbsf]), where no structures were identified. The GVR image log in this depth interval provides information about structural trends. Bedding dips range from <10° to nearly 80°, although steep dips (>60°) are rare (Figures **F15**, **F16**). From 450 to 550 mbsf, bedding dips lie in a consistent range from 30° to 50° and dips are to the northeast (Figure **F15**). A lithostratigraphic boundary is defined at 282.66 mbsf in these cores (see **Lithostratigraphy**), but no distinct change in structural style occurs at this boundary in either the core or GVR image data (Figures **F15**, **F16**).

The third RCB interval (Cores 375-U1519C-14R through 26R [518.4–635.6 mbsf]) yielded good quality cores. From 518.4 to 567.6 mbsf (base of Section 19R-1), beds generally dip <50° to the north-northeast (Figures **F15**, **F17**, **F18B**) and localized intervals of abundant filled fractures occur. Bedding dips from GVR data over much of this interval range from 40° to 60° to the east-northeast, which is a smaller range of dips than measured in the core (Figure **F15**). However, steep beds in the core are commonly associated with soft-sediment deformation features (Figure **F18C, F18D**). Below 550 mbsf, the dominant dip direction in GVR data shifts to the west-northwest and dip angles are more variable (10°–60°). The change in dip direction at ~550 mbsf corresponds to the Logging Unit 2/3 boundary (Figure **F16**; also see **Core-log-seismic integration**).

Scattered open and filled fractures are present throughout Cores 375-U1519C-14R through 26R (518.4–635.65 mbsf), but their abundance decreases markedly below Section 19R-1 (from 567.58 mbsf) (Figure **F15**). Filled fractures are more abundant in some sections (e.g., 16R-2 and 18R-2) and are present at a range of dip angles from subhorizontal to near vertical (Figures **F15**, **F19A, F19B**). A few steep, filled fractures form the edge of fracture meshes that comprise intersecting smaller fractures (Figure **F19B**). A few steep (>60°), indeterminate faults are present in the lower section of Domain 1. These faults truncate beds that cannot be traced across the fault (e.g., interval 16R-6, 95–108 cm; Figure **F19C**).

Open fractures range from subhorizontal to vertical with a large variation of dip directions (Figures **F15**, **F17**, **F19**). The open fractures commonly appear in spaced sets (e.g., Figure **F19B**) and are locally en echelon. It is difficult to determine whether these fractures were present prior to drilling. In some places they occur along filled fractures, in other places they are parallel to bedding or filled fractures, and in some they crosscut all other planar structures. It is possible that many of these fractures were original structures or interfaces, such as bedding, that were activated during drilling.

Domain 2

Domain 2 is defined from 567.58 mbsf to the base of the hole at 635.6 mbsf (Section 375-U1519C-19R-2 through Core 26R) and is characterized by gentle to moderate bedding dips toward the northwest, soft-sediment deformation, and scattered fractures. The Domain 1/2 boundary is defined by a decrease in the abundance of filled fractures in the core and also marked by the top of an obvious zone of MTDs and a gradual change in bedding azimuth (Figure **F15**). In the GVR image log, bedding dip direction changes gradually between Logging Units 2 and 3, the boundary of which is located slightly shallower than the Domain 1/2 boundary. In the core, bedding dips become generally gentler than 30° from the top of Domain 2 downhole (Figure **F15**). Oriented bedding dip azimuths in Domain 2 are variable but dominantly northwest and southeast with fewer to the northeast (Figure **F17**). In the GVR image log, most identified beds dip to the northwest (Figure **F15**). Open fractures in this zone are sparser and generally steeper than in Domain 1 but remain common in some intervals.

Borehole breakouts are observed in Domain 2 in a cluster around ~600 mbsf and from 620 to 650 mbsf (Figure **F16**). Borehole

Figure F16. GVR image log and interpreted bedding, fracture, and borehole breakout orientations (see Logging while drilling), Hole U1519A. Tails on fracture and bedding symbols indicate dip azimuth. Long axes of oval borehole breakout symbols indicate azimuthal orientation of borehole breakouts (north [000°] is up); position of breakout symbols on *x*-axis is arbitrary. RAB = resistivity-at-the-bit.

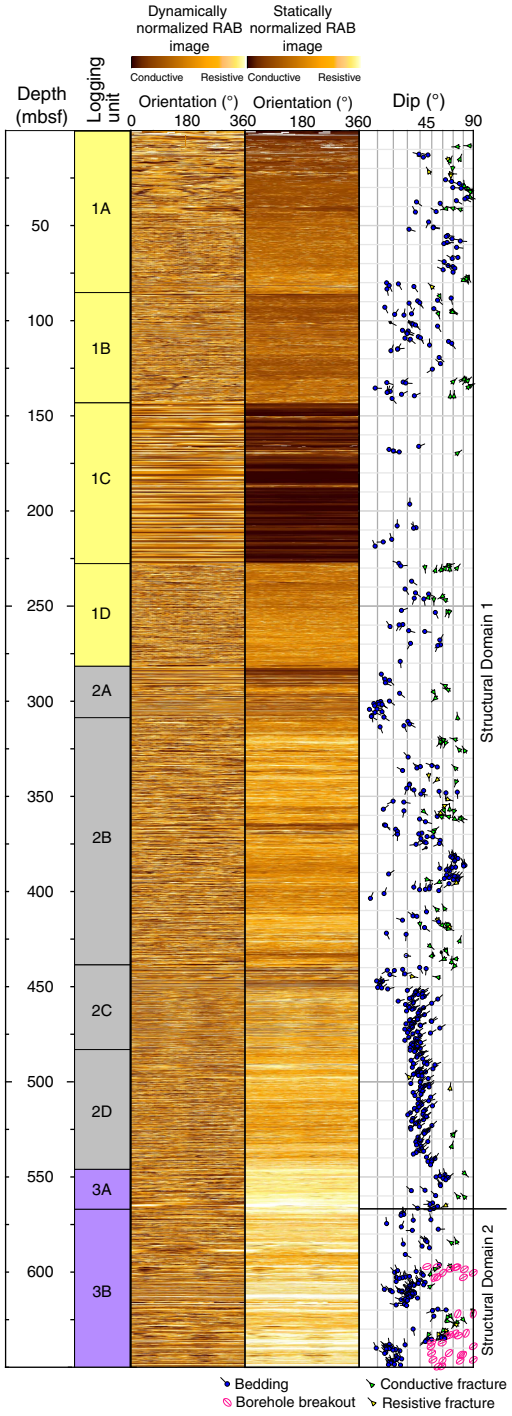

breakout orientations are approximately 054°/234°, implying a minimum horizontal stress (S_{hmin}) orientation of northeast–southwest, from which a maximum horizontal stress (S_{Hmax}) orientation of northwest–southeast can be inferred. Borehole breakout widths range from 33.9° to 83.6°.

Figure F17. Lower hemisphere, equal-area stereoplots showing orientations of bedding and filled and open fractures (great circles), Hole U1519C. The structures shown were oriented to geographical reference frame based on paleomagnetic measurements. Uncertainty in azimuth is as high as 30°. Top: orientations in Domain 1 (14R through 19R-1). Bottom: structures in Domain 2 (19R-2 through 26R).

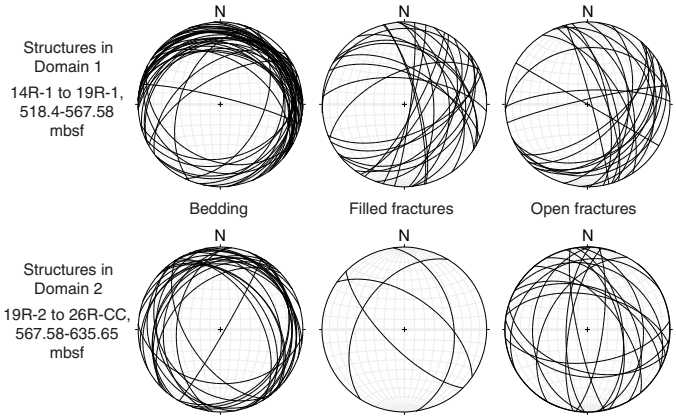

Figure F18. Examples of bedding and related structures recovered from Structural Domain 1. A. Dipping strata in upper part of Domain 1 (375-U1519E-13F-1, 64–84 cm). B. Dipping strata near base of Domain 1 (375-U1519C-15R-6, 2–22 cm). C. Unconformable bedding contact (375-U1519C-18R-1, 21–41 cm). D. Overturned bedding terminating along a planar zone of sheared sediment (375-U1519C-18R-4, 11–31 cm).

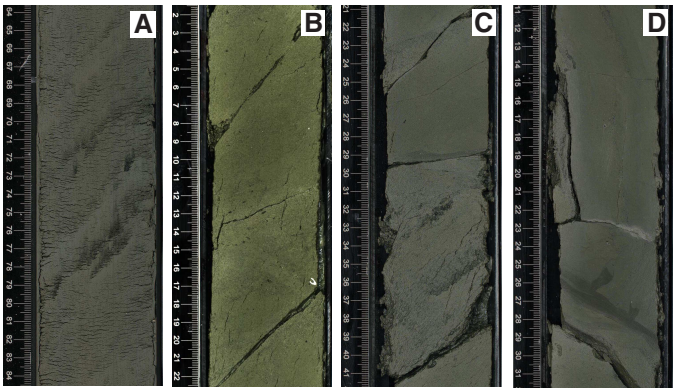

Drilling disturbance

Drilling disturbance in the cores was extensive throughout most of Holes U1519C–U1519E and included biscuiting (RCB cores) and sediment flow (both APC and RCB cores). In Hole U1519D, cores typically have upward-arching beds, and in some cores this upward arching was severe enough that original bedding was subparallel to the core axis. The shallow RCB cores (375-U1519C-2R through 7R and 9R–12R) were severely biscuited, and sediments in the biscuits showed intense ductile flow (e.g., tight folds with variable orientations). No structures could be recognized in these cores. The deeper RCB cores (14R–26R) have mild to moderate biscuiting and were also disturbed by fractures that may be caused or enhanced by drilling. Rare sandy intervals were generally affected by mingling, appeared soupy, and did not preserve any internal structure. However, except for these scattered coarse intervals, structures were generally recognizable and measurable in cores recovered from below 518.4 mbsf.

Figure F19. Representative fractures and faults in Structural Domain 1, Hole U1519C. A. Steep, composite, filled fracture showing branching and gentler dipping fractures connecting en echelon steep fractures (16R-2, 18–25 cm). Note open fracture cutting the filled fracture. B. Two subparallel, steeply dipping filled fractures bound a zone of intense fracturing (16R-1, 31–44 cm). A more gently dipping filled fracture bends near the steeper pair of fractures. Note also parallel, spaced, open fractures above and below the filled fractures. C. Steeply dipping indeterminate fault branching near base of photograph (16R-7, 96–105 cm). A bed terminates against the fault to the right but is not identified on left side of fault; this bed is also truncated by a steep, open fracture subparallel to the branching fault.

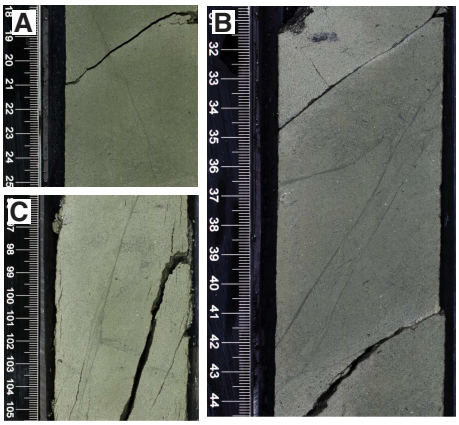

Summary

Deformation features at Site U1519 include small-scale localized fractures and variably inclined bedding. The description of Domain 1 is based on core description, GVR image log data, and seismic reflection images that indicate a large range of bedding dips attributed to stacked MTDs at the top of Expedition 372 Hole U1519A, transitioning downward to moderately dipping beds (Figures **F15**, **F16**) (see **Core-log-seismic integration**). Filled fractures are common in some cored intervals near the base of Domain 1. Domain 2 is defined by a reduced frequency of filled fractures, a change in bedding dip azimuth from northeast to northwest, and generally gentle bedding dips, except where steep and locally overturned beds are present in MTDs inferred from both core observation and LWD data. Borehole breakouts observed between 600 and 650 mbsf have an approximate northeast–southwest (054°/234°) S_{hmin} orientation.

Geochemistry

Inorganic geochemistry

The main objective of the inorganic geochemistry program at Site U1519 was to identify potential fluid flow and fluid–rock interactions that may affect the physical, hydrological, and mechanical properties of the sediment hosting the borehole observatory installed in Hole U1519B. A total of 75 routine pore water whole-round (WR) samples (10–30 cm long) were collected and squeezed for shipboard and shore-based pore water chemical analyses. We collected 30 samples from RCB cores in Hole U1519C, 15 samples from APC cores in Hole U1519D, and 30 samples from APC cores in Hole U1519E. WR samples were collected on the catwalk at a frequency of six samples per core in the upper ~20 m and ~1–4 samples per core deeper than 20 mbsf. Each core in Hole U1519C deeper than 250 mbsf was scanned with an IR camera to identify the occurrence of methane hydrate, indicated by cold temperature anomalies resulting from methane hydrate dissociation during core recovery.

Table T8. Pore water uncorrected major element concentrations, Site U1519. **Download table in CSV format.**

Table T9. Pore water uncorrected minor element concentrations, Site U1519. **Download table in CSV format.**

Table T10. Pore water major element concentrations analyzed via ion chromatography from samples processed in a glove bag, Site U1519. **Download table in CSV format.**

Figure F20. Sulfate, alkalinity, and chloride concentration profiles, Holes U1519D and U1519E (0–30 mbsf). Arrows = average seawater values.

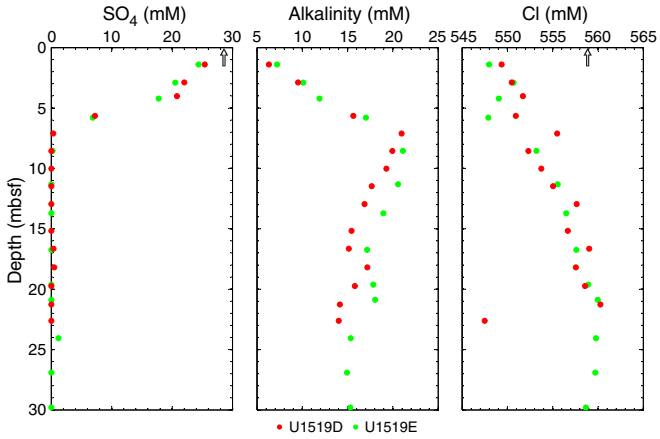

All WR samples were thoroughly cleaned in an effort to remove drilling fluid contamination, placed in titanium squeezers, and squeezed at gauge forces to a maximum of 30,000 lb. The volume of recovered pore water varied with lithology, depth, and coring technique and ranged between 11 and 56 mL in APC cores, 34 and 45 mL in HLAPC cores, and 12 and 42 mL in RCB cores. The pore water data were not corrected for drilling water contamination at this site because sulfate concentrations below the sulfate–methane transition zone (SMTZ) were uniformly low (mostly below 0.4 mM), indicating less than 2% drilling fluid contamination, with the exception of one WR from a silty interval (Sample 375-U1519C-25R-4, 67–95 cm) collected to assess gas hydrate concentration. An additional 43 WR samples were collected adjacent to the routine pore water WRs in APC Holes U1519D and U1519E. These WRs were immediately processed in a glove bag flushed with ultrahigh-purity nitrogen for shipboard and shore-based analyses of redox-sensitive elements.

Major and minor element concentrations are listed in Tables **T8** and **T9**. Major element concentrations analyzed via ion chromatography (IC) of samples that were processed in the nitrogen glove bag are listed in Table **T10**. Only the samples processed under atmospheric conditions are shown in Figures **F20**, **F21**, **F22**, and **F23**.

The geochemical profiles at Site U1519 reflect the combined effects of organic matter diagenesis, authigenic carbonate precipitation, and silicate mineral/volcanic ash alteration under high sedimentation rates. Below, we provide a general description of the pore water chemical profiles and the evidence for diagenetic reactions.

Figure F21. Sulfate, alkalinity, ammonium, bromide, and phosphate concentration profiles, Holes U1519C–U1519E. Arrows = average seawater values.

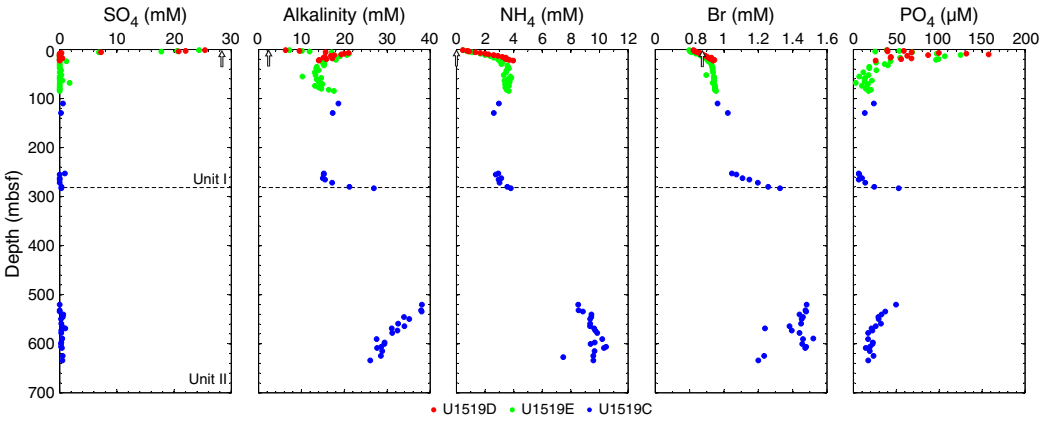

Figure F22. Chloride, sodium, potassium, calcium, magnesium, and silica concentration profiles, Holes U1519C–U1519E. Arrows = average seawater values. Note that major cations were measured by IC and inductively coupled plasma–atomic emission spectrometry (ICP-AES), but only IC data for potassium and sodium and ICP-AES data for calcium and magnesium are plotted because these data have higher precision.

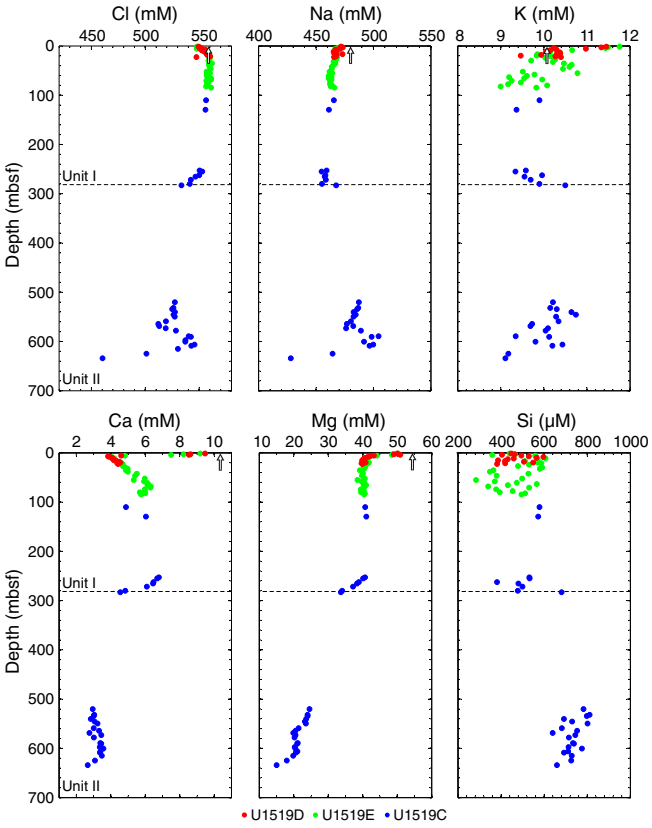

Figure F23. Strontium, lithium, boron, manganese, barium, and iron concentration profiles, Holes U1519C–U1519E. Arrows = average seawater values.

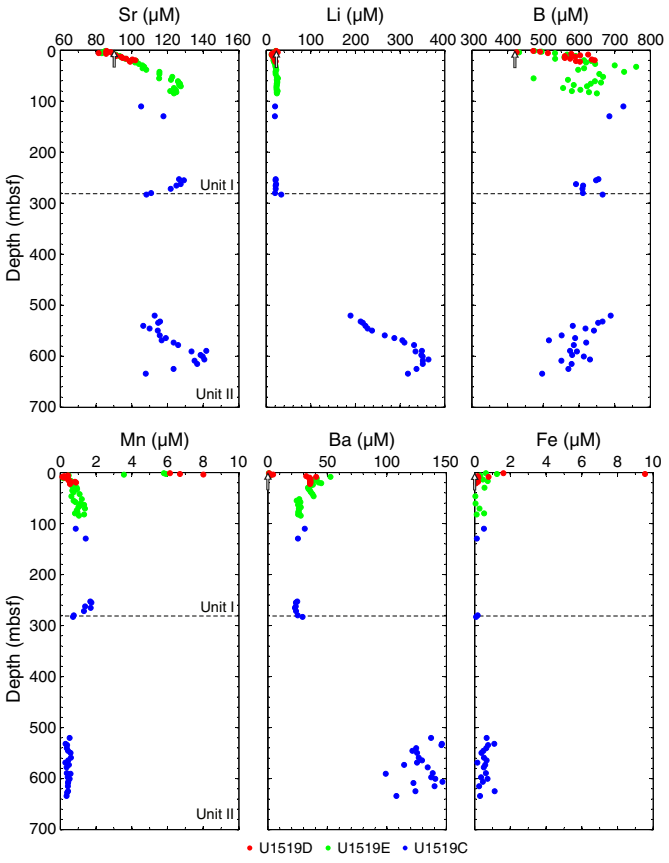

Organic matter diagenesis

The pore water profiles of sulfate, alkalinity, ammonium, bromide, and phosphate in Lithostratigraphic Unit I show characteristic changes with depth related to organic matter degradation. The profiles in the upper ~8 m, however, do not reflect steady-state sedimentation. Under steady-state conditions, sulfate concentrations typically decrease linearly from seawater value at the seafloor to depletion at the SMTZ. The pore water sulfate profiles in Holes U1519D and U1519E are kinked, with an abrupt change in depth trend at ~4 mbsf indicating a recent period of rapid sedimentation in the upper few meters (Figure **F20**) that produces a deeper SMTZ than would be observed under steady-state sedimentation, which is also indicated by the kinked alkalinity profile between the seafloor and the SMTZ. As a result, the SMTZ at Site U1519 is at ~7–8 mbsf, similar to that observed at the frontal accretionary wedge Site U1518 but shallower than nearby Site U1517 (Barnes et al., 2019).

Below the SMTZ in Unit I, alkalinity concentrations decrease to ~14 mM at 90 mbsf. Phosphate concentrations mimic the alkalinity profile, with a peak of 157 µM at 10 mbsf (Figure **F21**). Ammonium

concentrations also increase with depth to a maximum of ~3.8 mM at 15 mbsf and then decrease slightly in samples from Sections 375-U1519C-2R-2 through 2R-4. The trend of the bromide concentration profile mimics that of ammonium (Figure **F21**).

Typically, an increase in ammonium and alkalinity concentrations occurs down to the SMTZ and a decrease in alkalinity and phosphate concentrations occurs below the SMTZ, reflecting the competition between metabolite production through ongoing microbial methanogenesis and consumption in authigenic minerals. Deeper in the sediment column (typically >50 mbsf), alkalinity and ammonium concentrations reach asymptotic values and phosphate concentrations remain below detection. At Site U1519, however, a sharp increase in ammonium, alkalinity, phosphate, and bromide concentrations occurs across the Unit I/II boundary, with a second concentration maxima in Unit II. The depth of the second concentration maxima is unknown because of the coring gap between 285 and 520 mbsf. The concentrations of species related to organic matter diagenesis remain elevated in the cored interval from 520 to 635 mbsf, but their concentrations decrease with depth. We relate these second alkalinity, ammonium, phosphate, and bromide concentration maxima to rapid burial that preserves an older diagenetic sequence characterized by enhanced organic matter degradation and continued microbial methanogenesis, which is consistent with an average estimated sedimentation rate of 0.8 m/ky in Unit I (see **Biostratigraphy**).

Volcanic ash alteration and silicate mineral diagenesis

Dissolved calcium concentrations decrease sharply from 9.5 mM at 1.4 mbsf to 3.8 mM at the SMTZ, reflecting consumption in authigenic carbonate minerals driven by the alkalinity produced by sulfate reduction through both particulate organic carbon oxidation and anaerobic oxidation of methane (Figure **F22**). Below the SMTZ, calcium concentrations increase to 6.3 mM at 70 mbsf. The reversal in the Ca profile below the SMTZ suggests enhanced silicate mineral/volcanic ash alteration in the zone of microbial methanogenesis leading to a net addition of Ca to the pore water despite concurrent removal in authigenic carbonates (e.g., Solomon et al., 2014). Likewise, below the SMTZ, strontium concentrations increase to 130 µM (50% greater than seawater value), boron concentrations increase to ~750 µM (79% greater than seawater value), and potassium concentrations steadily decrease, consistent with silicate mineral/volcanic ash weathering in the upper 100 m of Unit I (Figures **F22**, **F23**). A second interval of enhanced silicate mineral/volcanic ash diagenesis occurs between 520 and 630 mbsf in Unit II. As observed in Unit I, strontium concentrations increase markedly to ~600 mbsf and potassium concentrations decrease; however, unlike the zone in Unit I, lithium concentrations increase sharply to values as high as 380 µM (~15× seawater value) at this depth, dissolved silica values are consistently elevated and range between 700 and 800 µM (silica in Unit I is between 400 and 600 µM), and boron concentrations have a decreasing trend. The different fluid compositions in the two zones of enhanced weathering likely reflect a difference in the composition of the reactive silicate phases and the secondary minerals produced through the weathering reactions.

Dissolved Ba concentrations increase abruptly below the SMTZ, likely in response to barite dissolution in response to sulfate depletion (Figure **F23**) (e.g., Torres et al., 1996; Dickens, 2001). Ba concentrations are also high between 520 and 630 mbsf in Unit II and range from 100 to 150 µM. The high Ba concentrations in this interval may simply reflect relict Ba addition from barite dissolution in the older diagenetic sequence buried in Unit II, but ongoing volcanic ash alteration and silicate mineral diagenesis may also be contributing additional Ba to the pore water.

Chloride and sodium concentration profiles

Chloride concentrations are lower than average modern seawater value (559 mM) in the upper portion of Unit I, increasing from 549 mM at 1.4 mbsf (2% lower than average seawater value) to 559 mM at 17 mbsf (Figure **F20**). Between 17 and 120 mbsf, Cl concentrations remain relatively constant at or near seawater value. Sodium concentrations are also 2% lower than average seawater value between the seafloor and 17 mbsf but remain low throughout Unit I (Figure **F22**). The cause of the lower Cl concentrations in the upper sediment section will be a focus of post-expedition research but could reflect (1) a recent change to a lower salinity water mass at this upper slope site or (2) constant low-salinity bottom water along the upper slope, in which case the increase in Cl concentrations in the upper 17 m is likely related to alteration and hydration of volcanic ash and silicate weathering reactions.

Chloride concentrations decrease from 550 to 534 mM across the Unit I/II boundary and are low, ranging from 440 to 546 mM, between 520 and 630 mbsf. Discrete anomalies in the Cl profile between 520 and 630 mbsf are the result of methane hydrate dissociation during core recovery, marking zones of elevated methane hydrate concentrations. However, Cl concentrations remain low throughout the 520–630 mbsf cored interval, and this low background chlorinity may reflect (1) disseminated methane hydrate throughout the section or (2) the presence of freshened fluids advected from a region where temperatures are high enough to support mineral dehydration reactions. Unfortunately, because of the coring gap above this cored interval, the background Cl profile is unconstrained, and determining the source of freshening at the base of Site U1519 (disseminated methane hydrate or advection) will require post-expedition isotopic studies.

IR scans on the catwalk were used to detect the occurrence of methane hydrate in each Hole U1519C core from deeper than 250 mbsf. Cold temperature anomalies were not frequently observed, partially because of poor core recovery in Cores 375-U1519C-2R through 7R. One methane hydrate–bearing WR was identified by IR scanning and collected to quantify methane hydrate saturation (Sample 25R-4, 67–95 cm) in the region of low chlorinity values in Unit II. This WR sample consisted of a gas hydrate–bearing silt layer. Because of the relatively high permeability of this silt, a considerable amount of drilling water contamination occurs, manifested by a sulfate concentration of 12.73 mM (~45% drilling fluid contamination). The measured chloride concentration for this sample is 440 mM. Considering the drilling fluid sulfate and chloride concentrations are 29 mM and 561 mM, respectively, the drilling water contamination–corrected Cl concentration for this sample is 333 mM. We do not provide an estimate of the methane hydrate saturation for this sample because it was collected below the coring gap; thus, a background Cl concentration profile is not clearly defined from which to estimate methane hydrate saturation.

Organic geochemistry

Gas analyses

Headspace samples were taken from each sediment core to monitor for the presence and abundance of C_1–C_3 hydrocarbons as part of the standard safety protocol (Pimmel and Claypool, 2001). Where possible, these samples were taken immediately adjacent to

Table T11. C_1–C_3 concentrations from headspace and void gas sample analyses, Site U1519. **Download table in CSV format.**

Figure F24. Methane (CH_4), ethane (C_2H_6), and ethene (C_2H_4) concentration profiles and calculated methane/ethane ratio, Holes U1519C–U1519E.

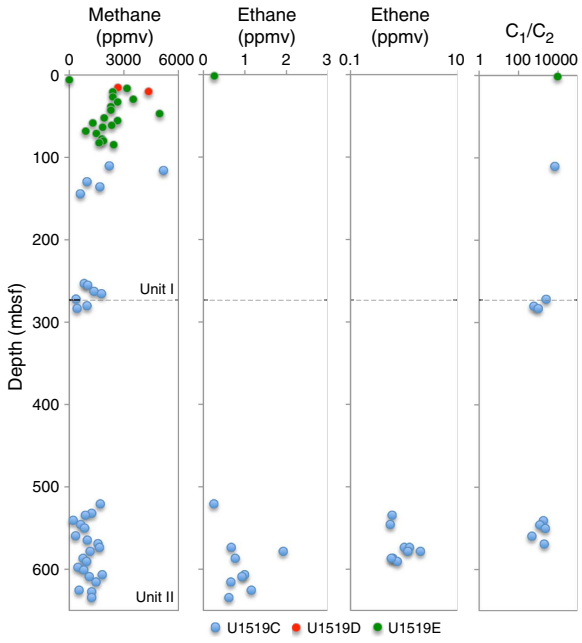

WR samples collected for pore water geochemistry. A total of 63 headspace and 2 void gas samples were analyzed by gas chromatography (see **Geochemistry** in the Expedition 372B/375 methods chapter [Wallace et al., 2019]). The results from Site U1519 are listed in Table **T11** and shown in Figure **F24**.

Between the seafloor and 144.3 mbsf, methane concentrations range from 0.55 to 5172 parts per million by volume (ppmv). Deeper than 144.3 mbsf, methane concentrations in the headspace samples are lower and remain between 212 and 1802 ppmv with an average concentration of 1011 ppmv. Ethane was detected in headspace samples deeper than 520.5 mbsf (ranging from 0.25 to 1.92 ppmv) but was not detected at shallower depths. The methane/ethane (C_1/C_2) ratios are consistently >500, suggesting a dominantly microbial source for the methane (Claypool and Kvenvolden 1983).

Bulk sediment analysis

A total of 101 samples were taken at Site U1519 (54 in Hole U1519C, 15 in Hole U1519D, and 32 in Hole U1519E) for elemental analysis by coulometric and carbon-hydrogen-nitrogen-sulfur (CHNS) measurements to determine inorganic carbon, calcium carbonate, total carbon (TC), total nitrogen (TN), and organic carbon concentrations (Table **T12**).

TC in Lithostratigraphic Units I and II increases slightly with depth and ranges from 1.05 to 3.27 wt% with an average of 1.48 wt% (Figure **F25**). Calcium carbonate concentrations range from 0.4 to 12.1 wt% in Unit I and from 6.1 to 21.9 wt% in Unit II (Figure **F25**). Organic C values in Units I and II range from 0 to 1.2 wt% with an average of 0.39 wt%. Inorganic C and TN concentrations increase slightly with depth in all lithostratigraphic units and range from 0.05 to 1.95 wt% (average = 1.1 wt%) and from 0.00 to 0.09 wt% (average = 0.05 wt%), respectively. Total organic carbon (TOC)/TN (C/N) ratios range from 0.85 to 14.9.

Table T12. TIC, $CaCO_3$, total C, TN, and TOC in bulk sediment samples, Site U1519. **Download table in CSV format.**

Figure F25. TC, $CaCO_3$, TOC, inorganic carbon, and TN concentration profiles and TOC to TN weight (C/N) ratio, Holes U1519C–U1519E.

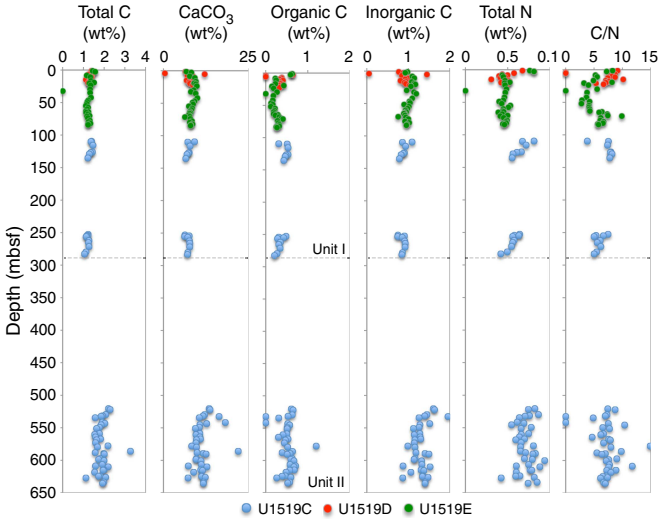

Physical properties

Density and porosity

Gamma ray attenuation (GRA) bulk density was determined on WR cores with the Whole-Round Multisensor Logger (WRMSL), and moisture and density (MAD) bulk density, grain density, and porosity were determined on discrete samples from Hole U1519C–U1519E working halves (see **Physical properties** in the Expedition 372B/375 methods chapter [Wallace et al., 2019]). Within 1 m of the seafloor, the GRA bulk density measured on cores from Holes U1519D and U1519E is ~1.5 g/cm^3. It increases rapidly to ~1.9 g/cm^3 at 7 mbsf and then gradually increases to ~2.0 g/cm^3 at 85 mbsf (Figure **F26**). GRA bulk density decreases slightly from the bottom of Hole U1519E to the first cored interval in Hole U1519C at 108–136 mbsf to values that generally range from 1.9 to 2.0 g/cm^3. From 250 to 284 mbsf, GRA bulk density is approximately 2.0–2.1 g/cm^3. Lower values, mostly between 1.8 and 2.0 g/cm^3, are observed in the lowermost cored interval in Hole U1519C (520–635 mbsf).

MAD bulk density values from Hole U1519D consistently overlap with data from Hole U1519E and are characterized by a large increase in MAD bulk density from 1.4 to 1.9–2.0 g/cm^3 in the uppermost 15 m. Between 15 mbsf and the bottom of Hole U1519E at 85 mbsf, bulk density increases gradually to 2.0–2.1 g/cm^3. MAD bulk density shifts to slightly lower values between the bottom of Hole U1519E at 85 mbsf and the first cored interval in Hole U1519C (109–135 mbsf), followed by an increase to values above 2.0 g/cm^3 from 250 to 284 mbsf. In the deepest cored interval in Hole U1519C (520–635 mbsf), MAD bulk density averages 2.0 g/cm^3 and exhibits a slight decreasing trend with depth.

MAD bulk density values provide an excellent match to both LWD density measurements and GRA density measurements from the WRMSL throughout the borehole, with the exception of the deepest cored interval in Hole U1519C, where the GRA bulk density values are lower than those from the MAD and LWD measurements, likely due to the small diameter of RCB cores at greater

Figure F26. Summary of physical properties, Site U1519. LWD data between 148 and 227 mbsf are low quality because of significant borehole washout. cps = counts per second.

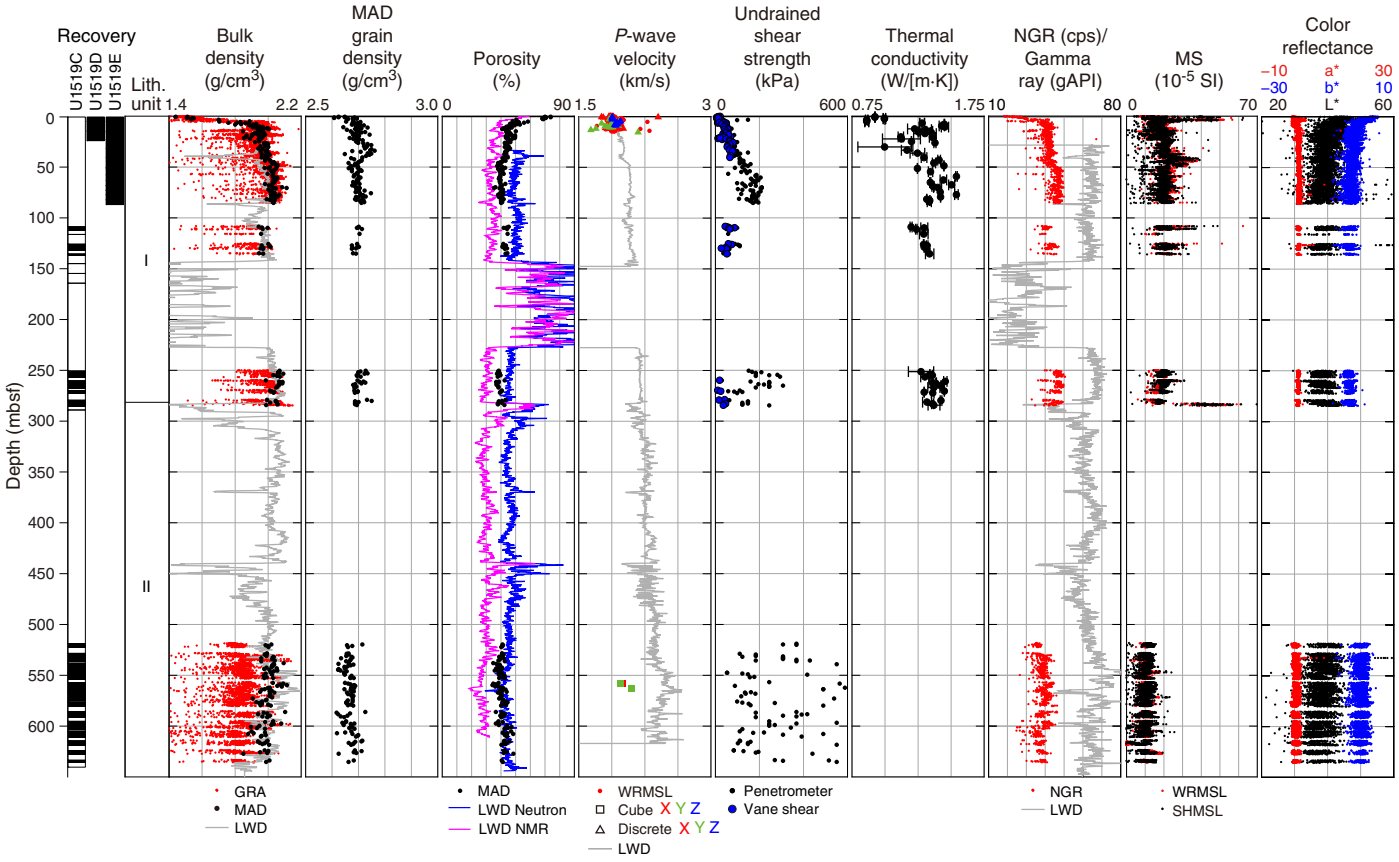

depths where sediments are more lithified. GRA bulk density corrected for the diameter of RCB cores based on image analysis (see **Physical properties** in the Expedition 372B/375 methods chapter [Wallace et al., 2019]) is consistent with MAD values for the entire depth (Figure **F27**).

MAD grain density values are nearly constant, ranging between 2.6 and 2.8 g/cm^3 (Figure **F26**). The lowest values are observed near the seafloor and increase slightly in the uppermost 10 m. An excursion to slightly higher MAD grain density values occurs at 30–40 mbsf, and another excursion to slightly lower values occurs deeper than 520 mbsf. The average grain density for the site is 2.7 g/cm^3.

Porosity values decrease rapidly from 74% at <1 mbsf to 41% at 12 mbsf in both Holes U1519D and U1519E. An excursion to slightly higher values (as high as 50%) occurs at ~20 mbsf, and then porosity decreases gradually to <40% at 50 mbsf and remains approximately constant (average = 40%) from 50 to 85 mbsf. Porosity shifts from 40% at the bottom of Hole U1519E to slightly higher values ranging from 41% to 45% from 109 to 135 mbsf in Hole U1519C. Porosity then decreases to an average value of 39% from 250 to 284 mbsf. In the deepest cored interval from 520 to 635 mbsf, porosity averages 41% but exhibits a slight overall trend of increasing porosity with depth, likely related to a large proportion of coarser grained

Figure F27. (A) RCB core diameter and (B) uncorrected and (C) corrected GRA bulk density with MAD bulk density (black dots), Hole U1519C.

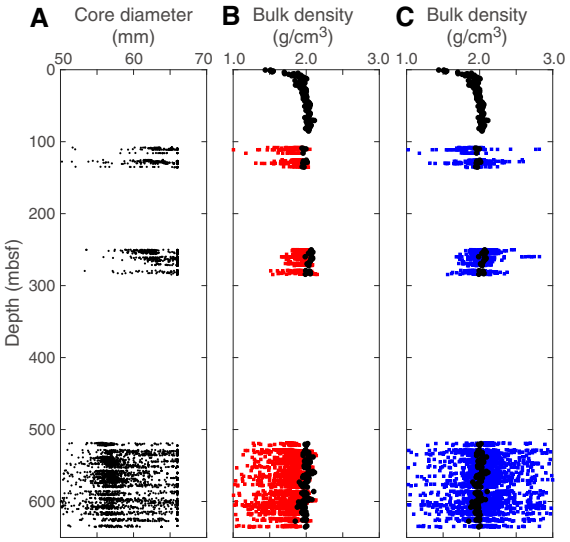

material in this interval. In general, porosity values and trends are consistent with values obtained by LWD nuclear magnetic resonance (NMR) and neutron porosity measurements (Figure F26).

P-wave velocity

P-wave velocity was measured on working halves and a limited number of discrete cubes (2 cm × 2 cm × 2 cm) at Site U1519. After careful investigation of the waveform data, it was discovered that most of the measurements on working halves were not real signals but system noise and that the only reliable data are from the upper 10 m of Holes U1519D and U1519E. Between 0 and 10 mbsf, *P*-wave velocity ranges from 1500 to 1600 m/s, consistent with LWD data in Hole U1519A (Figure F26) (see **Logging while drilling**). *P*-wave velocity on a limited number of discrete samples at ~560 mbsf (from Core 375-U1519C-18R) ranges from 1400 to 1700 m/s, which is much lower than LWD data in this depth interval (2300–2500 m/s).

Shear strength

Undrained shear strength increases from 0 to ~180 kPa with an average gradient of ~2.4 kPa/m between 0 and 85 mbsf in Holes U1519D and U1519E (Figure F26). The sediments were too indurated to measure strength using the automated vane shear (AVS) between 55 and 85 mbsf. Between 105 and 140 mbsf in Hole U1519C, shear strength remains mostly constant with an average value of ~62 kPa. Between 250 and 290 mbsf, shear strength estimated using the AVS is relatively constant with an average value of 30 kPa, whereas shear strength estimated using the penetrometer exhibits significant scatter and ranges between 29 and 307 kPa. In the cored interval of Hole U1519C deeper than 518 mbsf, the indurated sediments were measured only using the penetrometer. Between 518 and 635 mbsf, shear strength ranges 54–1104 kPa and averages ~319 kPa.

Thermal conductivity

Thermal conductivity measurements were conducted on sediment WR cores using the needle probe method on all samples shallower than 285 mbsf from Site U1519 (see **Physical properties** in the Expedition 372B/375 methods chapter [Wallace et al., 2019]). No measurements were conducted in the cored interval of Hole U1519C deeper than 518 mbsf, where the sediments were too stiff for a needle probe and too fragile for a half space probe. In most cases, three measurements were made with the needle probe at each measurement position. The plotted value in Figure F26 represents the mean of the three measurements, and the horizontal bar shows the standard deviation of the three measurements. Although a sample of three does not represent an accurate measure of the standard deviation, this value can be used to assess the relative scatter in the measurements.

From the seafloor to about 80 mbsf in Hole U1519E, thermal conductivity values range 0.8–1.6 W/(m·K). From 109 to 135 mbsf, thermal conductivity is relatively uniform at 1.3 W/(m·K), and deeper than 250 mbsf, thermal conductivity is about 1.4 W/(m·K).

Natural gamma radiation

Natural gamma radiation (NGR) values range from 18 to 67 counts/s at Site U1519 and are relatively uniform through the cored intervals, with an average of 40 counts/s (Figure F26). The NGR spectra were used to estimate ^{40}K, ^{232}Th, and ^{238}U concentrations using the algorithm presented by De Vleeschouwer et al. (2017) (Figure F28). K, Th, and U concentrations are relatively uniform through the cored intervals. Mean values of ^{40}K, ^{232}Th, and ^{238}U are 2.0 wt%, 5.1 ppm, and 1.4 ppm, respectively. These values likely reflect the low concentration of clay throughout the cored intervals.

Figure F28. Calculated K, Th, and U concentrations, Site U1519.

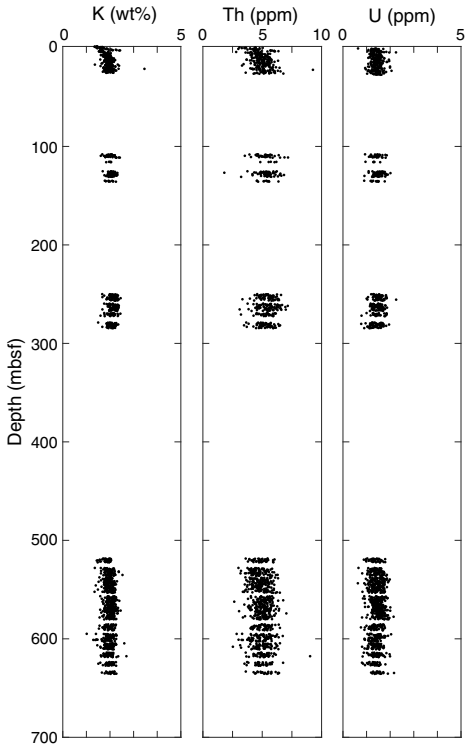

Magnetic susceptibility

Magnetic susceptibility is mostly constant from 0 to 150 mbsf, ranging between 10 × 10^{-5} and 30 × 10^{-5} SI (Figure F26). At ~1.5 and 3–4 mbsf, magnetic susceptibility is as high as 300 × 10^{-5} SI, corresponding to ash layers. Between 250 and 283 mbsf, magnetic susceptibility ranges from 15 × 10^{-5} to 20 × 10^{-5} SI. At 283 mbsf, it shifts to higher values of 40 × 10^{-5} to 50 × 10^{-5} SI, corresponding to the Lithostratigraphic Unit I/II boundary. Deeper than 518 mbsf, magnetic susceptibility is nearly constant at 10 × 10^{-5} SI.

Reflectance spectroscopy and colorimetry

Color reflectance data collected from archive halves are presented in the L*a*b* color space (Figure F26). L*, a*, and b* are nearly constant for the cored depth interval, with average values of 39, 1, and −1.4, respectively. From 0 to ~30 mbsf, L* and b* decrease gradually with depth from 50 to 40 and from 4 to −5, respectively, and a* increases from 0 to 1. From 30 to 285 mbsf, L*, a*, and b* are nearly constant at 35–42, 2, and −3, respectively. Deeper than 518 mbsf, a* and b* are both nearly constant at ~1 and L* decreases gradually with depth from 40 to 37 at 636 mbsf.

Downhole measurements

Formation temperature and heat flow

The APCT-3 was deployed eight times in Hole U1519E (Table T13). Two APCT-3s (1858002C and 1858005C) were each used for four measurements. All temperature measurements show a clear frictional heating spike upon insertion indicating that the tool pen-

Table T13. Advanced piston corer temperature tool (APCT-3) deployments and estimated formation temperatures, Hole U1519E. **Download table in CSV format.**

Core	Tool	Depth (mbsf)	Thermal resistance (m^2K/W)	Formation temperature (°C)
375-U1519E-				
4H	1858002C	31.3	25.6	6.44
5H	1858005C	40.1	30.8	6.72
6H	1858005C	49.6	39.9	6.97
7H	1858002C	57.0	44.3	7.18
8H	1858005C	62.3	47.3	7.27
9F	1858002C	67.0	51.6	7.28
11F	1858005C	76.4	58.2	7.46
13F	1858002C	85.8	65.0	7.91

Figure F29. Temperature-time series measured during APCT-3 1858002C deployment, Hole U1519E (purple line). Unshaded area = data used for equilibrium temperature fit, pink line = theoretical equilibrium curve, triangle = beginning of fit, inverted triangle = end of fit, diamond = temperature decay at ⅔ of the curve fitting window (not used), horizontal line = estimate of equilibrium temperature.

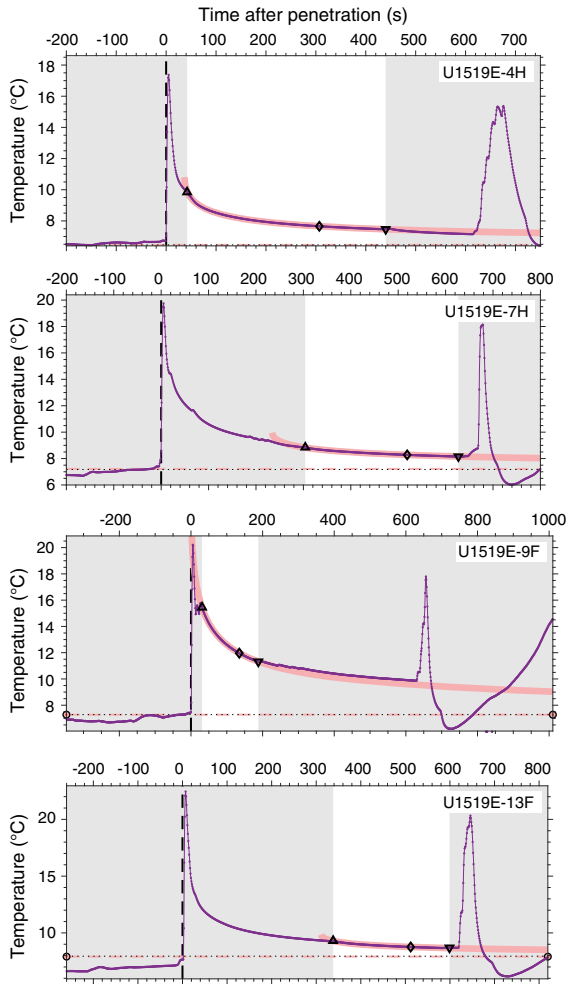

etrated the sediment (Figures **F29**, **F30**). Equilibrium temperatures are determined based on the cooling trend between the APCT-3 insertion time and the pull-out time. At this site, the majority of the

Figure F30. Temperature-time series measured during APCT-3 1858005C deployment, Hole U1519E (purple line). Unshaded area = data used for equilibrium temperature fit, pink line = theoretical equilibrium curve, triangle = beginning of fit, inverted triangle = end of fit, diamond = temperature decay at ⅔ of the curve fitting window (not used), horizontal line = estimate of equilibrium temperature.

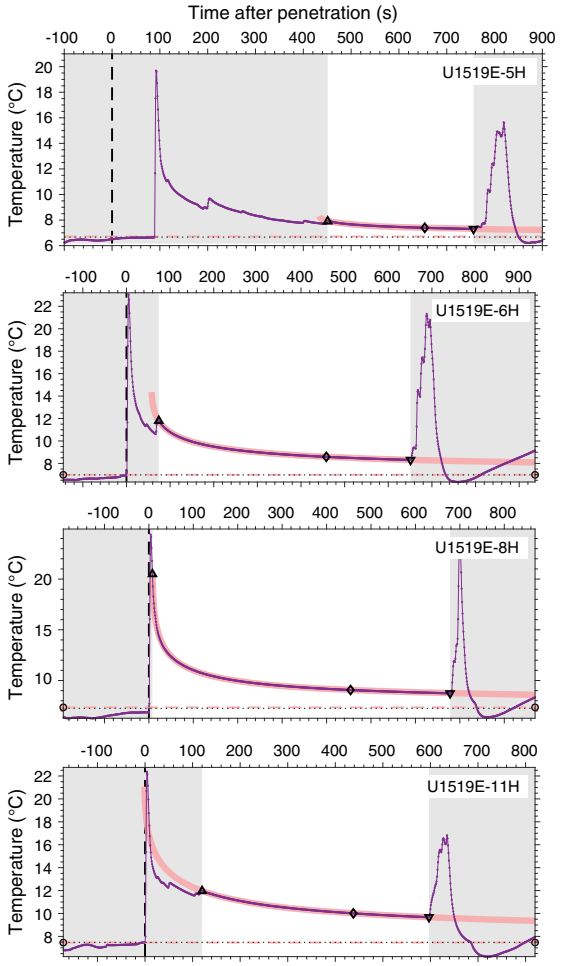

temperature decay curves show deviations from a smooth cooling trend indicating that the APCT-3 was likely disturbed, degrading the quality of temperature determinations. The one exception is the measurement associated with Core 375-U1519E-8H. Because of the disturbances, the decay curves were fit over the longest period of time containing a smooth record. Despite these problems, the APCT-3 measurements provide reliable estimates of the formation temperature.

Estimated equilibrium temperatures are plotted as a function of measurement depth (Figure **F31A**). The best-fitting thermal gradient to these data is 24.3°C/km. This fit yields an intercept corresponding to a bottom water temperature of 5.7°C, which is in good agreement with nearby bottom water temperature measurements made during the year-long Hikurangi Ocean Bottom Investigation of Tremor and Slow Slip (HOBITSS) deployment (Wallace et al., 2016) and expendable bathythermograph (XBT) casts made during R/V *Roger Revelle* Cruise RR1508 between 16 May and 18 June 2005. These water column temperature measurements show temperatures from 5.6° to 5.8°C at water depths between 990 and 1000

Figure F31. A. Estimated equilibrium temperatures vs. depth. Red dots = APCT-3 Shoe 1858005C, black dots = APCT-3 Shoe 1858002C, black line = best-fitting thermal gradient of 0.024°C/m extrapolated to bottom of Hole U1519E. B. Estimated equilibrium temperatures vs. thermal resistance. Black line = best-fitting heat flow of 33 mW/m^2.

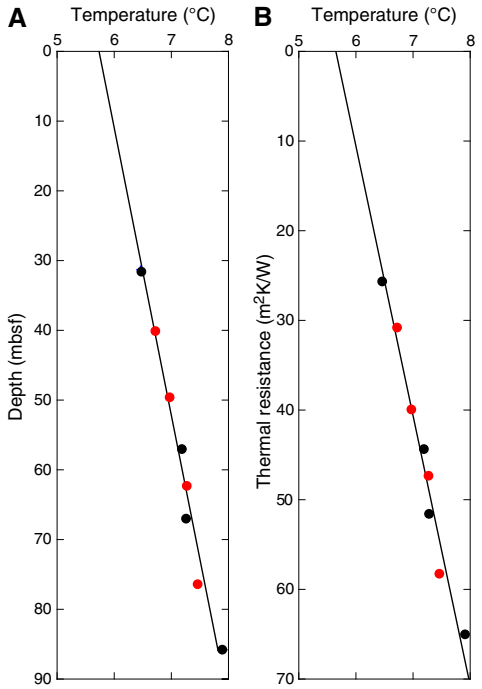

m. The consistency of the bottom water temperature measurements with the estimate of bottom water temperature based on the fit to the equilibrium temperatures adds confidence to the APCT-3 results. To estimate the vertical conductive heat flow (q), we use Fourier's law:

$$q = k\Gamma,$$

where k is the thermal conductivity and Γ is the thermal gradient. The mean thermal conductivity is 1.31 W/(m·K) (see **Physical properties**) and is combined with the best-fitting thermal gradient to yield a heat flow value of 32 mW/m^2.

A second method for estimating the conductive heat flow takes into account variations in thermal conductivity measured separately on core samples using the relationship (Bullard, 1939)

$$T(z) = T_0 + q\sum_{i=1}^{N}\frac{\Delta z_i}{k(z)_i},$$

where

T = temperature,
z = depth,
T_0 = bottom water temperature, and
$\sum_{i=1}^{N}\frac{\Delta z_i}{k(z)_i}$ = summed thermal resistance,

where $k(z)_i$ is the individual thermal conductivity value and Δz_i is the distance between adjoining thermal conductivity measurements.

In practice, q and T_0 can be estimated by plotting $T(z)$ against thermal resistance between the seafloor and the depth of the temperature measurement (Figure **F31B**). The thermal resistance of the sediment overlying each APCT-3 measurement is given in Table **T13**. The heat flow estimate defined by the slope of the least-squares linear fit is 33 mW/m^2 (Figure **F31B**), which is close to the estimate using Fourier's law. The estimated bottom water temperature using this technique is 5.6°C.

The heat flow value at Site U1519 is lower than regional heat flow values of ~50 mW/m^2 near the trench decreasing landward to 35 mW/m^2 estimated based on BSRs (Henrys et al., 2003; Townend, 1997). This heat flow is also lower than the 49 mW/m^2 estimated at Site U1517 (16 km to the southwest) (Barnes et al., 2019) but higher than shallow probe values (~27 mW/m^2) obtained in the same location (Antriasian et al., 2018).

Logging while drilling

The LWD data for Hole U1519A were collected with a BHA composed of six LWD tools attached behind the bit (from bottom to top): geoVISION, NeoScope, StethoScope, TeleScope, SonicScope, and proVISION. These tools provide a wide array of measurements including gamma ray (geoVISION and NeoScope), resistivity (geoVISION and NeoScope), porosity (NeoScope and proVISION), and compressional (P-wave) and shear (S-wave) wave velocity (SonicScope) as described in **Logging while drilling** in the Expedition 372B/375 methods chapter (Wallace et al., 2019). The StethoScope probe was not deployed at this site; therefore, the tool only collected APWD measurements.

Drilling parameters

In the composite plot of drilling parameters (Figure **F32**), the data are displayed according to the LWD operations period starting on 23 December 2017 at 2258 h (UTC + 13 h) and terminating on 25 December at 1246 h. The average rate of penetration (ROP) was ~40 m/h at ~40 mbsf and was gradually slowed over the depth of the hole to ~20 m/h at ~560 mbsf. Below ~560 mbsf, the ROP was increased to ~40 m/h. The drilling pipe rotation rate was ~20 rpm as the borehole was spudded, increased to ~50 rpm at ~80 mbsf, and then stayed close to this value for the remainder of the borehole. Weight on bit (WOB) ranged between −10 and 10 klb. From ~16 to 398 mbsf, WOB was ~4 klb. Below ~398 mbsf, WOB fluctuated between about −1 and 18 klb. Annular pressure increased progressively with depth. At the seafloor, the measured annular temperature was ~6°C; it increased to ~12°C at the bottom of the borehole.

Data quality

In general, the highest quality logging measurements are collected when the borehole is close to bit size. Thus, borehole conditions were assessed by the ultrasonic caliper measurement of borehole diameter to define zones of borehole enlargement, or washouts (Figures **F32**, **F33**). The ultrasonic caliper, however, can incorrectly identify intervals with extreme borehole enlargement (>5 cm) and instead report values close to the bit size (8.5 inch); therefore, porosity and resistivity measurements were also used to identify enlarged or washout intervals. These zones are characterized by anomalously low resistivity (~0.3–0.9 Ωm) and unrealistically high porosity (~0.7–1.0), both of which imply that measurements are affected by a large volume of seawater between the tool and borehole wall. Degraded borehole conditions are more

Figure F32. Drilling parameters, Hole U1519A.

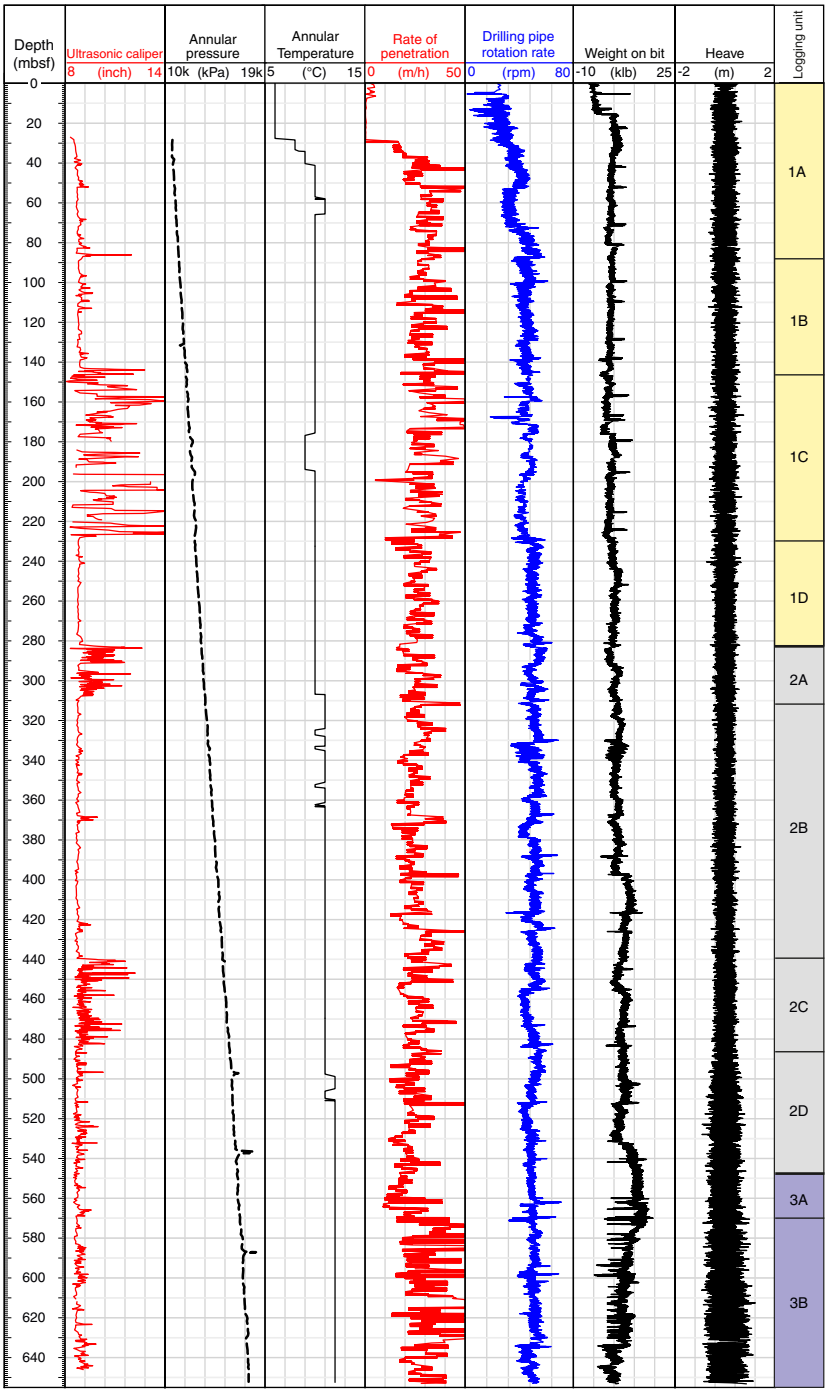

likely in intervals with less cohesive sediment such as sand and silt with little clay. In finer grained (typically clay-rich) intervals, the borehole is likely to be closer to bit size.

The NMR data are generally of good quality, but the transverse relaxation time (T_2) distribution is truncated to values between 1 and 1000 ms (Figure **F33**). Therefore, not all of the clay-bound water (which typically ranges from 0.3 to 3 ms) is recorded. Additionally, the largest pores in coarse sediments and any open pore space or washouts are recorded as a long NMR T_2 peak between 50 and 500 ms rather than an expected peak position at 1000 ms.

A GVR resistivity image log was acquired from 0 to 650 mbsf in Hole U1519A (Figure **F34**). The image log is of variable quality. Poor image log quality is due to a combination of missing data, image log stretching effects, horizontal image log artifacts, and spiral-hole image log artifacts. Missing data and image stretch reduce image quality significantly from 0 to 5 mbsf. At 120–130, 228–281, 370–439, and 483–591 mbsf, spiral-hole image artifacts are evident and reduce image quality, but geological features can still be observed. Image stretching is significant at 241, 281–291, 296, 305, 438–450, 535, and 558 mbsf. From 142 to 228 mbsf, image quality is

Figure F33. LWD measurements, Hole U1519A.

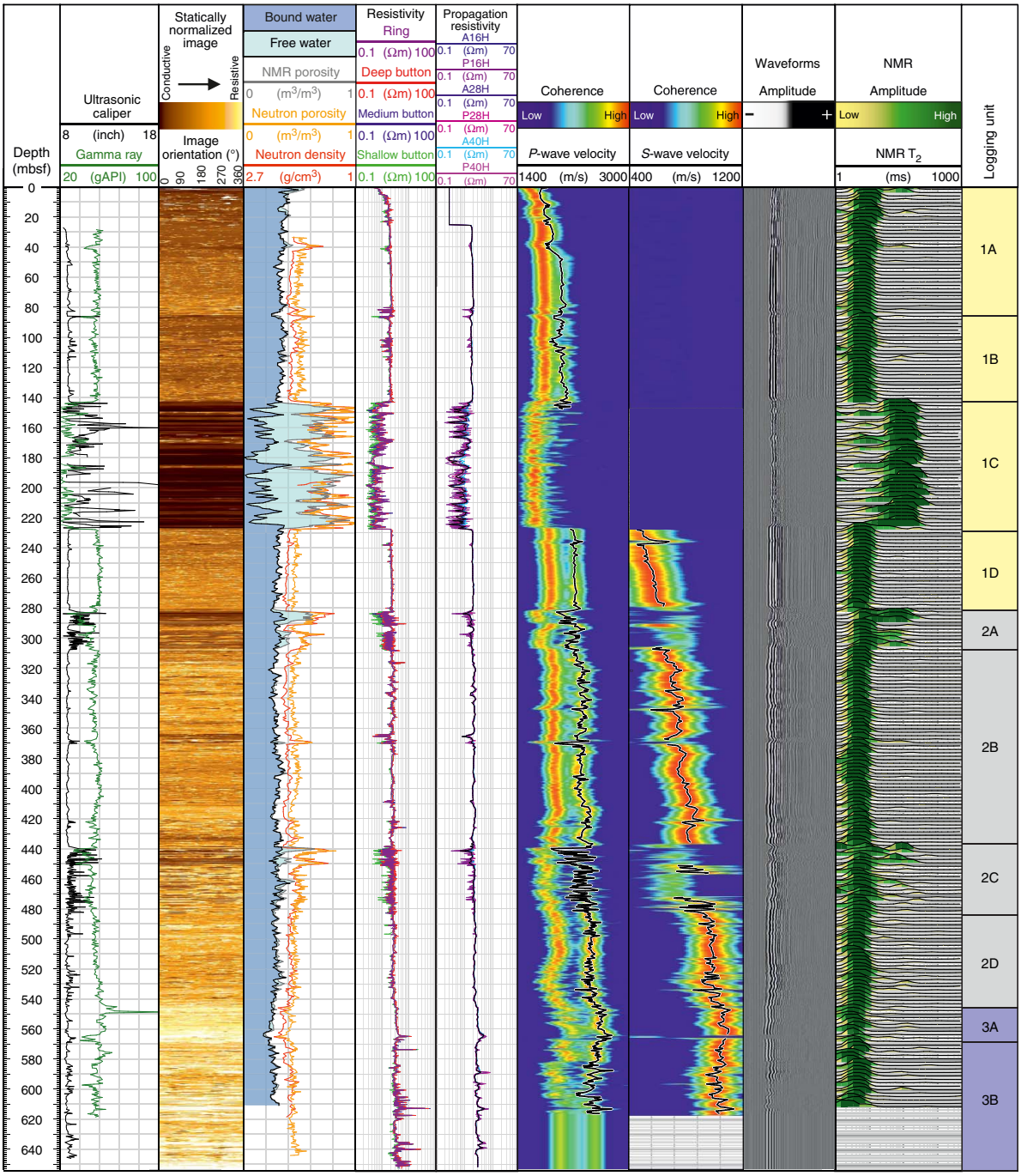

very poor because of washout of the borehole over a sandy unit (Logging Subunit 1C). Horizontal image artifacts are common throughout the imaged interval and are thought to be related to stick and slide as the resistivity buttons rotate around the borehole, possibly smearing the sediments being drilled through.

Logging units

The combination of different LWD measurements allowed us to define three logging units (Figures **F33**, **F34**) that correspond approximately to major seismic units defined in this area of the Tuaheni Basin (Seismic Units 1–3; see **Core-log-seismic integration**).

Logging Unit 1 (0–281.5 mbsf)

Logging Unit 1 is divided into four subunits based on significant changes in logging responses.

Logging Subunit 1A (0–86 mbsf) shows a short, unimodal NMR T_2 response that indicates a dominance of bound water in small pores and very little free water, implying the sediment is uniformly fine grained sediment. The gamma ray response is uniform with an average value of 50 gAPI. Aside from the near-seafloor sediments (0–5 mbsf), resistivity in this logging subunit is also generally uniform with a value of 2.0 Ωm, except for small decreases adjacent to very thin intervals that likely represent the presence of washed out, coarse-grained sediments (e.g., ~41 mbsf). Neutron porosity de-

Figure F34. Resistivity image log data with interpretation of bedding, fracture, and borehole breakout orientation, Hole U1519A. Ticks on fracture and bedding symbols point in the dip direction, as defined in the legend. Borehole breakout orientations are shown by long axes of pink ovals; "dip angle" is arbitrary for borehole breakouts.

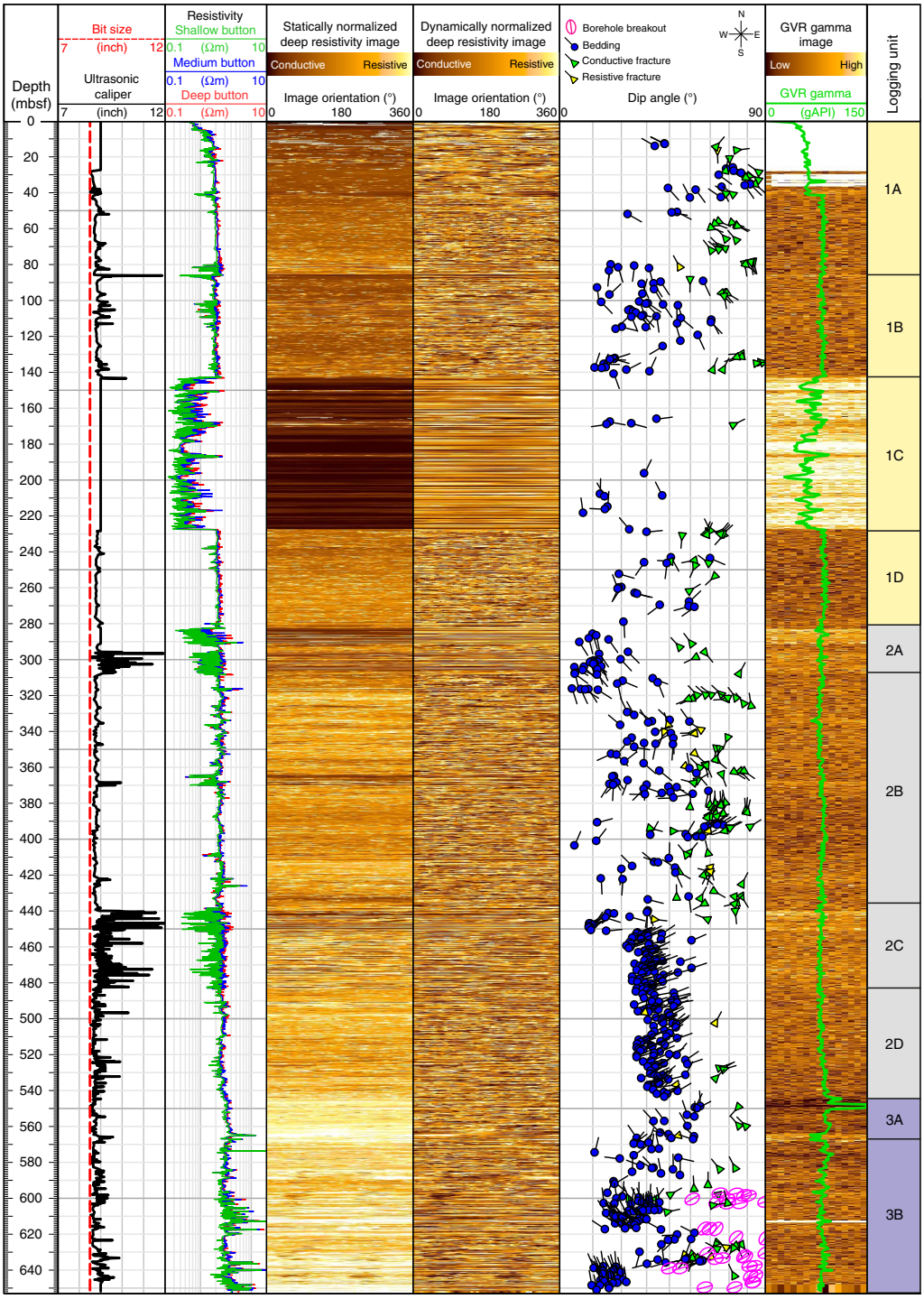

creases from ~0.55 to ~0.45 through this logging subunit. Compressional wave velocity increases from 1550 to 1725 m/s, although measurements between 0 and 50 mbsf are likely inaccurate because of borehole enlargement. Bedding is difficult to resolve from the resistivity image logs, but identified beds have moderate to high dip angles (~15°–80°) to the southeast or northwest (Figure **F34**). Steeply dipping image log features identified as bedding require further investigation to confirm their classification and interpret the steep dip angles. A number of conductive fractures and one resistive fracture, dipping 60°–90° to the southeast or northwest, are observed in this logging subunit.

Logging Subunit 1B (86–143 mbsf) is defined based on a small decrease in resistivity that can be seen in the statically normalized resistivity image log as a change to a darker color. Resistivity averages 1.9 Ωm. Neutron porosity is close to 0.50 throughout this logging subunit, and gamma ray is uniform at around 50 gAPI. The NMR T_2 distribution remains unimodal and similar to Subunit 1A. Bedding is easily identified from the resistivity image logs, with a range of dip angles (10°–60°) dipping dominantly to the southeast from 86 to 130 mbsf and to the east from 130 to 143 mbsf. Some thin conductive intervals are observed throughout this logging subunit and may be washed out, coarse-grained sediment beds. *P*-wave velocity increases from 1700 to 1875 m/s through the subunit with local decreases in thin bedded intervals between 101 and 110 mbsf. High-angle conductive fractures are observed dipping (65°–70°) to the southeast at ~97 mbsf and between 70° and 90° to the east and west from 130 to 140 mbsf.

Logging Subunit 1C (143–227.5 mbsf) shows a long NMR T_2 peak and low gamma ray (~20 gAPI) indicating an interval of relatively uniformly coarse grained sediment. Resistivity and velocity are low and porosity is high; these measurements are most likely affected by washout in this logging subunit. The attenuation resistivity measured at low frequency (A40L), which is the least affected of all the curves, reads 1–1.6 Ωm. Only occasional narrow depth intervals capture any usable image log data, and few geological features are observed.

Logging Subunit 1D (227.5–281.5 mbsf) shows signatures similar to those in Logging Subunit 1B, with gamma ray of ~50 gAPI and low T_2 distributions inferred to represent uniform fine-grained sediments. Resistivity is uniform (~2 Ωm), punctuated very occasionally by thin, more conductive beds. *S*-wave velocity is first resolved in this logging subunit starting at ~450 m/s near the top and increases to ~700 m/s at the base. Bedding identified from the resistivity image logs is sparse with no consistent orientation. At the top of this logging subunit, a cluster of conductive fractures are observed dipping 55°–70° to the northeast.

Logging Unit 2 (281.5–546.0 mbsf)

Logging Unit 2 corresponds to Seismic Unit 2 and lies beneath an onlapping and locally unconformable horizon below Logging Unit 1 (Seismic Unit 1), the present basin depocenter (see **Core-log-seismic integration**). Four subunits are identified from the LWD data.

Logging Subunit 2A (281.5–308.5 mbsf) is characterized by a bimodal NMR T_2 distribution that indicates a coarse sediment package with large pore sizes interrupted by a small interval of uniform fine sediments at 291–293.5 mbsf. The upper coarse sediment interval exhibits large resistivity oscillations, and bedding dips from 5° to 15° to the southeast. The lower coarse sediment interval shows distinct thin bedding with dips from ~5° to ~20° to the southeast, and bedding thickness increases with depth. Compressional wave velocity in this logging subunit is variable between 1800 and 2000 m/s and is affected by borehole quality; no shear wave velocity is recorded in this logging subunit.

Logging Subunit 2B (308.5–438.5 mbsf) consists of uniformly fine grained sediments interpreted from the unimodal, short NMR T_2 distribution and uniform gamma ray around 50 gAPI. Neutron porosity varies in a narrow range from 0.42 to 0.45. *P*-wave and *S*-wave velocities increase steadily with depth from 2200 to 2400 m/s and from ~510 to 620 m/s, respectively. Bedding observed from the resistivity image logs in this logging subunit is nonuniform in both dip angle and azimuth. Numerous fractures, both conductive and resistive, are present throughout this logging subunit, with dip angles 30°–90° and variable dip azimuths (Figure **F34**).

The pattern of NMR T_2 distribution in Logging Subunit 2C (438.5–483 mbsf) is distinct with the proportion of the longer T_2 peak increasing where more conductive beds occur. Bed dips are clearly defined and consistent throughout the subunit, dipping dominantly 20°–40° to the northeast. Neutron porosity is uniform at ~0.45, although large increases occur over specific thin beds suggesting the presence of coarse-grained sediments and/or borehole washouts. Gamma ray ranges from 20 to 50 gAPI, and the lowest values are most likely influenced by the borehole washout. This logging subunit is interpreted to be a stack of turbidite sequences with coarse-grained layers as thick as 10 cm. The Logging Subunit 2C/2D boundary is gradational.

Logging Subunit 2D (483.0–546.0 mbsf) consists of uniform fine sediments with occasional thin layers of coarser sediments, as indicated by a dominantly unimodal, small NMR T_2 distribution. Neutron porosity decreases from around 0.5 at the top to 0.46 at the base. The resistivity response is relatively constant at ~2.3 Ωm. *P*-wave and *S*-wave velocities both increase through the logging subunit, reaching 2300 and 1000 m/s at the base, respectively. Bedding dips are consistently 20°–45° to the northeast.

Logging Unit 3 (546–650 mbsf)

The Logging Unit 2/3 boundary is placed above a notable spike in gamma ray at 549 mbsf where density and resistivity show an inflection toward higher values and bedding orientations change from the consistent measurements in Logging Subunit 2D to variable orientations in the upper interval of Logging Unit 3 (546–600 mbsf). Logging Unit 3 contains two logging subunits defined on the basis of different velocity, density, and resistivity characteristics.

Logging Subunit 3A (546–567 mbsf) is characterized by higher resistivity, lower porosity, and higher density than overlying Logging Unit 2. Gamma ray is highly variable in contrast to other logging units. For example, the presence of a very high gamma ray spike (>100 gAPI) at ~550 mbsf likely marks the presence of volcanic ash (see **Lithostratigraphy**). *P*-wave velocity increases to 2500 m/s, the highest value in Hole U1519A, at the base of the subunit, and *S*-wave velocity reaches 1020 m/s. The resistivity image log in Logging Subunit 3A is more resistive (brighter) than in overlying logging units and contains thin (centimeter to ~1 m scale), highly resistive beds interpreted to be gas hydrate–filled, coarse-grained sediment layers. Bedding orientations are inconsistent, and three conductive fractures are noted in this logging subunit.

Logging Subunit 3B (567–650 mbsf) marks a gradational change from Logging Subunit 3A to slightly higher porosity, slower *P*-wave and *S*-wave velocities, and the occurrence of spikes of high resistivity (>10 Ωm on button resistivity measurements) and high *P*-wave velocity. From 620 to 640 mbsf, a mix of conductive and resistive fractures dip 45°–80° dominantly to the southwest. The *P*-wave velocity spikes coincide with centimeter to ~1 m scale, resistive (bright) layers and with intervals on the resistivity image logs interpreted to be gas hydrate–filled, coarse-grained sediment layers. These coarse-grained layers likely map to turbidite sequences noted in the core (see **Lithostratigraphy**). Bedding orientations vary with depth: bedding is inconsistent from 567 to 595 mbsf, dips 15°–35° to the north-northwest between 595 and 620 mbsf, is again inconsistent from 620 to ~635 mbsf, and dips ~10°–20° to the north-northwest from 635 mbsf to the bottom of the borehole.

Borehole breakouts are observed in the resistivity image logs in Logging Subunit 3B between 595 and 650 mbsf (Figure **F34**). Bore-

hole breakout azimuths are dominantly aligned ~054°/234° (northeast–southwest) from which we infer a northeast–southwest S_{hmin} orientation and a northwest–southeast S_{Hmax} orientation in this interval. Preliminary measurements of borehole breakout widths range from 33.9° to 83.6°.

Core-log-seismic integration

Depth scale

During Expedition 372, LWD data were acquired in Hole U1519A. The seafloor was penetrated at 1000.7 mbsl, and data were collected to a total depth of 650 mbsf (see **Logging while drilling**). During Expedition 375, Hole U1519B was drilled for the emplacement of an observatory, and the seafloor was tagged at 1000.4 mbsl (see **Operations**). Coring took place in Holes U1519C, U1519D, and U1519E, and the seafloor was measured at 1000.3, 1000.4, and 1000.3 mbsl, respectively. Spot-coring with the RCB system took place in Hole U1519C at 108.0–163.6, 250.0–288.4, and 518.4–640 mbsf. APC coring was done in Hole U1519D from 0 to 23.64 mbsf and in Hole U1519E from 0 to 85.8 mbsf.

Holes U1519A and U1519C are located 40 m apart, and all holes at Site U1519 lie on Seismic Line 05CM-04 (Figure **F1**) (see **Background and objectives**). Because of minor differences in seafloor depth, close proximity of the LWD and coring sites, and relatively simple geological structure, it is possible to conduct a correlation of the core, log, and seismic data with no depth shifting required.

Seismic-well ties

A seismic-well tie is needed to correlate physical properties changes in the logging data, lithostratigraphic units and structural domains in cores, and seismic reflections and seismic facies units to extrapolate results from drilling at Site U1519 over the Tuaheni Basin and surrounding slopes. Holes U1519A and U1519C intersect Seismic Line 05CM-04 at common depth points (CDPs) 2038 and 2041, respectively. To correlate seismic data (recorded in time) and log/core data (recorded in depth), it is necessary to develop an accurate time-depth relationship. *P*-wave velocity data were acquired by the SonicScope LWD tool in Hole U1519A, providing velocity information from 0 to 617 mbsf (see **Logging while drilling**).

The LWD *P*-wave velocity logs were compared with seismic velocity estimates produced for the depth migration of Seismic Line 05CM-04 (Barker et al., 2018) and a full waveform inversion (FWI) (see **Core-log-seismic integration** in the Expedition 372B/375 methods chapter [Wallace et al., 2019]) (Figure **F35**). LWD *P*-wave velocity is generally higher than the prestack depth migration (PSDM) model (Barker et al., 2018) from 150 to 400 mbsf. The FWI velocity model matches the average LWD velocity from the seabed to 617 mbsf and also detects a velocity inversion at 580 mbsf, which is close to a significant velocity inversion observed in the LWD data at 564 mbsf. The PSDM and FWI velocity models predict a very similar time-depth relationship, and both models slightly underestimate depth from 200 to 650 mbsf.

The LWD logs provided a more direct measurement of *P*-wave velocity at Site U1519 than the pre-expedition seismic velocity models. Therefore, the LWD *P*-wave velocity log was used to perform the depth-time conversion in the production of a synthetic seismic trace (Figure **F36A**). No *P*-wave velocity data were collected between 148 and 227 mbsf because of a significant borehole washout, so velocity values were linearly interpolated across this interval. The *P*-wave velocity log was then smoothed over 20 samples (sampling interval of 15 cm) to produce a profile relevant to the vertical

Figure F35. A. Comparison of Hole U1519A V_P data with pre-expedition PSDM and FWI velocity profiles near the site. UTIG = University of Texas Institute for Geophysics. FWI velocity model provided by R. Bell (unpubl. data; Imperial College London, United Kingdom). B. Comparison of time-depth relationships derived from different V_P data sets. Both PSDM velocity models from Barker et al. (2018).

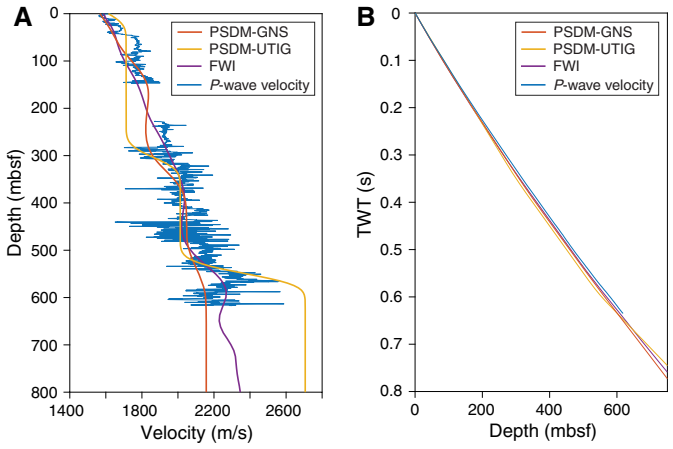

resolution of the seismic data. The LWD sourceless neutron-gamma density log from Hole U1519A was used in the construction of the synthetic seismic-well tie from 0 to 611 mbsf. The density log was smoothed over 20 samples (sampling interval of 15 cm).

Following testing using analytical, statistical, and deterministic wavelet extractions, a preferred wavelet was selected from Profile 05CM-04 by stacking 10 adjacent seismic traces from a flat region of the seafloor close to but not intersecting Site U1519 (between CDPs 2090 and 2100) to yield a high signal-to-noise ratio (Figure **F36**). This wavelet was convolved with the reflection coefficient log measured in two-way traveltime (TWT) to produce a synthetic seismic trace that can be compared with Seismic Line 05CM-04 in the vicinity of CDP 2038 near Site U1519.

The resulting synthetic seismic trace in the time domain is shown in Figure **F36A**, together with the real seismic data (Line 05CM-04, CDPs 2028–2048), with no depth shifts applied. Some significant high-amplitude reflections predicted by the synthetic, such as around 200–300 mbsf, match the seismic data. Very high amplitude reflections predicted around 130–200 mbsf may be exaggerated by reduced velocity and density values caused by borehole collapse in this area (see **Logging while drilling**). The synthetic also reproduces a zone of low-amplitude reflectivity from 475 to 550 mbsf (Figure **F36A**).

At 425–450 mbsf, it appears that a mismatch occurs between a high-amplitude, reversed polarity reflection in the data and synthetic. We note that this high-amplitude reflection is caused by a large decrease in density and velocity in an area where the caliper increases at 440 mbsf (see **Logging while drilling**). A reversed polarity reflection occurs in the data at 442 mbsf; however, there appears to be an even higher amplitude, reversed polarity reflection at a shallower depth of 425 mbsf (Figure **F36A**). We do not think that the reflection predicted in our synthetics at 440 mbsf represents the reflection at 425 mbsf because it would require the sediment velocity from 300 to 400 mbsf to be ~200 m/s faster than that measured by LWD. Instead, we suggest that the smaller amplitude, reversed polarity reflection in our synthetics at 420 mbsf represents the observed reflection at 425 mbsf. Subsequently, the very high amplitude reflection in our synthetics at 440 mbsf is in fact the observed

Figure F36. A. Synthetic seismic-well tie to Line 05CM-04 at CDP 2037 produced using LWD sonic and density data from Hole U1519A. RC = reflection coefficient. Inset shows source wavelet used that was produced from stacking 10 wavelets from an area of flat seabed. B. Preferred synthetic seismic-well tie produced by conducting small depth shifts to match reflections. Output velocity shows minor variations in velocity needed to account for depth shifts.

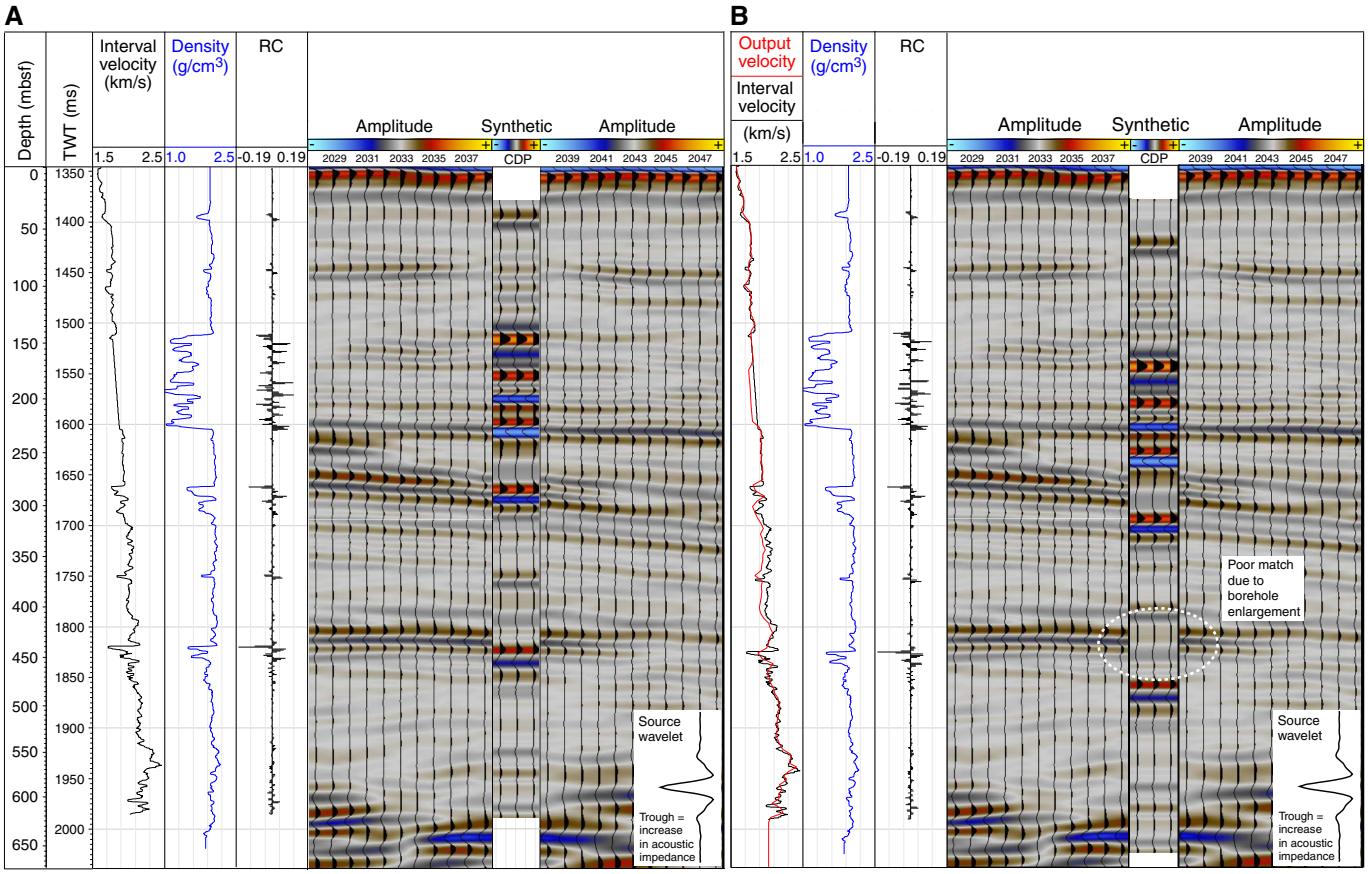

reflection at 442 mbsf, but the amplitude of the latter is artificially enhanced because of borehole washout.

Minor changes to the velocity log (red line, Figure **F36B**) allow the synthetic trace and real seismic reflections to be brought into slightly closer alignment. The discrepancies between the velocity required by the seismic-well tie and the real velocity logs could be the result of reduced quality *P*-wave velocity measurement because of washouts. The close match between the synthetic trace and Line 05CM-04 provides a high-confidence correlation between the LWD, core, and seismic reflection data.

Seismic stratigraphy, seismic units, and comparison with log and core data

Three major seismic reflection units are defined at Site U1519. In Figures **F37** and **F38**, the broader seismic stratigraphic architecture of the units is highlighted and compared with unpublished pre-expedition seismic stratigraphy (P. Barnes, unpubl. data). In Figure **F39**, the units are shown in meters below seafloor converted from time using the seismic-well tie (Figure **F36**; Table **T14**) and are compared with the logging units defined by LWD (see **Logging while drilling**).

Below, we describe the reflection and logging characteristics of each seismic unit and discuss the in situ physical properties that lead to the observed reflection characteristics. At 0–85.8, 108.0–163.6, 250.0–288.4, and 518.4–640 mbsf, we also tie lithologic, biostratigraphic, and core-based physical properties to the seismic data to enable interpretation of the depositional environment and history in the vicinity of Site U1519. Using a combination of correlation panels, crossplots, and the seismic-well tie, we discuss the character of each seismic unit, including lithologic and biostratigraphic information from the cored intervals (Figures **F40**, **F41**, **F42**) (see **Lithostratigraphy** and **Biostratigraphy**).

Seismic Unit 1 (0–281.5 mbsf)

Seismic Unit 1 (0–281.5 mbsf) is a near-horizontal basin fill sequence that onlaps Seismic Unit 2 in a landward direction and partly buries a thrust-faulted sequence beneath the eastern side of the Tuaheni Basin. Seismic Unit 1 correlates with Logging Unit 1 and Lithostratigraphic Unit I (Figure **F39**) (see **Logging while drilling** and **Lithostratigraphy**).

The upper part of Seismic Unit 1 above Reflection B4 (141 mbsf) (Figures **F37**, **F38**) is characterized by generally weakly reflective intervals with low-amplitude and chaotic discontinuous reflections and interspersed more continuous high-amplitude reflections. This sequence is interpreted to comprise at least two stacked MTDs separated by relatively thin intervals of layered sediments. Multibeam bathymetry (30 kHz) and seismic reflection data show that the upper MTD is the debris field associated with the North Tuaheni Landslide (Mountjoy et al., 2009, 2014). High-resolution seismic data show that this deposit is covered regionally by a veneer of more reflective sediment that ranges from ~0 to 25 m thick (e.g., Figure **F38**).

Figure F37. Seismic Units 1–3 near Site U1519 on Seismic Line 05CM-04. Labeled horizons are from P. Barnes (unpubl. data). Inset map shows location of available seismic profiles (yellow and white lines) and specific sections illustrated here and in Figure F38 (black lines). White bars on borehole site show sections cored in Holes U1519C–U1519E (labels indicate depth in mbsf). Prestack time migration (PSTM) seismic depth section provided by D. Barker (GNS Science) (05CM-04 PSTM HDVA-8 model) (Barker et al., 2018).

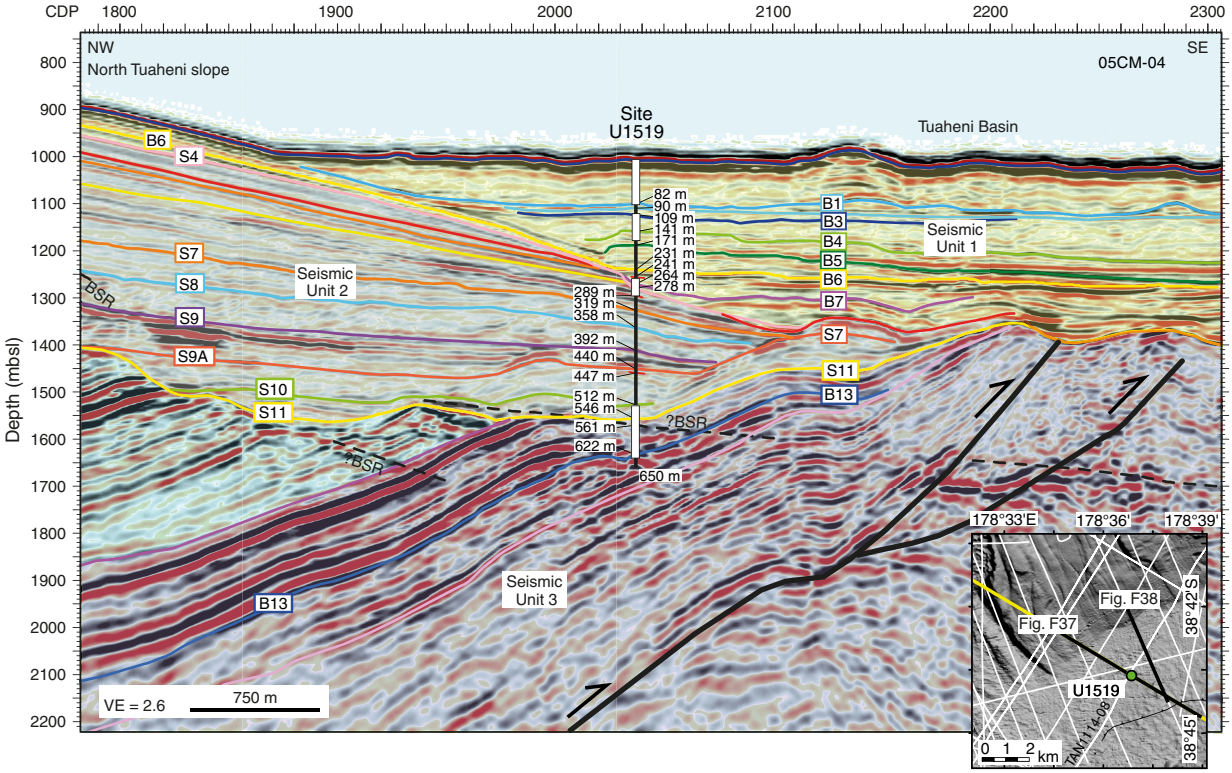

The upper part of Seismic Unit 1 above Reflection B4 (141 mbsf) coincides with Logging Subunits 1A and 1B (Figures **F39**, **F40**). These subunits are characterized predominantly by uniform gamma ray values of ~65–70 gAPI, in-gauge borehole conditions, and fairly uniform resistivity of about 2 Ωm that increases slightly with depth (see **Logging while drilling**). APC cores from Holes U1519D (0–23 mbsf) and U1519E (0–85 mbsf) indicate that the upper 137 m of Seismic Unit 1 comprises hemipelagic mudstone with silty turbidites. The inferred sediment veneer in the upper 10 m interval is characterized by very low resistivity of <2 Ωm and a 1 m thick volcanic ash. Biostratigraphy indicates that the upper 5 m is Holocene age and the underlying sequence to 141 mbsf is younger than 0.53 Ma (see **Biostratigraphy**).

The lower part of Seismic Unit 1 comprises two intervals. The interval between Reflections B4 and B6 (~141–231 mbsf) is characterized by strong, discontinuous reflections with locally channelized geometry and unconformable relationships. This interval coincides with Logging Subunit 1C, which is characterized by an abrupt decrease in resistivity, density, and gamma ray associated with borehole washout and loss of sonic data. No core was recovered from this interval that is inferred to be noncohesive and coarse grained. The underlying interval between Reflections B6 and S4 (~231–281 mbsf) comprises a generally weakly reflective sequence containing at least one seismic unconformity marked by Reflection B7 (Figure **F38**). This interval coincides with Logging Subunit 1D, which has uniform density, gamma, and resistivity and in-gauge borehole conditions. RCB cores from Hole U1519C (108–281 mbsf) indicate this interval comprises mudstone (Figure **F41**). The lower part of Seismic Unit 1 is dated as younger than 0.53 Ma (see **Biostratigraphy**).

The base of Seismic Unit 1 is a clear angular unconformity marked locally by Seismic Reflection S4 (Figures **F37**, **F38**). Modeling of the synthetic seismic trace (Figure **F36**) indicates that the contact is a reversed polarity reflection resulting from an abrupt decrease in density and velocity. This feature coincides with the negative-amplitude phase immediately beneath Reflection S4 (Figures **F39**, **F41**). The unconformable nature of the contact is not developed regionally but is localized in the vicinity of Site U1519. Away from the site, the phase of the reflection marking the base of Seismic Unit 1 differs depending on the physical properties and lithologies above and below the contact (Figures **F37**, **F38**).

The LWD data indicate that the base of Seismic Unit 1 is marked by an increase in gamma ray, density, resistivity, and *P*-wave velocity and a decrease in porosity (see **Logging while drilling**). Resistivity images reveal changes in bedding orientations across the Seismic Unit 1/2 boundary (Figure **F41**). RCB Section 375-U1519C-12R-3 indicates the contact occurs across mudstones that have a marked change in color and a slight change in grain size that coincides with an abrupt increase in magnetic susceptibility (Figure **F41**) (see **Lithostratigraphy**). The biostratigraphic data do not resolve a detectable change in age across the boundary (see **Biostratigraphy**).

Seismic Unit 2 (281.5–546 mbsf)

Seismic Unit 2 (281.5–546 mbsf) is characterized by a layered slope sequence of easterly dipping low- to high-amplitude reflection intervals that are locally truncated at the unconformity between

Figure F38. Seismic Units 1–3 near Site U1519 on Seismic Line TAN1404-P3106. Labeled horizons are from P. Barnes (unpubl. data). Inset map shows location of available seismic profiles (yellow and white lines) and specific sections illustrated here and in Figure F37 (black lines). Seismic data provided by J. Mountjoy (National Institute of Water and Atmospheric Research [NIWA], New Zealand) and S. Krastel (Kiel University, Germany).

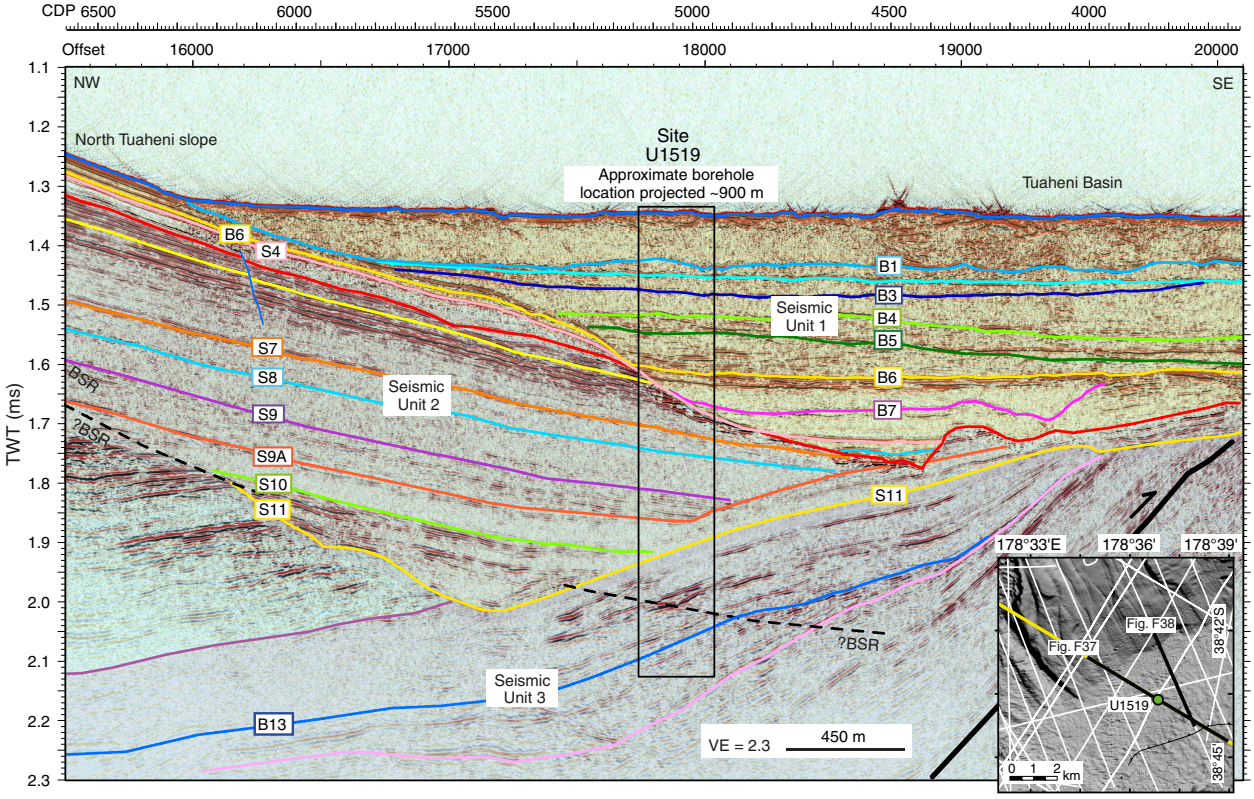

Seismic Units 1 and 2 (Figures **F37**, **F38**). This unit directly underlies the seafloor beneath the North Tuaheni slope and the western part of Seismic Unit 1. At Site U1519, the unit correlates directly with Logging Unit 2 (see **Logging while drilling**) (Figure **F39**) and most of Lithostratigraphic Unit I (see **Lithostratigraphy**) (Figures **F41**, **F42**).

The upper part of Seismic Unit 2 immediately below the unconformity and between Seismic Reflections S4 and S7 (281–319 mbsf) is strongly reflective. The seismic reflection intervals below are generally low amplitude and continuous between Reflections S7 and S8 (319–358 mbsf), chaotic and discontinuous between Reflections S8 and S9 (358–392 mbsf), high amplitude and continuous between Reflections S9 and S9A (392–440 mbsf), and weak and discontinuous between Reflections S9A and S11 (440–546 mbsf) (Figures **F37**, **F38**). The unit between Reflections S8 and S9 is interpreted to be an MTD. Bedding orientations in the lower portion of Seismic Unit 2 (440–546 mbsf) dip 20°–40° to the northeast as observed from resistivity image logs (see **Logging while drilling**).

The interval corresponding to Seismic Unit 2 includes Logging Subunits 2A–2D (Figure **F39**), which have physical properties that separate into distinct groups on crossplots involving gamma ray, *P*-wave velocity, density, and resistivity (Figure **F40**) (see **Logging while drilling**). The entire seismic unit is characterized by irregular but overall increasing *P*-wave velocity. The resistivity, density, gamma, and porosity logs show fairly uniform values throughout Seismic Unit 2, with notable excursions generally associated with higher amplitude seismic reflections, including Reflections S7, S8, and S9A (Figure **F36**).

The base of Seismic Unit 2 is defined by a regional erosional unconformity marked by Reflection S11 (Figures **F37**, **F38**). At Site U1519, however, the precise location of the unconformity is not clear, partly because of high-amplitude irregular reflections complicated by the presence of a BSR near the top of Seismic Unit 3. The base of Seismic Unit 2 coincides with the base of Logging Unit 2 at 546 mbsf. This boundary is defined by an increase in gamma ray, density, resistivity, and *P*-wave velocity (Figures **F39**, **F40**) together with a significant change in bedding dip and strike (Figure **F42**) (see **Logging while drilling**). The increase in density and *P*-wave velocity across the base of Seismic Unit 2 results in a normal polarity reflection at Horizon S11.

Although most of Seismic Unit 2 was not targeted for coring during Expedition 375, RCB cores were recovered in the lower 29 m of the unit below 517 mbsf (Figure **F42**) (see **Lithostratigraphy**). These cores indicate that the lower part of the unit comprises mudstones with interbeds of sandy siltstone and very fine sandstone and rare volcanic ash. No obvious change in lithology or processes of sedimentation are recognized across Horizon S11. Biostratigraphy indicates that Seismic Unit 2 is Middle to early Pleistocene (see **Biostratigraphy**).

Seismic Unit 3 (546–650 mbsf)

Seismic Unit 3 is characterized by high-amplitude northwest-dipping reflections that lie in the hanging wall of a thrust fault located 500 m beneath the base of Site U1519 (Figure **F37**). This seismic unit coincides with Logging Unit 3, which is characterized overall by slightly elevated gamma ray and high density, resistivity,

Figure F39. Comparison of Hole U1519A logging units, Hole U1519C–U1519E lithostratigraphic units, synthetic-well tie, and Line 05CM-04 and Cross-Line TAN1114-08 seismic reflection data (locations shown on Figure F37 inset map). Labeled horizons are from P. Barnes (unpubl. data).

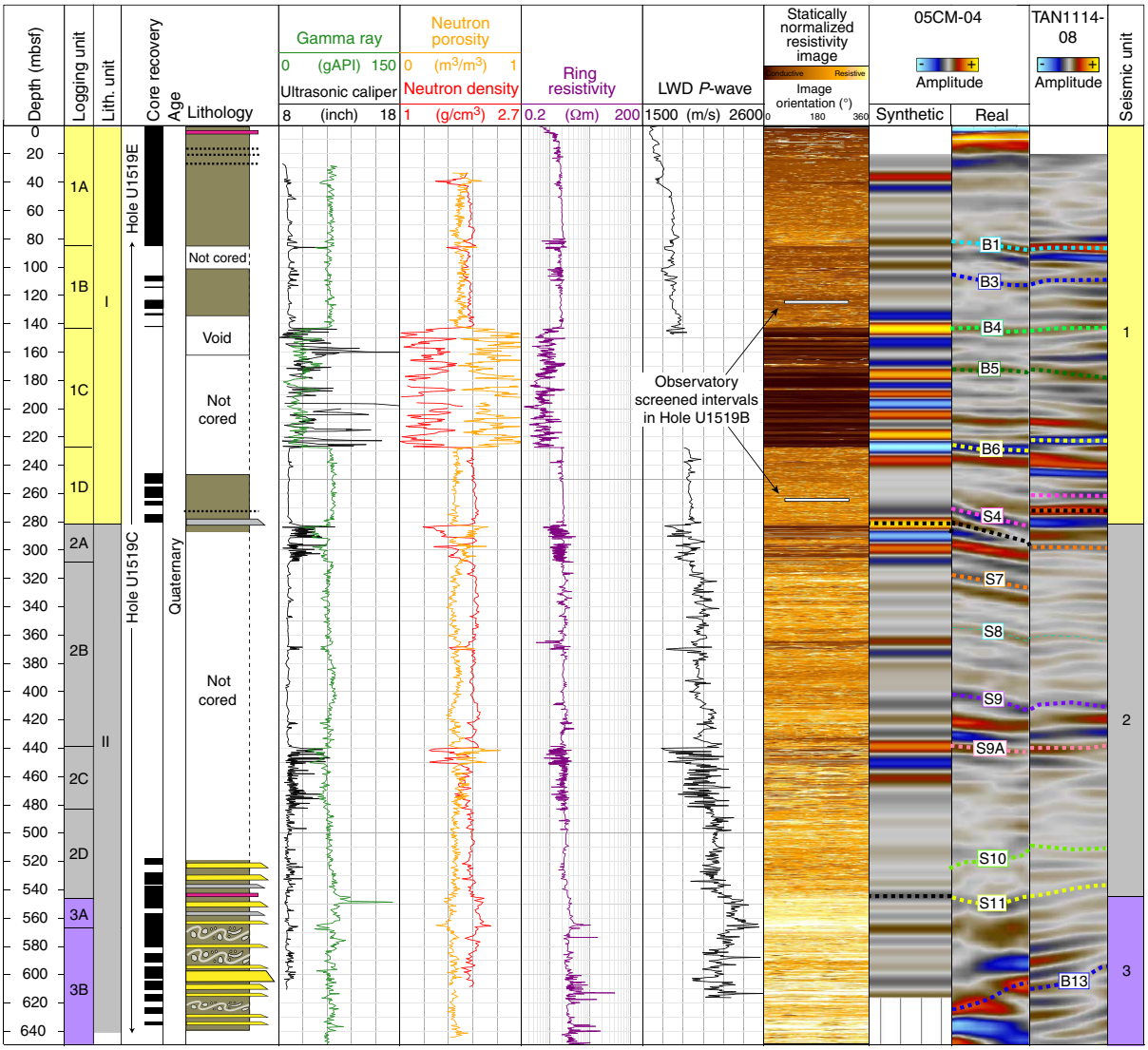

Table T14. Unit depths from preferred seismic-well tie, Site U1519. TWT = two-way traveltime. See Figure F36B. **Download table in CSV format.**

Base of seismic unit	TWT below sea level (ms)	Depth (mbsf)	Base of logging unit	Depth (mbsf)	Base of lith. unit	Depth (mbsf)
1	1652	274	1	281.5	I	282.7
2	1930	557	2	546.0	II	567.6

and *P*-wave velocity (Figures **F39**, **F40**). Moreover, predominantly northwest-dipping bedding orientations identified from resistivity image logging are consistent with the apparent dips in seismic data (Figure **F42**) (see **Logging while drilling**). RCB cores from the upper part of Seismic Unit 3 and coinciding with Logging Subunit 3A consist of mudstones with interbeds of sandy siltstone and very fine sandstone, similar to the lower part of Seismic Unit 2, as well as relatively thicker beds of medium- to very coarse grained sandstone (Figure **F39**) (see **Lithostratigraphy**).

A reversed polarity reflection at about 567 mbsf appears to coincide with the Logging Subunit 3A–3B transition, defined by a significant reduction in gamma ray, density, resistivity, and *P*-wave velocity and an increase in porosity (Figures **F39**, **F40**). Similar physical properties changes are apparent across this depth in laboratory measurements from cores (Figure **F42**) (see **Physical properties**). These changes coincide approximately with a change in lithology from bedded mudstone and sandstone to MTDs that include beds of shelly coarse-grained sand (see **Lithostratigraphy**). Structural observations from both core and resistivity image logs suggest that the lower part of Seismic Unit 3 exhibits fractures and faults with a wide range of dips and strikes (see **Structural geology** and **Logging while drilling**).

Prior to the expedition, Seismic Unit 3 was inferred to possibly be of late Miocene–Pliocene age, potentially equivalent to the Tolaga Group immediately onshore (Field et al., 1997). The biostratigraphic data from Hole U1519C, however, indicate that Seismic Unit 3 above 645 mbsf is Pleistocene age (younger than 1.7 Ma) (see **Biostratigraphy**), somewhat younger than anticipated.

Figure F40. Crossplots and histogram distributions of gamma ray, *P*-wave velocity, density, and resistivity values for logging units (see Logging while drilling), Site U1519.

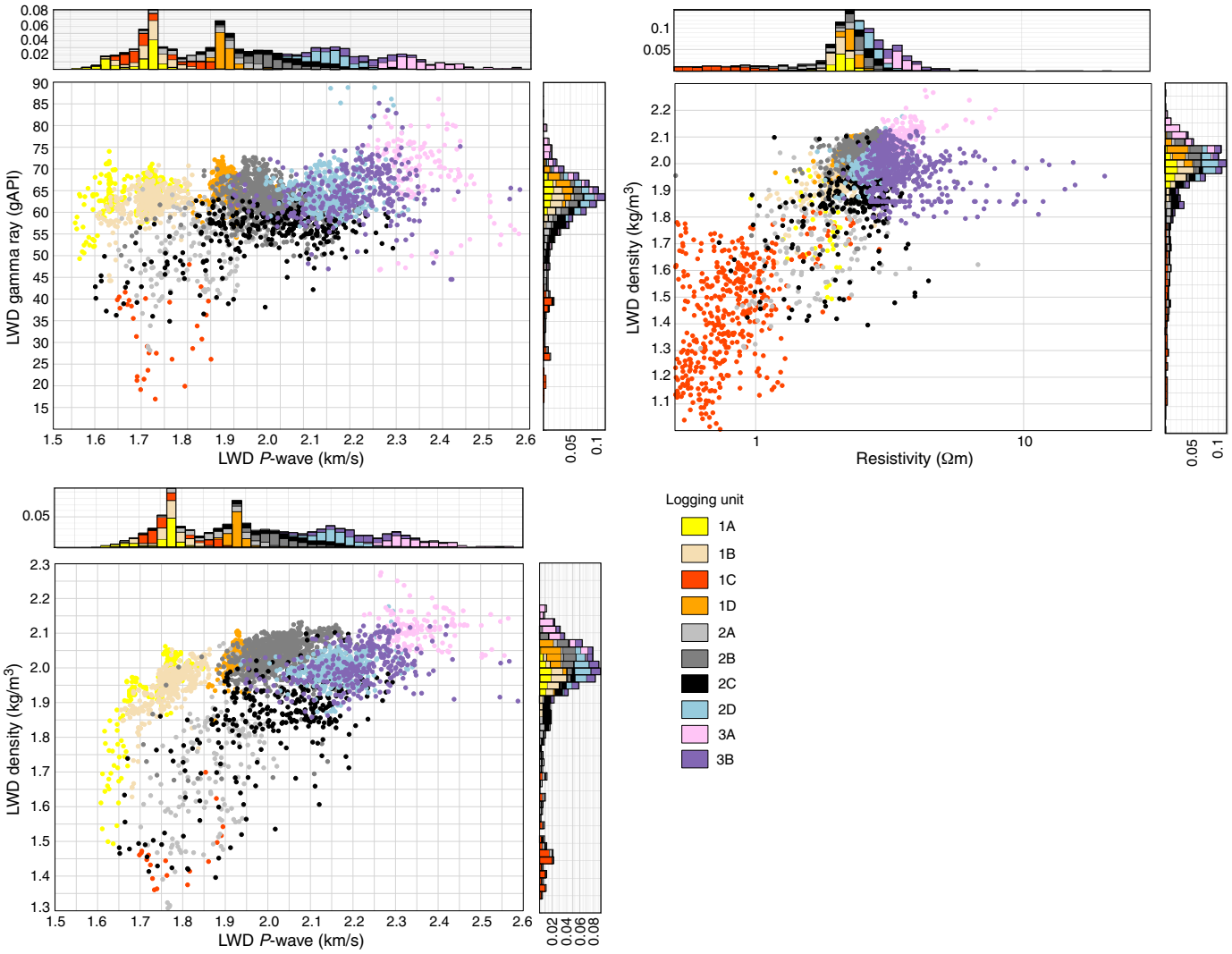

Hole U1519B observatory screened intervals

The observatory installed in Hole U1519B comprises two screened intervals, each 2 m long, in which pressure sensors were deployed (see **Observatory**). The pressure screens are centered at approximately 124 and 264 mbsf (Figure **F39**), and both are in Seismic Unit 1. The upper screen at 124 mbsf is located between Seismic Reflections B3 and B4, corresponding to Logging Subunit 1B and Lithostratigraphic Unit I. The lower observatory screen at 264 mbsf is located between Seismic Reflections B6 and S4, coinciding with Logging Subunit 1D and Lithostratigraphic Unit I. These intervals are both weakly reflective, and at least the upper interval is likely an MTD. On LWD logs, these intervals are characterized by gamma ray of about 61 and 66 gAPI, density of 2.0 and 2.1 g/cm^3, neutron density porosity of about 0.49 and 0.44, ring resistivity of 1.9 and 2.3 Ωm, and *P*-wave velocity values of 1795 and 1945 m/s, respectively. Both depths were associated with in-gauge borehole conditions (see **Logging while drilling**). RCB cores from both intervals were severely disturbed by drilling but are indicative of predominantly laminated silty mud of late Quaternary age (see **Lithostratigraphy** and **Biostratigraphy**).

Figure F41. Comparison of Hole U1519A LWD data, Hole U1519C laboratory physical properties data, and Line 05CM-04 seismic reflection data for cored interval 240–320 mbsf. Con. = conductive, Res. = resistive.

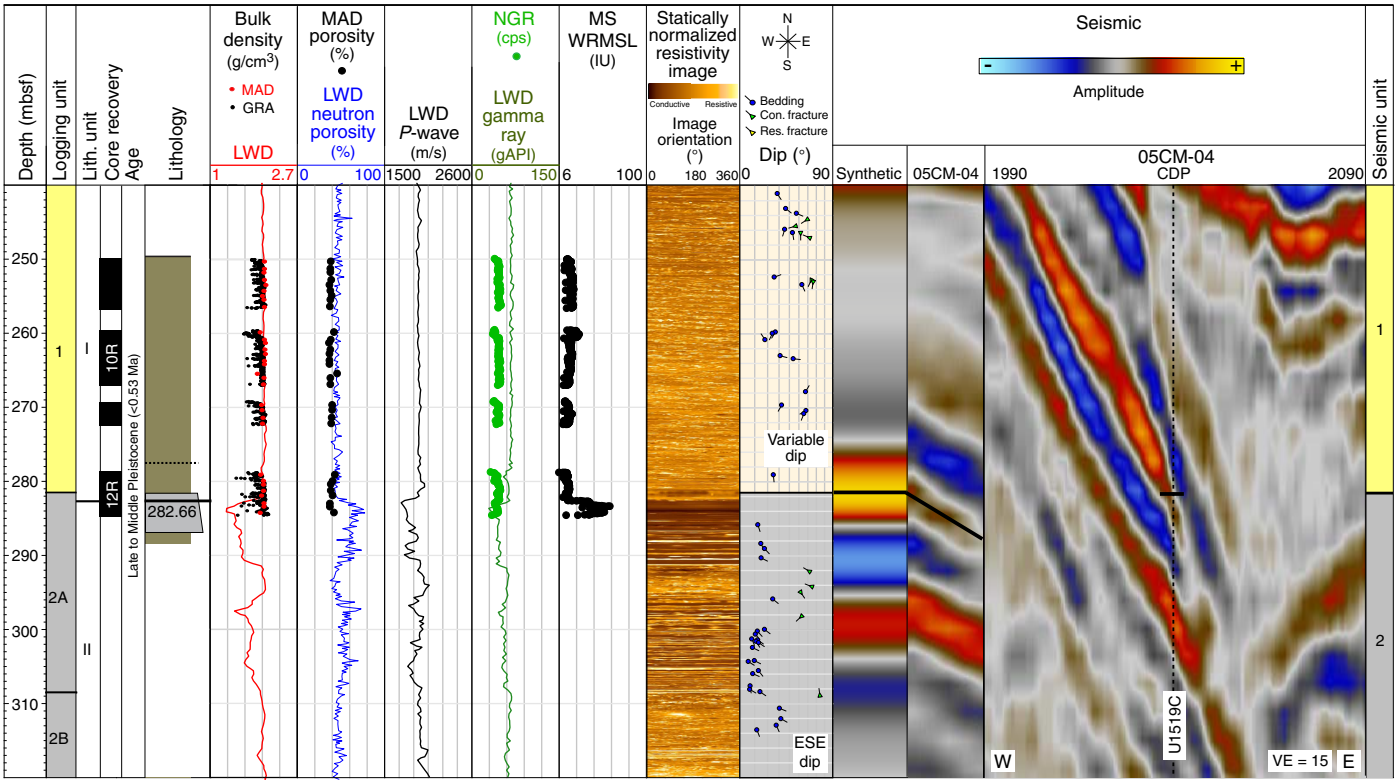

Figure F42. Comparison of Hole U1519A LWD data, Hole U1519C laboratory physical properties data, and Line 05CM-04 seismic reflection data for cored interval 500–650 mbsf. PWC = *P*-wave caliper. Con. = conductive, Res. = resistive.

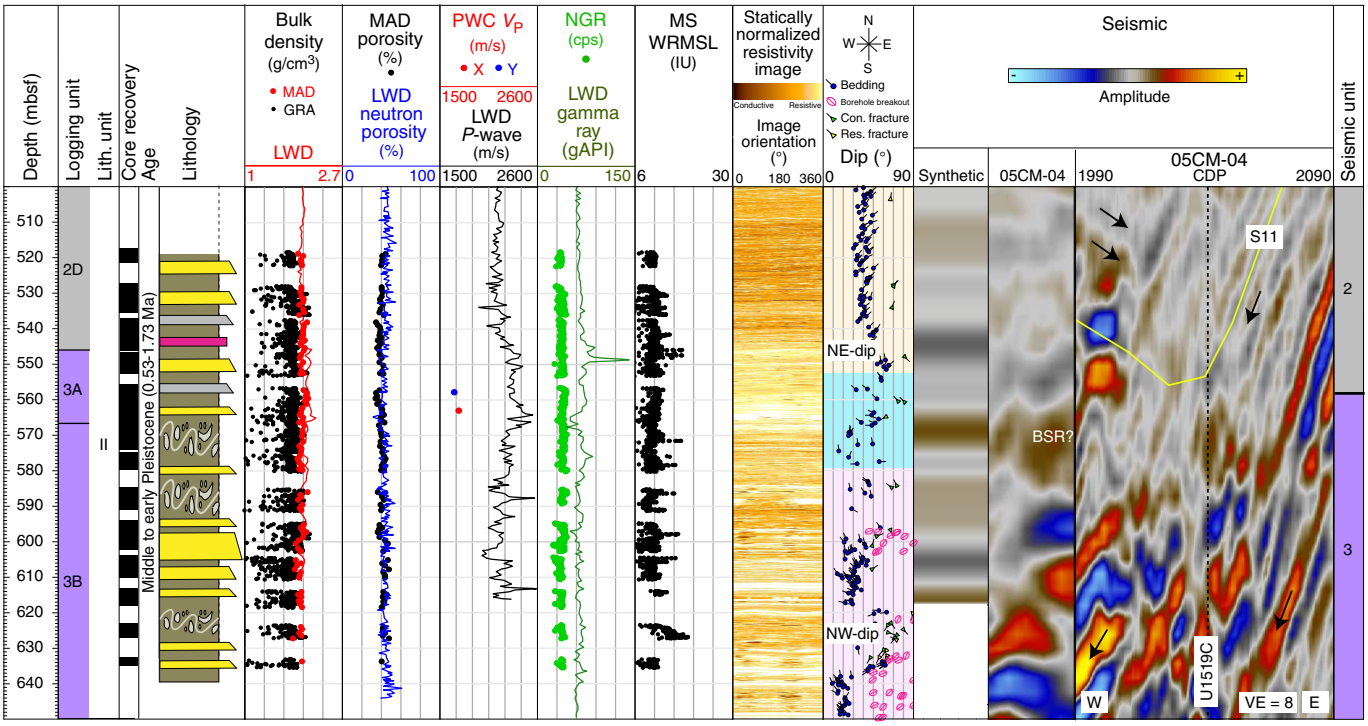

Observatory

The borehole observatory installed in Hole U1519B is designed to provide a time series of formation pressures and temperatures in the hanging wall directly above the source area of recurring SSEs on the plate interface. The data will be retrieved at a later date using a submersible ROV. The objectives of the observatory are to characterize hydrologic and thermal conditions in the upper plate and to document deformation and hydrological processes acting over a range of timescales, including short-lived transients associated with slow slip.

General design

Similar to the observatory installed at Site U1518 (see **Observatory** in the Site U1518 chapter [Saffer et al., 2019b]), the observatory at Site U1519 includes nested ACORK and CORK-II elements (Figure **F43**) (Becker and Davis, 2005). The ACORK consists of 10¾ inch steel casing with two 2 m long casing screens and an umbilical on its exterior. The umbilical contains hydraulic lines that terminate in the casing screens at depth and are connected to pressure gauges and a data logger at the wellhead. The CORK-II is installed inside the ACORK casing and consists of 4½ inch steel casing and an additional wellhead that is seated on top of the ACORK. An instrument string containing temperature sensors is hung in the CORK-II casing. In contrast to the observatory installed in Hole U1518H, the observatory in Hole U1519B does not contain an OsmoSampler package and the ACORK casing has no perforated sections. Installation operations are described in **Operations**.

The two screened intervals where hydraulic lines terminate (for pressure sensing) are centered at 123.74 and 263.60 mbsf (Table **T15**). Both screens are placed in lithologies interpreted to be homogeneous mudstone or siltstone in Logging Subunits 1B and 1D (see **Logging while drilling** and **Core-log-seismic integration**). The position and serial number of each of the 15 temperature sensors in

Figure F43. Completed observatory, Hole U1519B. CrN-DLC = chromium nitride-diamond like carbon. OD = outside diameter, ID = inside diameter.

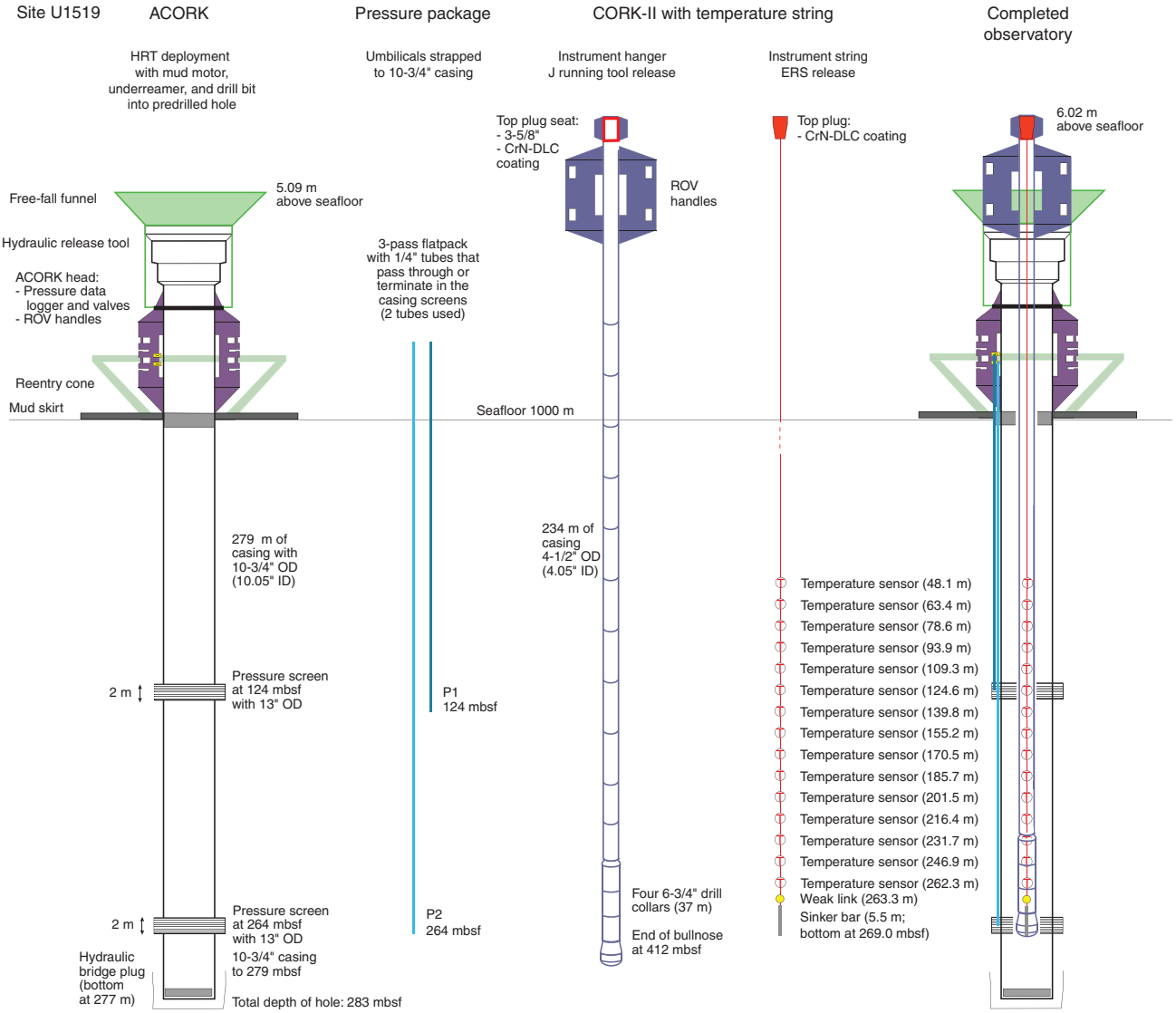

Table T15. Screened intervals for hanging wall observatory, Hole U1519B. **Download table in CSV format.**

Screened interval	Centered depth (mbsf)	Screened interval (mbsf)	Interval length (m)
Upper screen	123.74	123.00–125.00	2
Lower screen	263.60	263.00–265.00	2

the observatory are listed in Table **T16**. Temperature sensor positions are reported relative to the seafloor and to the weak link at the bottom of the sensor string (Figure **F43**; see **Operations**).

Pressure sensing and ACORK

Seafloor and formation fluid pressures are measured with absolute pressure gauges (APGs) connected to a data logger on the ACORK wellhead. Three APGs are mounted on the wellhead: two APGs measure formation pressure (Figure **F44B**), and the third senses pressure at the wellhead (seafloor pressure). The pressure sensing package is equipped with Paroscientific Digiquartz pressure transducers (two Model 8B2000-2 for formation pressure sensing and one Model 8B1400-2 for seafloor pressure), a high-precision pressure period counter with a 12.8 MHz real-time clock (RTC-PPC system resolving ~10 ppb of full-scale pressure or ~0.7 Pa), and a 24-bit/channel analog-to-digital converter and data logger (Bennest Enterprises, Ltd.; Minerva Technologies, Ltd.; and the Pacific Geoscience Centre, Geological Survey of Canada). The data logger in the pressure sensing unit at the wellhead can be accessed via an ODI Teledyne underwater mateable connector mounted on the unit. The data logger is programmed to record pressures once every 60 s from each of the APGs.

The APGs for the formation pressure measurements are connected to an umbilical along the exterior of the ACORK casing that terminates in carbolite-filled screens external to the casing. The screens are made out of 316SS stainless steel and wrapped with 0.085 inch wire with a 0.01 inch wire-to-wire spacing that results in an open cross section of 15%. The carbolite beads have a diameter of 600 µm. Figure **F44A** shows the uppermost screen and some of the umbilical tubing. The umbilical tubes (Figure **F44B**) act as pressure conduits that relay pressures from the screens in communication with the formation to the gauges at the wellhead. The bottom of the ACORK is sealed with a bridge plug so that the interior of the borehole is fully isolated from formation fluids. Valves at the wellhead allow individual pressure lines to be closed to the ocean so that the gauges directly record the pressure in the formation at depth or open to the ocean for periodic hydrostatic checks or to allow fluid sampling (Figure **F44C**).

Instrument string and temperature sensing

Fifteen temperature sensors are suspended on ⅜ inch Spectra rope as part of the instrument string. Table **T16** lists the position of the temperature sensors relative to seafloor and relative to the weak link above the sinker bar at the bottom of the sensor string. We use RBRsolo T 10K abyssal temperature recorders manufactured by RBR. The instruments have a temperature accuracy of ±0.002°C and titanium enclosures that are pressure rated for ocean depths as deep as 10,000 m. Each unit is autonomous, with its own sensor and data logger. The units are programmed to measure once every 10 s. The measurement duration is limited by their battery life; for 10 s sampling intervals, measurements are expected to continue for >7 y (until April 2025).

Table T16. Estimated in situ temperature sensor positions, Site U1519. These depth estimates assume 2% stretch based on direct pre-expedition measurements under comparable tension maintained by the 500 lb sinker bar and weak link at the bottom of the instrument string. **Download table in CSV format.**

Position (mbsf)	Position above weak link (m)	Label	Serial number	Rope section
48.05	215.25	HW210	37412	H1
63.35	199.95	HW195	37411	H1
78.63	184.67	HW180	37410	H1
93.93	169.37	HW165	37409	H1
109.26	154.04	HW150	37408	H1
124.57	138.73	HW135	37407	H1
139.84	123.46	HW120	37406	H1
155.16	108.14	HW105	37405	H1
170.45	92.85	HW90	37404	H1
185.74	77.56	HW75	37403	H1
201.05	62.25	HW60	37402	H1
216.36	46.94	HW45	37401	H1
231.65	31.65	HW30	37400	H1
246.94	16.36	HW15	37399	H1
262.28	1.02	HW0	37398	H1

The temperature sensors are connected to the Spectra rope with utility cord tied to attachment eyelets spliced into the line (see **Observatory** in the Site U1518 chapter [Saffer et al., 2019b]). Each instrument is then wrapped in a protective covering of ¼ inch (or thinner) rubber sheeting and wrapped in tape. The covering protects the instrument from impacts and creates a smooth profile to prevent the instrument string from snagging during deployment or recovery.

Additional instrument string components

From the bottom up, the instrument string consists of one sinker bar, one weak link, a single 269.28 m long rope section with 15 temperature sensors, and a top plug. The sinker bar at the bottom of the instrument string is a single ~6 m long, ~7.5 cm diameter steel bar weighing ~500 lb in water (Figure **F45**). The purpose of the sinker bar is to keep the rope taut during deployment, maintain the position of the temperature sensors at their correct depths, and help pull the instrument string into the CORK-II wellhead and seat the top plug.

The weak link is placed between the instrument string and the sinker bar to address the possibility of the sinker bar hanging up during retrieval (Figure **F46**). The weak link consists of two metal end pieces and two connection plates (see Figure **F70** in the Site U1518 chapter [Saffer et al., 2019b] for a different view of similar weak links). The pieces are sewn together with ⅛ inch polypropylene cord through as many as 150 pass-through holes. The number of holes that are threaded controls the strength because the end pieces can only separate by shearing the polypropylene cords. For Hole U1519B, the weak link is programmed for 4400 lb tensile strength, with 39 of the 75 threads sewn on each end.

The rope section above the weak link is composed of ⅜ inch 12-strand Spectra rope (manufactured by Cortland, Ltd.). Spectra is a Class II rope material that is ideal for the purposes of the observatory because it has high strength and low stretch, is easy to splice, and is slightly positively buoyant (Fisher et al., 2005, 2011; Edwards et al., 2012). For the ⅜ inch rope, the mean tensile strength is 15,400 lb and 13,900 lb when spliced. Rope splices are used to connect rope sections to other parts, attach sensors, and provide handling eyes to

Figure F44. Pressure sensing components, Hole U1519B. A. Pressure monitoring screen. B. Hydraulic lines in umbilical (green) being attached to pressure monitoring screen on exterior of ACORK casing. C. Pressure valves and external sampling ports on ACORK wellhead.

Figure F45. Sinker bar (18 ft long, 3 inch diameter) that constitutes the bottom of the instrument string, Hole U1519B.

Figure F46. Weak link, Hole U1519B. Side view shows separate pieces held together with woven plates.

ease deployment and recovery (see Figure **F68** in the Site U1518 chapter [Saffer et al., 2019b] for examples).

A top plug forms the upper end of the instrument string and includes an O-ring and a 3⅝ inch seat that seals the interior of the CORK-II casing (Figure **F47**). In contrast to the Hole U1518H observatory, this top plug does not latch because the interior of the ACORK casing is isolated from formation pressures via the bridge plug (and unlike the observatory at Site U1518, the ACORK casing does not have any perforated sections). The top plug also serves as the instrument hanger, with a 1½ inch diameter ring through which the rope is spliced. The top of the top plug is designed to permit recovery with the ERS.

Deployment and completion

The weight of the instrument string was monitored with the Schlumberger wireline system during deployment. Wireline tension monitoring did not show any sign of a hang up and recorded a drop in tension when the top plug was seated.

As described in **Operations**, the CORK-II was then lowered the remaining 11 m to its seat in the ACORK. The CORK-II was then released from the drill pipe using a J running tool. There are two issues to note regarding the release and subsequent inspection of the wellhead. First, the CORK-II wellhead appears to have sustained minor damage during release, and one of the fins on the wellhead is slightly bent. We do not anticipate that this will pose a problem for

Figure F47. Instrument string top plug, Hole U1519B. Top plug is attached to Schlumberger wireline ERS from above and connected to the Spectra rope on the bottom.

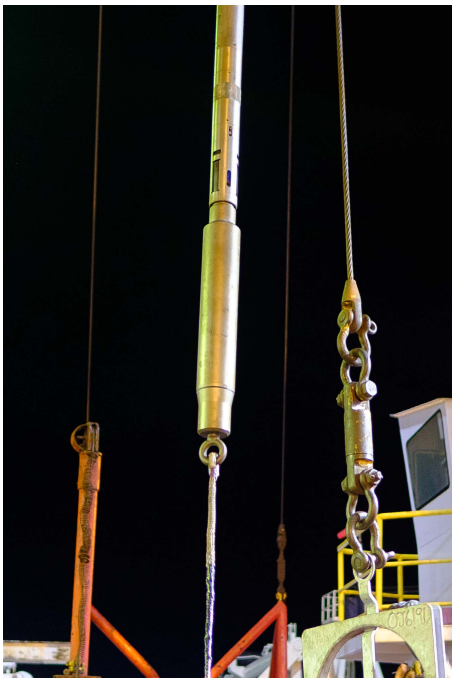

temperature sensor recovery; however, if the inner bore of the casing at the wellhead is warped or obstructed, then the sinker bar may be difficult to recover and the weak link may need to be broken. In addition, cuttings have accumulated in the reentry cone beneath the ACORK wellhead such that the hydraulic connections to the pressure instrument package are covered. This should not impact the ability to download data or manipulate valves but may complicate future exchange of the pressure data logger and batteries (Figure **F48**). Tentative plans are to use an ROV to download initial pressure data in 2019 and to collect the instrument string with temperature sensors and conduct an additional pressure data download by 2023.

Figure F48. Inspection of Hole U1519B wellhead immediately after installation. A. Top plug seated in CORK-II. B. Bent stabilizing fin on CORK-II wellhead. C. Cuttings in reentry cone partially covering hydraulic connections on ACORK wellhead. Data ports and valves remain exposed.

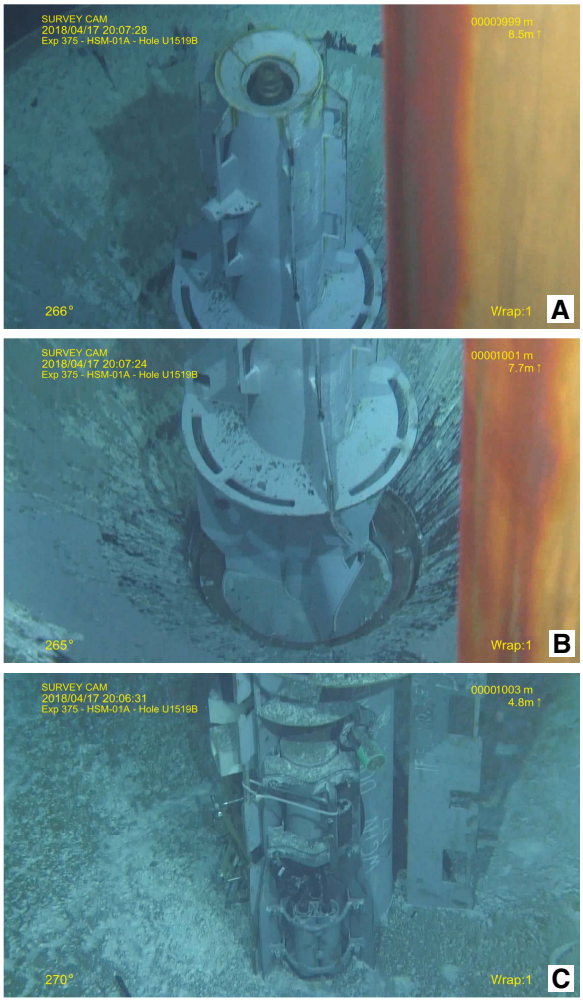

References

Antriasian, A., Harris, R.N., Tréhu, A.M., Henrys, S.A., Phrampus, B.J., Lauer, R., Gorman, A.R., Pecher, I.A., and Barker, D., 2018. Thermal regime of the northern Hikurangi margin, New Zealand. *Geophysical Journal International*, 216(2):1177–1190. **https://doi.org/10.1093/gji/ggy450**

Barker, D.H.N., Henrys, S., Caratori Tontini, F., Barnes, P. M., Bassett, D., Todd, E., and Wallace, L., 2018. Geophysical constraints on the relationship between seamount subduction, slow slip and tremor at the north Hikurangi subduction zone, New Zealand. *Geophysical Research Letters,* 45(23):12804–12813. **https://doi.org/10.1029/2018GL080259**

Barker, D.H.N., Sutherland, R., Henrys, S., and Bannister, S., 2009. Geometry of the Hikurangi subduction thrust and upper plate, North Island, New Zealand. *Geochemistry, Geophysics, Geosystems,* 10(2):Q02007. **https://doi.org/10.1029/2008GC002153**

Barnes, P.M., Pecher, I.A., LeVay, L.J., Bourlange, S.M., Brunet, M.M.Y., Cardona, S., Clennell, M.B., Cook, A.E., Crundwell, M.P., Dugan, B., Elger, J., Gamboa, D., Georgiopoulou, A., Greve, A., Han, S., Heeschen, K.U., Hu, G., Kim, G.Y., Kitajima, H., Koge, H., Li, X., Machado, K.S., McNamara, D.D., Moore, G.F., Mountjoy, J.J., Nole, M.A., Owari, S., Paganoni, M., Petronotis, K.E., Rose, P.S., Screaton, E.J., Shankar, U., Shepherd, C.L., Torres, M.E., Underwood, M.B., Wang, X., Woodhouse, A.D., and Wu, H.-Y., 2019. Site U1517. *In* Pecher, I.A., Barnes, P.M., LeVay, L.J., and the Expedition 372A Scientists, *Creeping Gas Hydrate Slides.* Proceedings of the International Ocean Discovery Program, 372A: College Station, TX (International Ocean Discovery Program). **https://doi.org/10.14379/iodp.proc.372A.103.2019**

Becker, K., and Davis, E.E., 2005. A review of CORK designs and operations during the Ocean Drilling Program. *In* Fisher, A.T., Urabe, T., Klaus, A., and the Expedition 301 Scientists, *Proceedings of the Integrated Ocean Drilling Program,* 301: College Station, TX (Integrated Ocean Drilling Program Management International, Inc.). **https://doi.org/10.2204/iodp.proc.301.104.2005**

Bell, R., Sutherland, R., Barker, D.H.N., Henrys, S., Bannister, S., Wallace, L., and Beavan, J., 2010. Seismic reflection character of the Hikurangi subduction interface, New Zealand, in the region of repeated Gisborne slow slip events. *Geophysical Journal International,* 180(1):34–48. **https://doi.org/10.1111/j.1365-246X.2009.04401.x**

Bullard, E.C., 1939. Heat flow in South Africa. *Proceedings of the Royal Society of London, Series A: Mathematical, Physical and Engineering Sciences,* 173(955):474–502. **https://doi.org/10.1098/rspa.1939.0159**

Chang, C., McNeill, L.C., Moore, J.C., Lin, W., Conin, M., and Yamada, Y., 2010. In situ stress state in the Nankai accretionary wedge estimated from borehole wall failures. *Geochemistry, Geophysics, Geosystems,* 11:Q0AD04. **https://doi.org/10.1029/2010GC003261**

Claypool, G.E., and Kvenvolden, K.A., 1983. Methane and other hydrocarbon gases in marine sediment. *Annual Review of Earth and Planetary Sciences,* 11(1):299–327. **https://doi.org/10.1146/annurev.ea.11.050183.001503**

Davis, E., Becker, K., Wang, K., and Kinoshita, M., 2009. Co-seismic and post-seismic pore-fluid pressure changes in the Philippine Sea plate and Nankai decollement in response to a seismogenic strain event off Kii Peninsula, Japan. *Earth, Planets Space,* 61(6):649–657. **http://www.terrapub.co.jp/journals/EPS/abstract/6106/61060649.html**

De Vleeschouwer, D., Dunlea, A.G., Auer, G., Anderson, C.H., Brumsack, H., de Loach, A., Gurnis, M., et al., 2017. Quantifying K, U, and Th contents of marine sediments using shipboard natural gamma radiation spectra measured on DV *JOIDES Resolution*. *Geochemistry, Geophysics, Geosystems,* 18(3):1053–1064. **https://doi.org/10.1002/2016GC006715**

Dickens, G.R., 2001. Sulfate profiles and barium fronts in sediment on the Blake Ridge: present and past methane fluxes through a large gas hydrate reservoir. *Geochimica et Cosmochimica Acta,* 65(4):529–543. **https://doi.org/10.1016/S0016-7037(00)00556-1**

Edwards, K.J., Wheat, C.G., Orcutt, B.N., Hulme, S., Becker, K., Jannasch, H., Haddad, A., Pettigrew, T., Rhinehart, W., Grigar, K., Bach, W., Kirkwood, W., and Klaus, A., 2012. Design and deployment of borehole observatories and experiments during IODP Expedition 336, Mid-Atlantic Ridge flank at North Pond. *In* Edwards, K.J., Bach, W., Klaus, A., and the Expedition 336 Scientists, *Proceedings of the Integrated Ocean Drilling Program,* 336: Tokyo (Integrated Ocean Drilling Program Management International, Inc.). **https://doi.org/10.2204/iodp.proc.336.109.2012**

Field, B.D., Uruski, C.I., Bey, A., Browne, G., Crampton, J., Funnell, R., Killops, S., Laird, M., Mazengarb, C., Morgans, H., Rait, G., Smale, D., and Strong, P., 1997. *Cretaceous–Cenozoic Geology and Petroleum Systems of the East Coast Region, New Zealand.* GNS Monograph, 19.

Fisher, A.T., Wheat, C.G., Becker, K., Cowen, J., Orcutt, B., Hulme, S., Inderbitzen, K., Turner, A., Pettigrew, T.L., Davis, E.E., Jannasch, H., Grigar, K., Adudell, R., Meldrum, R., Macdonald, R., and Edwards, K., 2011. Design, deployment, and status of borehole observatory systems used for single-hole and cross-hole experiments, IODP Expedition 327, eastern flank of Juan de Fuca Ridge. *In* Fisher, A.T., Tsuji, T., Petronotis, K., and the Expedition 327 Scientists, *Proceedings of the Integrated Ocean Drilling Program,* 327: College Station, TX (Integrated Ocean Drilling Program Management International, Inc.). **https://doi.org/10.2204/iodp.proc.327.107.2011**

Fisher, A.T., Wheat, C.G., Becker, K., Davis, E.E., Jannasch, H., Schroeder, D., Dixon, R., Pettigrew, T.L., Meldrum, R., McDonald, R., Nielsen, M., Fisk, M., Cowen, J., Bach, W., and Edwards, K., 2005. Scientific and technical design and deployment of long-term subseafloor observatories for hydrogeologic and related experiments, IODP Expedition 301, eastern flank of Juan de Fuca Ridge. *In* Fisher, A.T., Urabe, T., Klaus, A., and the Expedition 301 Scientists, *Proceedings of the Integrated Ocean Drilling Program,* 301: College Station, TX (Integrated Ocean Drilling Program Management International, Inc.). **https://doi.org/10.2204/iodp.proc.301.103.2005**

Henrys, S.A., Ellis, S., and Uruski, C., 2003. Conductive heat flow variations from bottom-simulating reflectors on the Hikurangi margin, New Zealand. *Geophysical Research Letters,* 30(2):1065. **https://doi.org/10.1029/2002GL015772**

Huffman, K.A., and Saffer, D.M., 2016. In situ stress magnitudes at the toe of the Nankai Trough Accretionary Prism, offshore Shikoku Island, Japan. *Journal of Geophysical Research: Solid Earth,* 121(2):1202–1217. **https://doi.org/10.1002/2015JB012415**

Martini, E., 1971. Standard Tertiary and Quaternary calcareous nannoplankton zonation. *In* Farinacci, A. (Ed.), *Proceedings of the Second Planktonic Conference, Roma 1970:* Rome (Edizioni Tecnoscienza), 739–785.

Mountjoy, J.J., and Barnes, P., 2011. Active upper plate thrust faulting in regions of low plate interface coupling, repeated slow slip events, and coastal uplift: example from the Hikurangi margin, New Zealand. *Geochemistry, Geophysics, Geosystems,* 12(1):Q01005. **https://doi.org/10.1029/2010GC003326**

Mountjoy, J.J., McKean, J., Barnes, P.M., and Pettinga, J.R., 2009. Terrestrial-style slow-moving earthflow kinematics in a submarine landslide complex. *Marine Geology,* 267(3–4):114–127. **https://doi.org/10.1016/j.margeo.2009.09.007**

Mountjoy, J.J., Pecher, I., Henrys, S., Crutchley, G., Barnes, P.M., and Plaza-Faverola, A., 2014. Shallow methane hydrate system controls ongoing, downslope sediment transport in a low-velocity active submarine landslide complex, Hikurangi Margin, New Zealand. *Geochemistry, Geophysics, Geosystems,* 15(11):4137–4156. **https://doi.org/10.1002/2014GC005379**

Pedley, K.L., Barnes, P.M., Pettinga, J.R., and Lewis, K.B., 2010. Seafloor structural geomorphic evolution of the accretionary frontal wedge in response to seamount subduction, Poverty Indentation, New Zealand. *Marine Geology,* 270(1–4):119–138. **https://doi.org/10.1016/j.margeo.2009.11.006**

Pimmel, A., and Claypool, G., 2001. *Technical Note 30: Introduction to Shipboard Organic Geochemistry on the JOIDES Resolution.* Ocean Drilling Program. **https://doi.org/10.2973/odp.tn.30.2001**

Saffer, D.M., Wallace, L.M., Barnes, P.M., Pecher, I.A., Petronotis, K.E., LeVay, L.J., Bell, R.E., Crundwell, M.P., Engelmann de Oliveira, C.H., Fagereng, A., Fulton, P.M., Greve, A., Harris, R.N., Hashimoto, Y., Hüpers, A., Ikari, M.J., Ito, Y., Kitajima, H., Kutterolf, S., Lee, H., Li, X., Luo, M., Malie, P.R., Meneghini, F., Morgan, J.K., Noda, A., Rabinowitz, H.S., Savage, H.M.,

Shepherd, C.L., Shreedharan, S., Solomon, E.A., Underwood, M.B., Wang, M., Woodhouse, A.D., Bourlange, S.M., Brunet, M.M.Y., Cardona, S., Clennell, M.B., Cook, A.E., Dugan, B., Elger, J., Gamboa, D., Georgiopoulou, A., Han, S., Heeschen, K.U., Hu, G., Kim, G.Y., Koge, H., Machado, K.S., McNamara, D.D., Moore, G.F., Mountjoy, J.J., Nole, M.A., Owari, S., Paganoni, M., Rose, P.S., Screaton, E.J., Shankar, U., Torres, M.E., Wang, X., and Wu, H.-Y., 2019a. Expedition 372B/375 summary. *In* Wallace, L.M., Saffer, D.M., Barnes, P.M., Pecher, I.A., Petronotis, K.E., LeVay, L.J., and the Expedition 372/375 Scientists, *Hikurangi Subduction Margin Coring, Logging, and Observatories.* Proceedings of the International Ocean Discovery Program, 372B/375: College Station, TX (International Ocean Discovery Program). **https://doi.org/10.14379/iodp.proc.372B375.101.2019**

Saffer, D.M., Wallace, L.M., Barnes, P.M., Pecher, I.A., Petronotis, K.E., LeVay, L.J., Bell, R.E., Crundwell, M.P., Engelmann de Oliveira, C.H., Fagereng, A., Fulton, P.M., Greve, A., Harris, R.N., Hashimoto, Y., Hüpers, A., Ikari, M.J., Ito, Y., Kitajima, H., Kutterolf, S., Lee, H., Li, X., Luo, M., Malie, P.R., Meneghini, F., Morgan, J.K., Noda, A., Rabinowitz, H.S., Savage, H.M., Shepherd, C.L., Shreedharan, S., Solomon, E.A., Underwood, M.B., Wang, M., Woodhouse, A.D., Bourlange, S.M., Brunet, M.M.Y., Cardona, S., Clennell, M.B., Cook, A.E., Dugan, B., Elger, J., Gamboa, D., Georgiopoulou, A., Han, S., Heeschen, K.U., Hu, G., Kim, G.Y., Koge, H., Machado, K.S., McNamara, D.D., Moore, G.F., Mountjoy, J.J., Nole, M.A., Owari, S., Paganoni, M., Rose, P.S., Screaton, E.J., Shankar, U., Torres, M.E., Wang, X., and Wu, H.-Y., 2019b. Site U1518. *In* Wallace, L.M., Saffer, D.M., Barnes, P.M., Pecher, I.A., Petronotis, K.E., LeVay, L.J., and the Expedition 372/375 Scientists, *Hikurangi Subduction Margin Coring, Logging, and Observatories.* Proceedings of the International Ocean Discovery Program, 372B/375: College Station, TX (International Ocean Discovery Program). **https://doi.org/10.14379/iodp.proc.372B375.103.2019**

Solomon, E.A., Spivack, A.J., Kastner, M., Torres, M.E., and Robertson, G., 2014. Gas hydrate distribution and carbon sequestration through coupled microbial methanogenesis and silicate weathering in the Krishna–Godavari Basin, offshore India. *Marine and Petroleum Geology,* 58(A):233–253. **https://doi.org/10.1016/j.marpetgeo.2014.08.020**

Torres, M.E., Brumsack, H.-J., Bohrmann, G., and Emeis, K.C., 1996. Barite fronts in continental margin sediments: a new look at barium remobilization in the zone of sulfate reduction and formation of heavy barites in diagenetic fronts. *Chemical Geology,* 127(1–3):125–139. **https://doi.org/10.1016/0009-2541(95)00090-9**

Townend, J., 1997. Estimates of conductive heat flow through bottom-simulating reflectors on the Hikurangi and southwest Fiordland continental margins, New Zealand. *Marine Geology,* 141(1–4):209–220. **https://doi.org/10.1016/S0025-3227(97)00073-X**

Wallace, L.M., and Beavan, J., 2010. Diverse slow slip behavior at the Hikurangi subduction margin, New Zealand. *Journal of Geophysical Research: Solid Earth,* 115(B12):B12402. **https://doi.org/10.1029/2010JB007717**

Wallace, L.M., Saffer, D.M., Barnes, P.M., Pecher, I.A., Petronotis, K.E., LeVay, L.J., Bell, R.E., Crundwell, M.P., Engelmann de Oliveira, C.H., Fagereng, A., Fulton, P.M., Greve, A., Harris, R.N., Hashimoto, Y., Hüpers, A., Ikari, M.J., Ito, Y., Kitajima, H., Kutterolf, S., Lee, H., Li, X., Luo, M., Malie, P.R., Meneghini, F., Morgan, J.K., Noda, A., Rabinowitz, H.S., Savage, H.M., Shepherd, C.L., Shreedharan, S., Solomon, E.A., Underwood, M.B., Wang, M., Woodhouse, A.D., Bourlange, S.M., Brunet, M.M.Y., Cardona, S., Clennell, M.B., Cook, A.E., Dugan, B., Elger, J., Gamboa, D., Georgiopoulou, A., Han, S., Heeschen, K.U., Hu, G., Kim, G.Y., Koge, H., Machado, K.S., McNamara, D.D., Moore, G.F., Mountjoy, J.J., Nole, M.A., Owari, S., Paganoni, M., Rose, P.S., Screaton, E.J., Shankar, U., Torres, M.E., Wang, X., and Wu, H.-Y., 2019. Expedition 372B/375 methods. *In* Wallace, L.M., Saffer, D.M., Barnes, P.M., Pecher, I.A., Petronotis, K.E., LeVay, L.J., and the Expedition 372/375 Scientists, *Hikurangi Subduction Margin Coring, Logging, and Observatories.* Proceedings of the International Ocean Discovery Program, 372B/375: College Station, TX (International Ocean Discovery Program). **https://doi.org/10.14379/iodp.proc.372B375.102.2019**

Wallace, L.M., Webb, S.C., Ito, Y., Mochizuki, K., Hino, R., Henrys, S., Schwartz, S.Y., and Sheehan, A.F., 2016. Slow slip near the trench at the Hikurangi subduction zone, New Zealand. *Science,* 352(6286):701–704. **https://doi.org/10.1126/science.aaf2349**

Wang, K., 2004. Applying fundamental principles and mathematical models to understand processes and estimate parameters. *In* Davis, E.E., and Elderfield, H. (Eds.), *Hydrogeology of the Oceanic Lithosphere:* Cambridge, United Kingdom (Cambridge University Press), 376–413.

Zoback, M.D., 2007. *Reservoir Geomechanics:* Cambridge, United Kingdom (Cambridge University Press). **https://doi.org/10.1017/CBO9780511586477**